Extracellular Vesicle Capture and microRNA Detection

by

Nidhi Juthani

BASc. Chemical Engineering, University of Waterloo (2017)
M.S. Chemical Engineering Practice, Massachusetts Institute of Technology (2019)

Submitted to the Department of Chemical Engineering
in partial fulfillment of the requirements for the degree of

Doctor of Philosophy in Chemical Engineering

at the

MASSACHUSETTS INSTITUTE OF TECHNOLOGY

June 2023

Author .....
Department of Chemical Engineering
August 31, 2021

Certified by .....
Patrick S. Doyle
Robert T. Haslam (1911) Professor of Chemical Engineering
Thesis Supervisor

Accepted by .....
Patrick S. Doyle
Robert T. Haslam (1911) Professor of Chemical Engineering

Extracellular Vesicle Capture and microRNA Detection

by

Nidhi Juthani

Submitted to the Department of Chemical Engineering
on August 31, 2021, in partial fulfillment of the
requirements for the degree of
Doctor of Philosophy in Chemical Engineering

Abstract

Cancer is one of the leading causes of death in the United states, and there has been much focus on earlier detection through the discovery of novel, easily accessible biomarkers via liquid biopsies. Extracellular vesicles have shown promise as a non-invasive biomarker for disease diagnosis and monitoring, and have become a treasure trove of information because they have been found to carry proteins, DNA, mRNA and microRNA as well surface markers indicative of the their cell origin. Thus developing methods to profile extracellular vesicles and interrogate the contents of these vesicles is a growing area of research and has the potential to develop into a non-invasive diagnostic platform, a liquid biopsy.

The aim of this thesis is to develop a system to capture extracellular vesicles and profile the miRNA patterns present within them. First, we develop various amplification strategies in hydrogel particles for microRNA detection, including a colorimetric detection platform that can be translated to point-of-care settings for a liquid biopsy. We also explored other amplification strategies for increased miRNA detection sensitivity including precipitation-based enzymatic signal amplification and strand displacement amplification.

Then we develop methods for extracellular vesicle lysis and miRNA detection using a one-pot lysis and miRNA capture method. Extracellular vesicles were isolated from matched diseased and normal donor serum. Using rolling circle amplification, we performed multiplexed miRNA detection and quantification from serum extracellular vesicles. Calibration curves using rolling circle amplification were used to determine miRNA copy number estimates in agreement with other studies in literature with absolute quantification.

Finally, we tune hydrogel particle porosity and use novel functionalization techniques to capture extracellular vesicles based on their surface markers. We explored the use of the thiol-acrylate Michael addition reaction for antibody conjugation and optimized it for extracellular vesicle capture. Using these porous, antibody functionalized hydrogel particles, we captured breast cancer serum and match healthy serum extracellular vesicles using two surface markers, paving the way for multiplexed extracellular vesicle surface marker characterization. Porous hydrogel particles have

the potential to considerably enhance the workflow for exosome capture and profiling experiments, through multiplexing, fewer sample preparation requirements, and customizable nature, hence furthering extracellular vesicle research.

Incorporating the insights from the MIT Sloan Management program, the commercialization potential and current market landscape for extracellular vesicles was analysed. Extracellular vesicles have shown tremendous potential in the field of therapeutics, diagnostics, and for furthering academic research. The market study shows that the field is growing rapidly, with continued investment from venture capital for new companies, as well as corporate acquisitions by legacy players as they look to enter the field.

The work presented in this thesis employs the various benefits of hydrogels for biomolecule detection, namely their biocompatibility, solution-like kinetics, non-fouling nature, and tunable chemistry. We believe that this work can be leveraged to improve upon and develop new technologies for extracellular vesicle capture and analysis, leading to more insights into this promising biomarker, eventually leading to earlier and more accurate diagnosis of disease.

Thesis Supervisor: Patrick S. Doyle
Title: Robert T. Haslam (1911) Professor of Chemical Engineering

Acknowledgments

These past four years on the PhD train have been a whirlwind of a ride. Most people would assume that there would be valleys and peaks, but I found that there were some vertical loops and even some stretches of track where I had to push the train along, it was going so slow. The disruptions to research and to life in general caused by the Covid-19 pandemic was the equivalent of getting stuck in a roller coaster at the top of the peak, Needless to say, it has been an adventure, that I am grateful to have had the chance to embark on. There are so many people along the way that helped and supported me in some shape, way or form. First, I want to thank my advisor, Prof. Patrick Doyle for his constant support and guidance through these past three and a half years. He supported me in exploring new ideas and guided me in developing them into impactful and novel projects. Thank you for being so welcoming and accessible as an advisor as well. Next, I would like to thank my thesis committee members for their insights and guidance throughout my thesis work. Professor Joel Voldman, thank you for all your insightful questions during committee meetings. I also can't forget the support and guidance you gave at my first major conference at microTAS 2019. Professor Kwanghun Chung, thank you for all encouragement and guidance during committee meetings as well. You would commend my approach or my presented research and I would get the biggest confidence boost during committee meetings as a result.

Next, I want to thank all the Doyle lab members for always being open, supportive and willing to share and collaborate. To the graduate students who I pestered incessantly as I learned the ropes, Sarah Shapiro and Maxwell Nagarajan, thank you for bearing with me and being such amazing mentors and guiding me into the world of microRNA and hydrogels. A special shoutout to Lynna Chen for teaching me the lab fundamentals of the Doyle group, like SFL, and miRNA assays. Thank you to Augusto Tentori, Jeremy Schieferstein. Alex Klotz, Sima Asadi and Amir Erfani for your wise post-doc advice and willingness to let me rant on more than one occasion. To the non-window office labmates, Beatrice Soh, Li-Chiun Cheng,

Liam Chen, Devashish Gokhale, Indresh Yadav, Matt Wojtaszek, and Arjav Shah, thank you for all the fun stuff: gossip, banter and good food. Finally, to my miRNA subgroup, Dana Al-Sulaiman and Omar Mohd, you guys listened to me every week for the past year as I recounted my failures and successes on a slide deck and always were insightful, supportive and helpful throughout. A special thank you to Dana for being my partner-in-crime for EV-miRNA as we dealt with 17 hour experiment days. You made the past year so enjoyable in the lab. Thanks also to Gwen Wilcox, without whom the 5th floor of E18 would not function.

I want to thank my Edgerton roommates, Sydney Sherman and Delanie Linden for the baked goods, late night TV, taco bell, and shopping adventures. Thank you for providing much needed mini-breaks and the research-life balance that I needed. I also want to thank the MIT Figure skating club for letting me continue my passion for figure skating and giving me a place to forget about experiments that didn't go well or confusing results and just skate. To Boston Bollywood, I only found you in my 3rd year, but better late than never. I am so happy to have had the opportunity to dance as part of BB and become a member of the BB family.

To my chai crew, Shraddha Rana, Prashanth Prakash, Chinmay Kulkarni, Sachin Bhagchandani (and honorary members Ben Leaker and Jessica Wu), you guys have been a core part of my MIT experience. Thank you for your companionship and encouragement throughout grad school. Our chai sessions were a much need respite and welcome break from lab work.

I would like to acknowledge the funding sources for all work in this thesis. This work was partially supported by NIH-NIBIB Grant 5R21EB024101-02, NIH Grant 1R01CA235740-01A1, and a postgraduate scholarship from Natural Sciences and Engineering Research Council (NSERC) of Canada.

I would also like to acknowledge the nanomaterials core at the Koch Institute for MRPS measurements and Abigail Lytton-Jean for your training and guidance on the Spectradyne nCS1. NMR measurements were performed at the DCIF at MIT with the help of Devashish Gokhale. Finally, NTA measurements were performed

with the help of Kevin Silmore, Xun Gong, and Allan Brooks of the Strano Lab (MIT).

Finally, I would like to thank my family. To my husband, Shreesha Jagadeesh, for all your patience, support and encouragement on this journey. Your pushed me and encouraged me to keep going even when I thought there was a dead end. And finally my parents: thank you for instilling in me a love for math and science and for your support and care throughout my life.

Contents

List of Figures

List of Tables

Introduction

Cancer is a leading cause of death in the United States, however, it has also been widely shown that the chances of survival increase significantly with earlier detection. This is particularly true for lung cancer, where the 5-year survival rate is 50% for early stage lung cancer, but drops to 5% for late stage diagnoses [1, 2]. Traditional diagnostic procedures can involve invasive biopsies, or chest x-rays and CT scans, which are plagued with high false positive rates. methods include biopsies in which a tumor sample is taken for pathology and CT scans [2, 3].

Thus there is significant momentum to transition to liquid biopsies: a minimally invasive test for diagnostic biomarkers, which can be readily obtained from body fluids such as blood and urine [4]. With novel panels of biomarkers specific to the disease of interest,liquid biopsies have the potential to detect disease progression or treatment resistance long before it would trigger clinical symptoms or appear on x-ray or CT scans. Moreover, the possibility to subtype diseases without invasive biopsies opens up the possibility for even more subtype-specific treatments, resulting in higher survival rates and improved prognosis [2, 3].

In the last few years, extracellular vesicles have shown promise as a non-invasive biomarker for disease diagnosis and monitoring, and have become a treasure trove of information because they have been found to carry proteins, DNA, mRNA and microRNA as well surface markers indicative of the their cell origin [5]. Thus developing methods to profile extracellular vesicles and interrogate the contents of these vesicles is a growing area of research and has the potential to develop into a

non-invasive diagnostic platform, a liquid biopsy.

The aim of this thesis is to develop a system to capture extracellular vesicles and profile the miRNA patterns present within them. Hydrogel microparticles are central to this thesis and the benefits afforded by them, namely their biocompatibility, solution-like kinetics, non-fouling nature, and tunable chemistry, are utilized to the fullest extent. First, we develop various amplification strategies in hydrogel particles for microRNA detection, including a colorimetric detection platform that can be translated to point-of-care settings for a liquid biopsy. Then, we develop methods for extracellular vesicle lysis and microRNA detection using a one-pot lysis and microRNA capture method. Finally, we tune hydrogel particle porosity and use novel functionalization techniques to capture and profile extracellular vesicles based on their surface markers. This chapter will provide (1) An overview of the biomarkers we are concerned with, namely extracellular vesicles and microRNA, (2) A discussion of both novel and traditional detection methods for these biomarkers of interest, (3) An overview of hydrogel-based detection strategies and (4) An outline of the organization of this thesis.

1.1 Biomarkers of Interest

1.1.1 Extracellular Vesicles

Extracellular vesicles (EVs) are small lipid-bound vesicles released by cells and can carry cargo such as proteins, lipids, mRNAs, and miRNAs [6–8]. EVs can be divided into three types on the basis of size and route of biogenesis: exosomes, microvesicles, and apoptotic bodies [2, 8]. Exosomes, most typically found to be between 30-150 nm in diameter, are released by cell through an active process in which multivesicular bodies fuse with the cell membrane [5, 6, 9]. This process is shown in Figure 1-1. Exosome-mediated cell communication has been implicated in metastasis, angiogenesis, tumor proliferation and drug resistance [5, 7, 10, 11]. Exosomes from highly metastatic lung cancer cells have been shown to induce epithelial-to-mesenchymal transitions in other bronchial epithelial cells [2]. Exosomes have been found in var-

ious bodily fluids including blood plasma and serum, saliva, urine, amniotic fluid, semen, and cerbrospinal fluid [2, 12] and thus do not require invasive surgeries to harvest. Moreover, the contents of the exosomes are reflective of the cells of origin, making them useful as potential biomarkers for the diagnosis and monitoring of a variety of diseases, in which they play a role [5, 7, 9, 12].

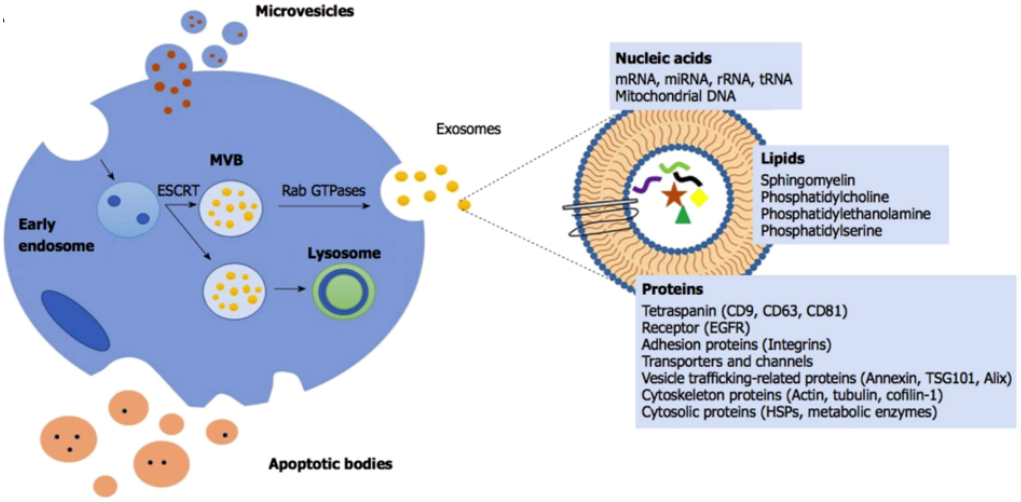

Figure 1-1: Extracellar vesicles comprise of exosomes (∼30-150 nm), microvesicles (∼100-1000 nm), and apoptotic bodies (>1000 nm). Exosomes are generated via the endolysosomal pathway and compartmentalized into the multivesicular bodies (MVBs), which fuse with the cell membrane and release the exosomes. Exosomes comprise of various transmembrane and cytosolic proteins, such as CD9, CD63, and CD81. They contain proteins, DNA, miRNA and mRNA reflective of the cell of origin. Figure adapted from [9]

1.1.2 microRNA

MicroRNAs are short non-coding RNA that have emerged as highly promising diagnostic and prognostic biomarkers due to their gene regulatory functions and dysregulated patterns in many diseases including cancer [13, 14]. miRNA regulate mRNA translation through either blocking the translation or degrading the target mRNA after binding to the 3' untranslated region [15, 16]. miRNAs are generated through the DICER-mediated cleavage of of pre-miRNA, stem-loop structures 60-100 nucleotides in length, which is exported out of the nucleus into the cytoplasm [16, 17]. miRNAs have exceptional stability in blood in body fluids due to their association with proteins such as the Argonaute protein family, and packaging within extracellular vesicles (EVs), protecting them from RNasesM [14, 18, 19]. miRNA can be

shuttled to other cells via EVs, RNA-binding proteins such as argonaute, and even certain classes of lipoproteins [20, 21]. This cell-to-cell transfer of miRNA has been implicated in tumor metastasis, tumor proliferation, and even drug resistance [16, 17]. As such miRNA are found in the blood and other body fluids and are a potent source of information since their miRNA dysregulation profiles can reflect state of diseases and tumors [16, 22]. Figure below shows a schematic of miRNA biogenesis and the communication pathways for miRNA to be shuttled to other cells.

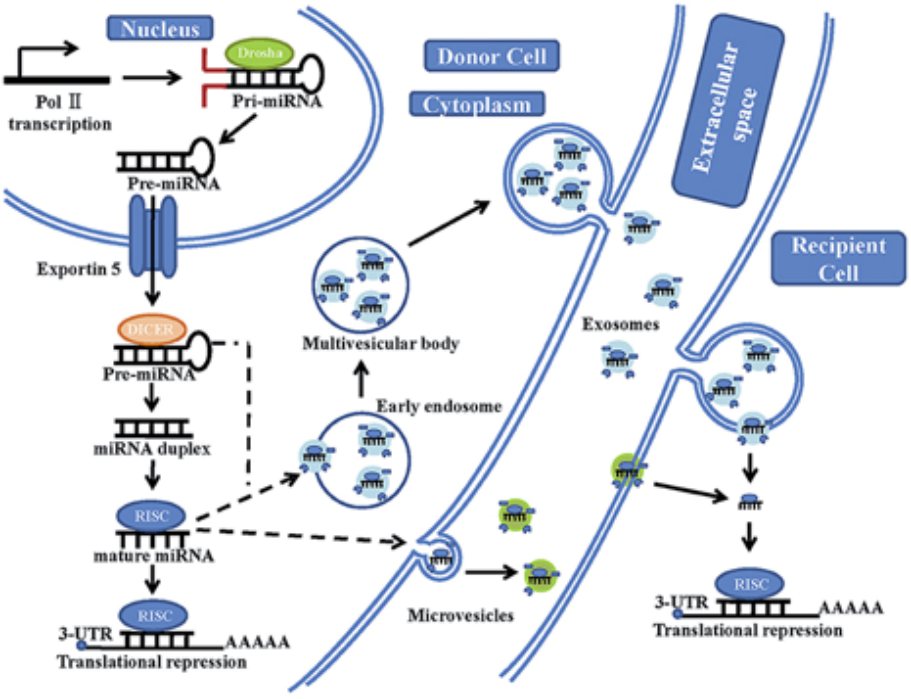

Figure 1-2: miRNA genes are transcribed by RNA polymerase II (Pol II), forming >1000nt long primary miRNA (pri-miRNA). These are processed by Drosha enzyme into pre-miRNA. The stem-loop RNA structures are then exported to the cytoplasm by the transport protein exportin-5. In the cytoplasm, pre-miRNA is cleaved by Dicer, which generates an intermediary miRNA duplex, of which one strand or both strands become the mature miRNA. These mature miRNA can be loaded into microvesicles, or multivesicular bodies, which eventually release exosomes. The miRNA, bound to RNA induced silencing complex (RISC), bind with the 3' UT region of the target mRNA to induce block translation or induce degradation. Figure adapted from [20]

1.2 Detection Methods

1.2.1 Methods for Extracellular Vesicle Detection

Apart from assessing the clinical utility of using exosomal proteins and miRNA as biomarkers, many research groups are developing and improving methods for the

isolation of exosomes and detection of its contents for various diseases including lung cancer, prostate cancer, and cardiovascular diseases. [2, 8, 23–25]. Traditional methods to isolate exosomes from biological fluids or cell culture media involve long and difficult ultracentrifugation and density-gradient centrifugation methods, which can take 8-10 hours with multiple rounds of ultracentrifugation at 100,000xg or greater speeds. Despite these methods being very inefficient and having the potential to contaminate exosomes with protein aggregates and other vesicles of similar size, they remain the gold-standard for isolating exosomes. [12]. With the increased focus on exosomes in cancer research, commercially available PEG-based reagents have become popular for exosome isolation [12, 26]. These polymeric reagents induce depletion interactions in which they "deplete" from areas in between the exosomes, causing the exosomes to precipitate and eventually be pulled down by low centrifugal forces [27]. Multiple groups have also found success with in-house PEG recipes [2, 28, 29]. A key drawback is that contaminants and PEG polymer aggregates can also co-precipitate with the exosomes, potentially hampering downstream analysis.

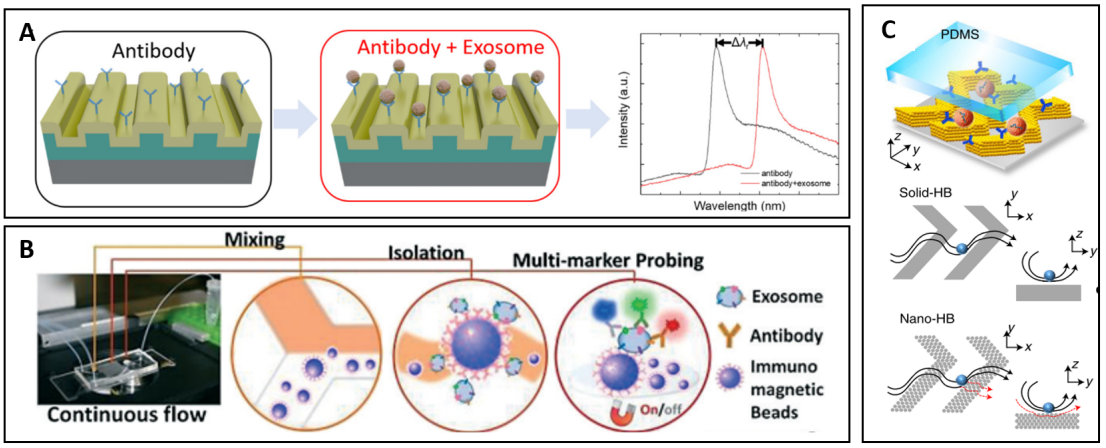

Figure 1-3: A) Schematic structure of a photonic crystal biosensor functionalized with antibodies. The binding of EVs to the antibody results in a shift in the reasonant reflection of the photonic crystal.[30] B) Schematic of a microfluidic chip for continuous mixing of antibody-coated magnetic beads and EVs, which are selectively enriched as the magnetic beads aggregate in the presence of an applied field. EVs are then probed for secondary markers with fluorescence detection. [31] C) Schematic of a nanostructured herringbone (HB) chip for EV capture. The solid HB chip results in hydrodynamic resistance close to the surface, limiting EV contact with the surface. The nano-HB chip allows fluid drainage through the porous structure, increasing probability of contact. [32]

Finally, size exclusion and immunoaffinity-based techniques are becoming more prevalent, particularly when used with microfluidic techniques. Immunoaffinity capture

of exosomes, based on surface protein markers, is a way to obtain a more targeted subset of exosomes by targeting exosome-specific surface markers such as tetraspanins (i.e. CD63, CD9, CD81) or even cancer-specific markers (i.e. EpCAM, CA125, EGFR)[7, 12, 33]. Many of these methods involve antibodies immobilized on planar surfaces (i.e. microfluidic channels, electrodes, glass slides) [**Wang2018RapidBiosensor**, 34–36], limiting antibody capture kinetics. Hence there has been a increasing emphasis on creating 3D or nanostructured surfaces for EV capture [32, 37–40]. These surfaces are difficult to manufacture and functionalize. In contrast, there are many systems that make use of antibody-coated magnetic beads for EV capture [23, 31, 41, 42]. The availability of commercial antibody-coated bead vendors with EV-specific antibodies already conjugated (i.e. Dynabeads), and fast capture kinetics through rigorous mixing, make this option particularly attractive [12]. However, commercially available beads have a limited selection for capture antibody, and moreover, multiplexing is limited to the spectral limitations of the instrument (i.e. for flow cytometry). An overview of immunocapture of EVs on planar, nanostructured and bead-based surfaces is shown in figure 1-3.

1.2.2 Methods for miRNA Detection

Conventional strategies for miRNA detection, including reverse-transcription qPCR (RT-qPCR) and microarrays, offer limited multiplexing and involve complex multistep procedures [43, 44]. Moreover, quantitative detection with these traditional approaches is very difficult and seldom demonstrated in literature [44, 45]. Their small size ($\sim$20-25 ribonucleotides), sequence homology and highly variable expression levels have made accurate detection and quantification difficult [44–47].

RT-qPCR is a form of target amplification, where the miRNA is first converted to cDNA with reverse transcriptase using either specific stem-loop primers, or poly-A tailing of the miRNA followed by an oligo-dT primer. The cDNA is then amplified using standard PCR cycles of primer extension and DNA denaturation. Quantification is done in real-time with either intercalating dyes like SYBR green, or with specific molecular beacon probes, as shown in Figure 1-4. Multiplexing is limited

by the number of different fluorophores one can discern simultaneously. Moreover, RT-PCR requires specialized equipment along with cumbersome sample preparation and protocols. Finally, across the miRNA field there is really no standardized system of controls or references. This make it very difficult to find and compare absolute miRNA concentrations from RT-PCR data and it can also lead to biased data [43, 46].

Other commonly used technologies adapted from detecting mRNA, are microarrays and next generation RNA sequencing (NGS). In microarray based detection, all of the miRNA are fluorescently tagged using an RNA enzyme. These tagged miRNA are then allowed hybridized with complementary DNA capture probes immobilized on a surface. A fluorescence scanner is then used to detect the bound miRNA. Microarrays allow for large scale multiplexing but require long hybridization times, and large sample input. The NGS process is similar to RT-PCR in that the miRNA are reverse transcribed into a cDNA library. Through adapter ligation, the miRNA are immobilized onto a surface and then undergo a process similar to PCR to generate identical amplicons. The last round of primer extension is done with fluorescent-tagged nucleotides, one nucleotide at a time, in order to sequence the template strand as the amplicon is generated. With the high costs and data processing requirements, sequencing is most often used for discovery studies involving identifying novel or clinically relevant miRNA as compared to diagnosis and routine detection.

There has been a considerable push within the field to develop novel miRNA detection strategies, with increased sensitivity, greater multiplexing capabilities, and simpler workflow. These novel platforms all utilize a capture nucleic acid probe (i.e. DNA, LNA, PNA) to bind to the target miRNA sequence, followed by signal readout using optical, electrochemical, or plasmonic methods [15, 43, 44]. In order to achieve the sensitivities required for most clinical miRNA sensing applications, numerous amplification strategies have been developed [43, 48].

Within, optical-based miRNA detection, solution-based amplification schemes, coupled with fluorescence detection are abundant, but they are limited by their spectral multiplexing ability [43, 48–50]. However, many of the amplification schemes such

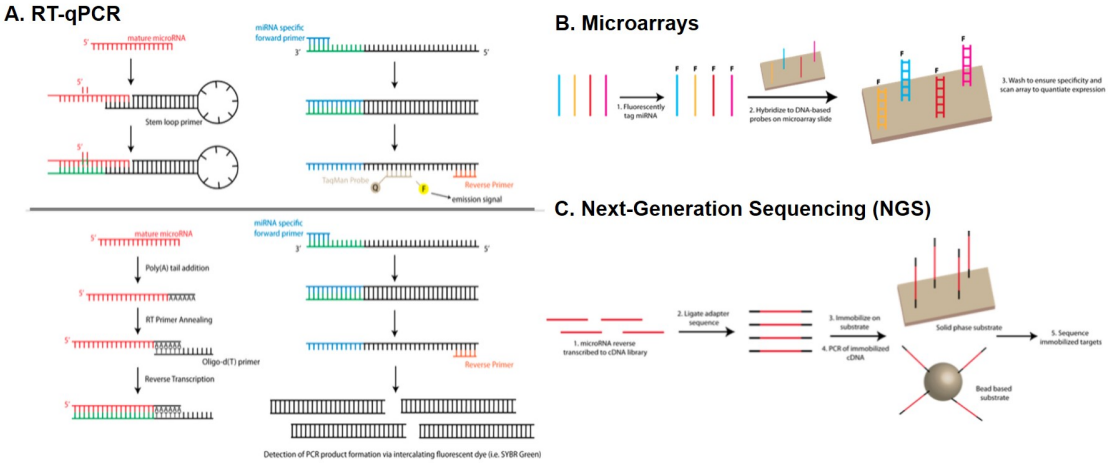

Figure 1-4: (A) RT-qPCR using TaqMan system, which uses stem-loop primers specific to the miRNA target of interest. During PCR amplification, the DNA polymerase proceeds along the template strands produced by miRNA specific forward and reverse primers and hydrolyses the TaqMan molecular beacon bound to the template. This liberates the fluorescent dye from the quencher and results in light emission. In SYBR green-based approaches, miRNAs are typically polyadenylated at the 3 end and d(T) oligo primers are used for cDNA synthesis. PCR amplification is carried out using miRNA specific forward primer and reverse primer. SYBR Green, an intercalating dsDNA dye, is then used to monitor PCR product formation. (B) Microarray detection involves capture of fluorescently tagged miRNAs on DNA-based capture probes immobilized on the microarray. The fluorescent signal is then quantitated and the intensity is related to the relative miRNA expression. (C) For RNA-seq, miRNA are reverse transcribed into a cDNA library. This is followed by adaptor ligation that allows for immobilization on a substrate that are used for rounds of amplification ending in sequenced fluorescent amplicon. Figure adapted from [43]

as hybridization chain reaction (HCR) [**Guo2017HybridizationMicroRNAs**, 51], rolling circle amplification (RCA) [52, 53], have shown promise after adaptation to surface-bound methods as shown in figure 1-5. As such, surface-bound detection methods could be readily scaled for spatial multiplexing. Many of the surface-bound methods use electrochemical or plasmonic readouts, however, they are useful for insights into novel amplification strategies or detection modalities as well as the synergistic and combined use of various amplification strategies and signal readouts that can then be adapted for use with hydrogel particles. Examples include the use of quantum dots [**Guo2017HybridizationMicroRNAs**, 54, 55], enzymatic amplification[44, 52, 56, 57], and nucleic acid isothermal amplification schemes [51, 55, 58] that can be applied to an anchored capture probe as shown in figure 1-5. There are numerous review articles that dive deeper into these methods for further insights [15, 43, 44, 48, 59, 60].

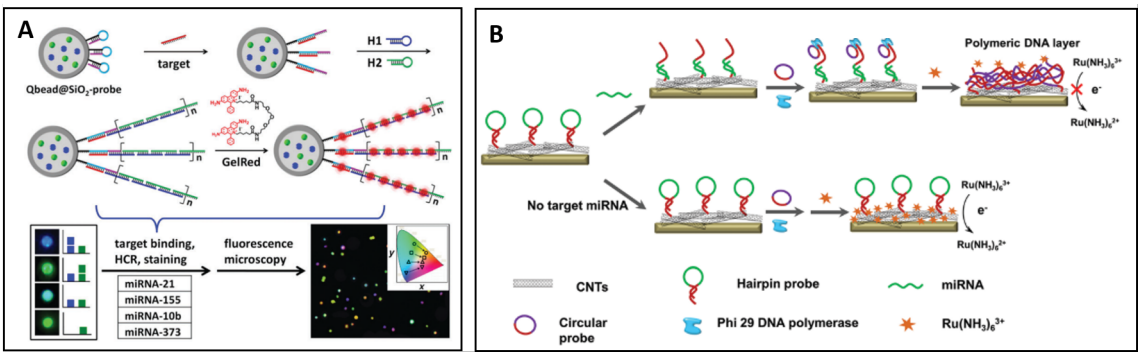

Figure 1-5: A) Schematic structure of silica coated quantum dot-doped beads (Qbead@SiO_2) functionalized with hairpin probes for miRNA capture and HCR. The HCR tail is labelled with GelRed dye. The colorimetric combination of Qbeads determines the miRNA probe, while the GelRed fluorescence determines the miRNA concentration. B) Schematic of a miRNA assay with carbon nanotube (CNT) enhanced electrochemical detection. The hairpin probe bound to the CNTs captures the miRNA, unfolding and triggering RCA with a circular probe. The polymeric DNA layer prevents electron transfer, resulting in a drop in signal. [52]

1.3 Hydrogel-based Detection of Biomarkers

Hydrogels are a versatile platform for biomolecule detection assays due to their biocompatibility, solution-like kinetics, non-fouling nature, and ability to incorporate capture agents inside a 3D network [61, 62], Hydrogels have previously been used for the multiplexed detection of variety of biomarkers such as microRNA, mRNA, proteins and cytokines from a variety of complex samples such as live cells and cell lysate, serum, and FFPE tissue [45, 62–69]. Moreover, there exist multiple systems for creating hydrogel sensing structures such as hydrogel posts using optical lithography techniques, hydrogel spots through contact microprinting and finally hydrogel microparticles through microfluidic emulsion polymerization or stop-flow lithography [70–72]. The diversity in sensing structures permits hydrogels to be used as sensing platforms in a variety of form factors and end-uses.

Stop flow lithography (SFL), a technique pioneered in the Doyle Group, is a scalable method for the manufacture of hydrogel particles in arbitrary 2D-extruded shapes, permitting the use of a various graphical and shape encoding schemes for multiplexed detection. [73, 74]. Figure 1-6A shows a schematic of this process. A pre-polymer solution is introduced into a polydimethylsiloxane (PDMS) microfluidic channel. The flow is stopped and particles are polymerized by exposing the solution with UV

light through a photomask. The photomask determines the 2D extruded shape of the particle, allowing for spatial codes and identifiers to be incorporated into the particle. Flow is resumed, flushing away the particles, and the process is repeated. The PDMS allows oxygen to permeate into the channel, inhibiting polymerization at the edges, allowing the particles to be free-flowing [75]. The spatial code enables multiplexed assays with numerous different miRNA sequences [45, 74].

miRNA detection within hydrogels is based on complementary strand hybridization between the miRNA target and a probe strand bound to the hydrogel. A biotinylated universal linker sequence enables tagging with streptavidin-R-phycoerythrin (SAPE). The signal is quantified by fluorescence imaging, whereby the code indicating the miRNA target is easily identifiable. Nucleic acid based amplification techniques such as rolling circle amplification, and enzymatic amplification techiques have been shown to be compatible with the hydrogel particles, allowing for lower limits of detection [76, 77]. Proteins and other biomarkers have similarly been detected through the use of a capture probe and subsequent labelling with a biotinylated reporter probe and SAPE [62, 63, 78].

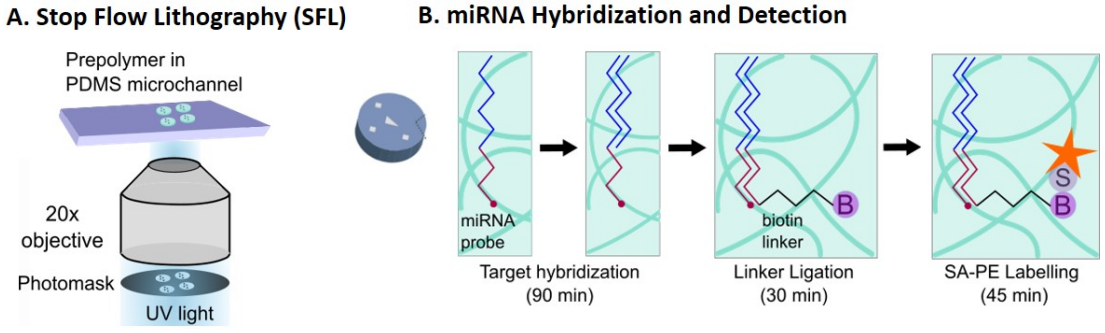

Figure 1-6: A) Schematic of particle fabrication using stop-flow lithography. The flow is paused temporarily and exposed to UV light through a photomask defining the particle shape. Flow is then resumed and the cycle is repeated. B) The miRNA specific probe on the hydrogel hybridizes with the target miRNAs in solution. Then a universal biotintylated linker is ligated onto the target with T4 Ligase. A streptavidin fluorophore (SAPE) binds to the biotin producing a stable fluorescent signal.

1.4 Organization of Thesis

This thesis develops a system to capture extracellular vesicles and profile the miRNA patterns present within them and is organized in the following manner:

Chapter 1 provides a general introduction to the thesis and a background on extracellular vesicles and miRNA, current techniques for detection and an overview of hydrogel-based detection.

Chapter 2 describes materials and methods that are central to multiple studies within this thesis and referred to throughout.

Chapter 3 presents a platform for multiplexed colorimetric microRNA detection using shape-encoded hydrogel particles.

Chapter 4 enumerates miRNA amplification strategies for improved sensitivity.

Chapter 5 describes the development and application of a method for quantitative and multiplex detection of extracellular vesicle-derived miRNA, via rolling circle amplification within encoded hydrogel microparticles.

Chapter 6 describes the use of porous hydrogel microparticles for mulitplexed capture and profiling of small extracellular vesicles.

Chapter 7 summarizes the work completed in this thesis and provides an outlook for future work and development of the concepts developed in this work.

Materials and Methods

2.1 Materials

This chapter contains common materials and detailed methods utilized throughout this thesis. Each chapter also contains a description of experimental procedures that are specific to that chapter.

2.1.1 Chemicals and Buffers

Table 2.1 provides abbreviations for commonly used reagents that will be used throughout this thesis, along with supplier and storage information.

Table 2.1: List of commonly used reagents in thesis.

Abbreviated Name	**Storage**	**Composition**
PDMS	RT	polydimethylsiloxane(Sylgard 184, Dow Corning)
PEGDA-700	4°C, protect from light	polyethylene glycol diacrylate, Mn=700 (Sigma)
PEG-600	4°C	polyethylene glycol, Mn=600 (Sigma)
Darocur 1173	4°C, protect from light	2-hydroxy-2-methiopropiophenone (Sigma)
SDS	RT	sodium dodecyl sulfate (Sigma)
SAPE	4°C, protect from light	streptavidin phycoerythrin (premium grade from ThermoFisher Scientific)
S-AP	4°C, protect from light	streptavidin alkaline phosphatase (Sigma)
NBT-BCIP	-20°C	nitro-blue tetrazolium and 5-bromo-4-chloro indoylphosphate, tablets stored frozen (SigmaFAST NBT-BCIP, Sigma Aldrich)
ELF-97	-20°C	proprietary fluorogenic substrate for S-AP from Sigma Aldrich
NHS-PEG-SH	-20°C, store dry under argon	PEG-2000 heterobifunctional linker with a NHS ester end group and thiol end group (Nanocs)

One key note that was learned during this thesis was the importance of proper storage conditions and using fresh/new PEG reagents. Even non-photosensitive PEG reagents like PEG-600 undergo some aging process, which gives rise to uneven probe distribution and "speckled pattern" results when using prepolymer formulations made with old PEG. In general PEG reagents for prepolymers should be stored at 4°C (protected from light) and should be thawed completely before using. It is best practice to aliquot the PEG reagents into small volumes so that each volume undergoes a limited number of freeze-thaw cycles.

Table 2.2 describes the formulation of common buffers used throughout this thesis. All buffers were made with nuclease-free water and filtered through a 0.2 μm pore filter (either a syringe filter or a vacuum filter for large volumes)

Table 2.2: List of commonly used buffers in thesis.

Buffer Name	**Storage**	**Composition**
PBS	RT	phosphate-buffered saline pH 7.4 (Corning)
PBST	RT	PBS with 0.05% Tween-20
1x TE	RT	1x Tris-EDTA buffer consisting of 10 mM Tris, 1 mM EDTA, diluted from 100x stock solution (EMD Millipore)
3x TE	RT	3x Tris-EDTA buffer consisting of 30 mM Tris, 3 mM EDTA, diluted from 100x stock solution (EMD Millipore)
1x TET	RT	1x TE with 0.05% Tween-20
Rinse Buffer	RT	1x TET with 50 mM NaCl
Hybridization Buffer	RT	1x TET with 500 mM NaCl
PTET	RT	5x TE with 25% v/v PEG 400 and 0.05% Tween-20 (note that new PEG 400 should be used to prevent pH variation)
TBST	4°C	1x Tris-buffered saline with 0.1% Tween-20 (TBS diluted from 10x stock from Sigma)
2% BSA-PBST	4°C	20 mg/ml BSA solution made in PBST (BSA in lyophilized form from Sigma)
5% BSA-PBST	4°C	50 mg/ml BSA solution made in PBST (BSA in lyophilized form from Sigma)

2.1.2 Oligonucleotides

All DNA capture probes and synthetic RNA targets were purchased from Integrated DNA Technologies (IDT) with RNase-free HPLC purification. They were ordered in lyophilized form, and subsequently reconstituted in 1x TE, and stored at -20°C in aliquots. DNA capture probes had a 5' acrydite modification for copolymerization with the PEGDA-700 and a 3' invdT modification to prevent nuclease degradation and unwanted ligation/polymerization reactions on the probe. DNA probes with a biotin or FAM (6-carboxyfluorescein) modification at the 3' end were also used for characterization and troubleshooting. DNA probes were stored at 10x the concentration required in the prepolymer solution (500 μM - 2.47 mM). RNA targets were typically serially diluted for calibration curves and stored in aliquots containing

fixed amount of target (i.e. 5 μL of 20 pM = 100 amol). Larger aliquots of certain commonly used concentrations (i.e. 20 pM, 500 pM, 1 nM) were also stored.

Primers for strand displacement amplification were purchased from Sigma (they were below the minimum size requirements for IDT purification). These primers were short (6-12 nt) DNA oligos with a 5' biotin or FAM (6-carboxyfluorescein) modification. They were ordered as 100 μM stock solutions in 1xTE and subseqently diluted to working concentrations of 10 μM and aliquoted for storage at -20°C.

Sequences for all oligonucleotides can be found in the Appendix.

2.2 Experimental Methods

2.2.1 PDMS Microfluidic Device Fabrication

Microfluidic channels for particle synthesis were fabricated in polydimethylsiloxane (PDMS) using previously published methods. PDMS (Sylgard 184, Dow Corning) was mixed in a 10:1 base: crosslinker ratio and poured over a SU-8 photoresist mold, fabricated using standard photolithography techniques. PDMS mixing was done by hand using a glass stir rod for about 1 min. After pouring the PDMS over the mold, the PDMS was degassed under vaccuum for 2x 1min intervals using a dessicator attached to a vacuum pump. The PDMS was allowed to sit at room temperature for at least another 20 minutes until all the bubbles had disappeared. before placing in the 65°C oven to cure overnight. The PDMS channels were cut using a clean scalpel and then cleaned by sonicating in ethanol. Inlets and outlets were punched using a biopsy punch (1.5 mm inlet, 4 mm outlet). The PDMS channels were placed on a glass coverslip coated in half-cured PDMS (10:1 ratio, cured for 25-30 min at 65°C). The resulting device was baked overnight at 65°C to complete the bonding process.

The half-cured PDMS coverslips were made by sandwiching 100 μL of PDMS between two coverslips and shearing until it formed a uniform layer. It was important to test the curing level of the PDMS on the coverslips by scratching a corner with

a pipette tip and adjust cure time accordingly (The scratch should not disappear, otherwise the PDMS is underbaked. Overbaked PDMS would not scratch in the first place).

For standard particles, channel heights and widths were 42 µm and 300 µm respectively. For colorimetric detection particles, channel heights and widths were 60 µm and 300 µm respectively. Channel lengths varied from 3 to 4 mm, depending on the hole punching. Synthesis chips could be reused many times (5+ times) by cleaning via ethanol sonication after each use. PDMS parking chips were made in a similar manner as the particle synthesis chips, with chip design based on [77]. They typically had channel heights of 38 µm.

2.2.2 Glass Microchannel Preparation

Glass microfluidic chips containing straight channels were commercially purchased from Hilgenberg GmbH. They contained channels 50 μm in height and 20 mm in length, with various widths (0.5 mm, 1 mm, 1.5 mm). PDMS inlets and outlets were punched using a biopsy punch and attached to the glass channel inlets and outlets using plasma treatment (30s in Harrick PDC-32G plasma cleaner).

Channels were activated by soaking in 1 M NaOH for 1 hour and then rinsing 2x with DI water. Channels were then silanized using a a silane solution (2:3:5 mixture of 3-(trimethoxysilyl)propyl methacrylate) for 30 minutes [79]. The solution was made fresh before use and the stock 3-(trimethoxysilyl)propyl methacrylate) was stored under argon. Channels were then washed 2x in methanol and then 2x with DI water and then placed in a dessicator under vacuum and protected from light until hydrogel post polymerization.

2.2.3 Stop Flow Lithography for Hydrogel Particle Synthesis

Particles were synthesized using stop flow lithography (SFL) as shown in Figure 2-1. For miRNA probe particles, a prepolymer solution consisting of 20% PEGDA-700, 40% PEG-600, 5% Darocur 1173 photoinitiator, and 35% 3x Tris-EDTA buffer is mixed in a 9:1 ratio with the acrydite-modified DNA probe. This pre-polymer

solution was introduced into the PDMS channel using compressed air-driven flow [80]. The flow is stopped and a particle is polymerized by exposing the channel with UV light (M365L2-C4, Thorlabs, 365 nm LED) for 95 ms through a photomask (mylar transparency mask, Fineline Imaging) inserted in the F-stop. The mask defines the 2D-extruded shape of the particles. Flow is then resumed to clear the particle and bring fresh prepolymer into the UV exposure zone. Each cycle consists of a hold (205 ms), flow (200 ms), stop (500 ms), expose (95 ms) step in that order, with the full cycle lasting 1 s.

The flow-stop-expose process is run in a continuous cycle to achieve semi-continuous particle synthesis. Particles are collected from the outlet and washed twice with TET (TE buffer with 0.05% Tween-20). Each wash consists of adding 400 µL of buffer to the microfuge tube containing the particles, vortexing briefly, centrifuging for 45s to sediment the particles, and removing 400 µL of supernatant. For miRNA assays, particles are then oxidized by incubating them for 5 minutes with 500 µM $KMnO_4$ in 0.1 M Tris-HCl pH 8.8. Particles were washed 3x in TET and stored in TET at 4°C.

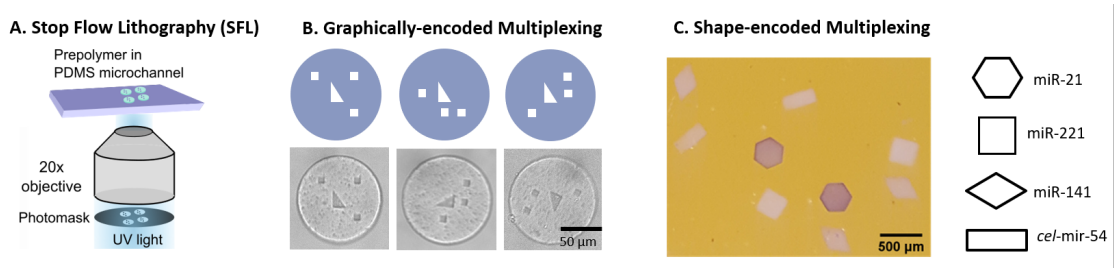

Figure 2-1: A) Schematic of SFL particle synthesis. B) Representative images of graphically encoded and C) shape-encoded particles. Scale bar is 50 µm for B) and 500 μm for C).

For particles used in thiol-acrylate reactions, no Tris-based buffers are used during synthesis. Instead, 3x TE in the prepolymer is replaced with PBS, and TET buffer for washes and storage is replaced with PBST. The particles are not oxidized.

2.2.4 Projection Lithography for Hydrogel Post Synthesis

Hydrogel posts in glass microfluidic channels are synthesized using projection lithography using the same microscopy setup as SFL. The prepolymer solution (similar

composition as in SFL) is loaded into the channel using either pressure-driven flow. Posts are polymerized with 100 ms exposure using 100 μm diameter circle mask inserted in the F-stop. After all the posts of a particular composition are polymerized, the subsequent prepolymer solution is loaded in a fresh pipette tip and flushed through the channel for at least 1 minute to clear out the previous solution. Once all posts have been polymerized, the channel is washed 3x in TET. The posts are blocked with 3% w/v Pluronic F-108 for 30 minutes, washed 3x in TET and then oxidized for 5 minutes with 500 µM $KMnO_4$ in 0.1 M Tris-HCl pH 8.8. Channels are again washed 3x in TET and then stored at 4°C with TET loaded pipette tips inserted in both the inlets and outlets.

2.2.5 Standard microRNA Assay

Particles were co-polymerized with oligonucleotide DNA probes specific to different miRNA as described above. A graphical code in the center of the particle encodes for the miRNA target. The particles were diluted in hybridization buffer (20 particles for each miRNA in each reaction) to which the synthetic miRNA targets were added at different concentrations. The final NaCl concentration in the 50 µL reaction volume was 350 mM, which previous studies have shown to produce high signal while reducing cross-reactivity [45]. Target hybridization was conducted for 90 min at 55°C on a thermoshaker. Particles were washed 3x in Rinse buffer and 245 µL of ligation solution (40 nM biotinylated universal linker, 250 nM ATP, 800 U/ml T4 DNA ligase in NEBuffer 2 (New England Biolabs)) was added to the 50 µL of particles. The ligation reaction was conducted at 21.5°C on the thermoshaker for 30 minutes. Particles were washed 3x with Rinse buffer again. For labelling, particles were incubated with 5 µL of 20 µg/ml SA-PE (working solution made in TET and stored at 4°C) for 45 minutes at 21.5°C on the thermoshaker. Particles were washed 3x with rinse buffer to remove unbound SA-PE.

The ligation mix was made by diluting pre-made aliquots of NEB2A (100 µL 10x NEB2 buffer + 25 µL of 10 µM ATP) with 869 µL of TET. 4 µL of 10 µM linker and 2 µL of ligase were added to this. The mix was vortexed for 30s and then centrifuged

for 30s right before addition to the particle tubes. Care was taken to pipette from the top of the centrifuged mixture so that debris that was just centrifuged down would not be included in the ligation reaction. Each 1 ml of ligation mix was used for at most 3 tubes of reactions, leaving ~265 µL leftover (this leftover was not used since it contained all the debris was centrifuged down).

All centrifugation steps for washes were done on a VWR benchtop centrifuge (500xg rcf).

2.2.6 Imaging and Analysis

Particles were imaged using a CCD camera (Andor Clara) under the 20x objective of an inverted microscope (Zeiss Axio Observer) equipped with a LED excitation source (X-Cite 120 LED) and appropriate filter sets for either FAM (Omega XF100-2) or phycoerythrin (Omega XF101-2 for early data). A special-order filter set from Semrock was later used for SAPE, which increased signal by 2-fold, while keeping the same absolute background levels as the Omega filter set. This special order set consisted of a FF01-520/60 exciter, FF01-607/70 emitter, and FF562-DiO3 dichroic filter. All filters are standard stock at Semrock. They are not sold as a set though. The comparison of the two filter sets is shown in figure 2-2.

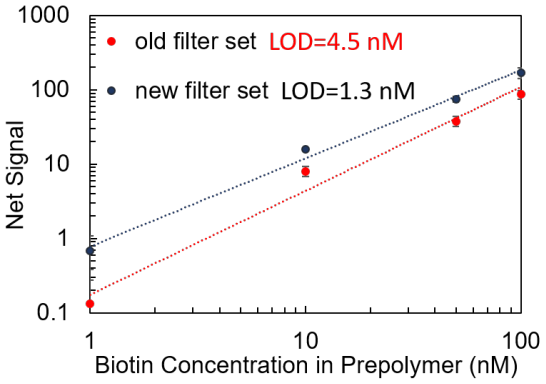

Figure 2-2: Comparison of performance between the Omega filter and set and the Semrock filter set for SA-PE signal. Particles with biotin probe at various concentrations were synthesized using SFL and then labeled with 45 minutes with SAPE.

Earlier in the course of this thesis, PTET was used for imaging. Briefly, the particles were resuspended with 200 µL of PTET and then centrifuged for 2 minutes. Particles

were pipetted from the bottom of the tube onto a 20x60 mm glass coverslip and then sandwiched with a 18x18 mm coverslip. It was later discovered that the age/quality of the PEG used for PTET caused the buffer to drop in pH (from $\sim$ pH 8 to $\sim$ pH 4). While this marginally affected the fluorescence of SA-PE, it caused a significant drop in signal for FAM (a fluorescein fluorophore used in some studies). FAM is known to be pH sensitive. Thus for much of the final data shown in this thesis, no PTET was used for imaging.

About 20-30 µL of the particle solution (in rinse buffer) was pipetted onto the 20x60 mm glass coverslip and the droplet spread out with the help of a pipette tip. No coverslip was used on top to sandwich the particles. The two potential issues with this method are uneven liquid height above particles during imaging and drying of the droplet. The uneven liquid height was mitigated by spreading the droplet. In practice, we saw at most 10 AFU difference in background signal in different locations of the droplet, due to liquid height differences. Background subtraction during image analysis removed this difference in the data. The droplet evaporation was sufficiently slow that it was possible to image 3-4 different particle types (6-8 particles each) without any noticeable difference in the droplet size. For higher multiplexing with more particle types, imaging was done in batches (i.e. 10-20 µL of particles at a time).

Average fluorescence signal of the particles was measured in ImageJ (NIH) using the circle selection feature. The entire particle was included (the holes for the graphical code included) instead of just taking a small region of interest (ROI) within the particle. This was done so that the boundary layer present for many of the miRNA would be included in the analysis. It would also reduce variability in data due to slightly different ROI location between particles and conditions. The background signal was the the signal from that same circle ROI taken right beside the particle. Particles were kept in the center of the field of view while acquiring images. Net signal was calculated as background subtracted signal of the particle in question minus the background subtracted signal of the control particle (either a particle from a no target condition, or a negative control probe particle).

2.2.7 Determination of Limit of Detection

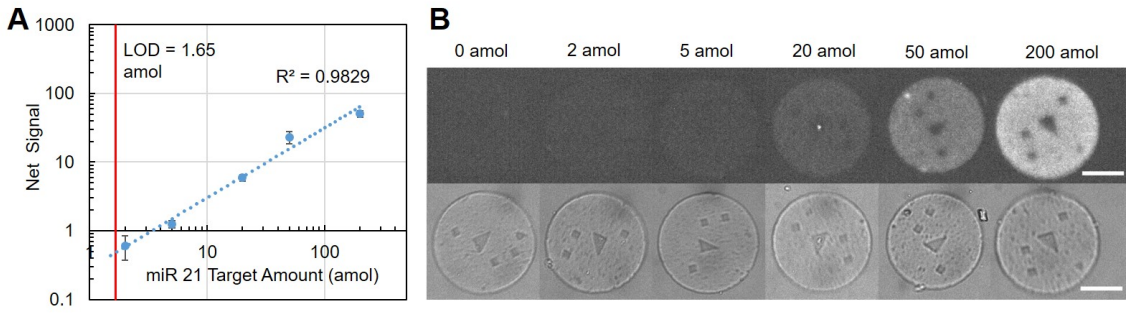

Figure 2-3: Particle calibration curve for miR-21. A) The net signal is the background subtracted signal minus the negative control signal (0 amol). The LOD for miR-21 was 1.65 amol. At least 5 particles were analyzed for each concentration. Error bars represent one standard deviation. B) Representative fluorescent (top) and brightfield (bottom) images of particles at each target concentration. All fluorescent images are at the same brightness. Scale bars are 50 µm.

The average net signal was plotted against the miRNA amount on a log-log scale and a linear line of best fit was fitted to the log-transformed data.

$$log_{10}y = mlog_{10}x + b$$

The limit of detection (LOD) was determined as the miRNA concentration where the net signal is equal to 3 times the standard deviation of the control particles (3σ method). The concentration is calculated by inverting the equation of best fit.

$$x = 10^{(log_{10}y - b)/m}$$

An example of the images taken for analysis and the resulting data and LOD determination is shown in figure 2-3

Multiplexed Colorimetric microRNA Detection using Shape-encoded Hydrogel Particles

The goal of my thesis is to develop a system to capture extracellular vesicles and profile the miRNA patterns present within them. In this chapter, we focus on an enzymatic amplification strategy that enables multiplexed, colorimetric detection. We report a platform utilizing a reporter enzyme, which produces a chromogenic indigo precipitate that preferentially localizes within hydrogel microparticles. The 3D network of the hydrogel maintains the rapid target binding kinetics found in solution, while multiplexed target detection is achieved through shape-encoding of the particles. Moreover, the precipitate-laden hydrogels can be imaged with a simple phone camera setup. We used this system to detect microRNA (miRNA) down to 0.22 fmol. We then showed the compatibility of this system with real samples by performing multiplexed miRNA measurements from total RNA from matched colon cancer and normal adjacent tissue. This chapter is adapted from Juthani, N., I& Doyle, P. S. (2020). A platform for multiplexed colorimetric microRNA detection using shape-encoded hydrogel particles. Analyst, 145(15), 5134–5140. [81]

3.1 Introduction

As diagnostics move out of the lab into clinical settings, the use of specialized equipment for signal detection greatly hinders technology translation[82, 83]. To this end, colorimetric detection systems typically require fewer instrumentation requirements and are more amenable to translation to resource limited settings [84, 85]. This is most evidently seen by the success of lateral flow assays, which use colloidal nanoparticles for target labelling[86]. These surface-based detection systems (i.e. lateral flow assays and contact printing methods) facilitate spatial multiplexing, but one loses the favorable hybridization kinetics offered in solution[57, 71, 87–89]. Conversely, solution-based colorimetric detection systems can realize fast hybridization kinetics but are not capable of simultaneous multiplexing [90–95].

Hydrogels offer a superior alternative to solution and surface-based biomolecule detection systems due to their biocompatibility, solution-like kinetics, non-fouling nature, and ability to incorporate capture agents inside a 3D network [61, 62]. Hydrogels have previously been used to detect microRNA, mRNA, proteins and cytokines from a variety of complex samples such as total RNA extract, live and lysed cells, serum, and FFPE tissue [45, 62–69]. However, like many other detection platforms, hydrogel-based detection assays typically employ a fluorescent reporter to label the captured target. This could involve direct labelling with a fluorescent dye, or labelling with an enzyme, which in turn produces a fluorescent product. The latter labelling technique necessitates containment of the fluorescent product and hence has found most utility in droplet-based or oil-encapsulated systems, where the soluble fluorescent product can be contained for sufficient signal generation and multiplexing [49, 70, 77, 96–98]. Thus, a limited amount of substrate is accessible for the reaction. Moreover, specialized equipment such as fluorescent microscopes, fluorescent plate readers or fluorescent scanners are necessary to detect the fluorescent signal [45, 49, 67, 98].

Efforts to develop a colorimetric readout for hydrogels have used gold nanoparticle labelling combined with dark-field microscopy. While the sensitivity of this method

was comparable to fluorescent labelling, it still requires the use of a microscope for detection using dark-field imaging [99]. To this end, we present a hydrogel-based multiplexed colorimetric detection platform which can be imaged using a cell phone.

In this work, we utilize a reporter enzyme, which catalyzes the production of a chromogenic precipitate. Specifically, the target is labelled with streptavidin-enzyme conjugate streptavidin-alkaline phosphatase (S-AP), which acts upon a substrate solution of nitro-blue tetrazolium and 5-bromo-4-chloro-3-indolyl phosphate (NBT-BCIP), a precipitating substrate traditionally used with S-AP in blotting and in-situ hybridization techniques [100]. NBT-BCIP starts as a clear, pale yellow substrate. S-AP cleaves the phosphate group on BCIP, which upon dimerization produces an indigo dye. The dimerization also reduces NBT into an insoluble indigo-purple diformazan in the vicinity of the enzyme [101, 102]. The enzymatic reaction occurs within the hydrogel particle, which contains the reaction, resulting in the localization of the precipitate.

These hydrogel particles are created using stop-flow lithography (SFL), a technique that can produce 2D-extruded particles in arbitrary shapes dependent on the photomask used [73]. This enables a variety of graphical and shape encoding schemes for multiplexing. In this platform, we use shape-encoding, whereby a different particle shape encodes for the target it captures, to enable facile multiplexing, while maintaining the familiar solution assay-based workflow [103, 104]. As such, this platform is able to combine the benefits of solution-based colorimetric detection systems, with its rapid kinetics, with the multiplexing offered by surface-based colorimetric detection. Moreover, the hydrogel particles can be imaged using a cell-phone camera with no other expensive optics or detection systems necessary.

This method of precipitation-based colorimetric detection is particularly useful for microRNA (miRNA) detection. miRNA are small, noncoding RNAs that are an emerging class of biomarkers as they have been shown to be dysregulated in many diseases including numerous cancers, cardiac diseases, and Alzheimer's [3, 8, 14]. However, miRNA only represent a small fraction of total RNA (0.01%) present in tissue and their small size ($\sim$22nt) make quantification difficult [46]. Hydrogel parti-

cles are an ideal substrate for miRNA hybridization assay due to the fast solution-like kinetics, non-fouling nature, and ability to perform multiplexed measurements [61, 62]. Moreover, this platform can be outfitted to any detection assay that can accommodate labelling with an enzyme reporter, such as protein and cytokine detection with appropriate biotinylated antibodies followed by the streptavidin-enzyme conjugate. To demonstrate the ability of our hydrogel particles to contain and localize the chromogenic precipitate, we first co-polymerized hydrogels with a biotin moiety and characterized the precipitation reaction in time. Then we used this colorimetric detection method to detect miRNA in a hydrogel-based hybridization assay. We then showed the ability to perform multiplexed detection of miRNA from total RNA from matched colon tumor and normal adjacent tissue using shape-encoded particles.

3.2 Experimental

PDMS microfluidic device fabrication and particle synthesis were carried out as described in Chapter 2. One key difference is that the microfluidic channels were 60 µm in height (vs. 42 µm) and the particles for colorimetric detection were about 300 μm in width instead of the nominal 100 μm diameter particles used in the standard assay. Each exposure only produced 1 particle. The particles used have a fixed 2D perimeter of 1000 µm and same height, resulting in a consistent surface area to volume ratio (0.051 ± 0.0029 µm^{-1}) for comparable target and enzyme diffusion.

3.2.1 Precipitate Reaction Characterization

Characterization experiments were done with particles co-polymerized with different concentrations of biotin probe incorporated, with the shape encoding the concentration. The biotin concentrations were calculated based on the biotin probe concentration in the prepolymer solution and the incorporation rate (11%) for this formulation of hydrogel particles based on previous work [105]. The particles were suspended in TBST (15 particles of each concentration) to which streptavidin alkaline phosphatase (S-AP, Invitrogen) was added to a final concentration of 10 µg/ml in a 50 µL reaction volume. Particles were mixed with the enzyme on a tube re-

volver (speed 30 with shaking, ThermoFisher) for 30 minutes at room temperature (21.5°C). The tube holder was angled at 90° so that the tubes rotated in the same plane in a rolling motion. The particles were then washed three times with TBST. Then 50 µL of substrate solution was added to 50 µL of particle solution. The particles were placed back on the tube revolver for varying amounts of reaction time at room temperature. After the specified time, particles were washed once with 100 µL of TBST and then deposited onto an imaging well on a glass slide.

The substrate solution contained nitro-blue tetrazolium and 5-bromo-4-chloro-3-indolylphosphate (NBT-BCIP), a precipitating substrate commonly used with S-AP in blotting and in-situ hybridization [100]. The solution was made by dissolving a tablet of NBT-BCIP (SigmaFAST BCIP/NBT, Sigma Aldrich) in nuclease-free (NF) water. For studies assessing reaction time, "1x substrate" was used, in which the tablet was dissolved in 10 ml of NF water (the recommended concentration for the product resulting in 0.15 mg/ml BCIP, 0.30 mg/ml NBT, 100 mM Tris, and 5 mM $MgCl_2$). For studies assessing substrate concentration, the tablet was dissolved in either 5 ml or 2 ml of NF water resulting in 2x and 5x substrate solutions respectively. In all cases, the solution was filtered through a 0.45 µm small volume syringe filter.

3.2.2 microRNA Detection Assay

Particles were co-polymerized with oligonucleotide DNA probes specific to different miRNA. The shape of the particle encoded for the miRNA target. The particles were suspended in hybridization buffer (10 particles for each miRNA in each reaction) to which the synthetic miRNA targets were added at different concentrations. The final NaCl concentration in the 50 µL reaction volume was 350 mM, which previous studies have shown gives high signal while reducing cross-reactivity [45]. Target hybridization was conducted for 90 min at 55°C on a thermoshaker as shown in Figure 3A. Particles were washed three times in Rinse buffer (TE buffer with 0.1% Tween-20 + 50 mM NaCl) and 245 µL of ligation solution (40 nM biotinylated universal linker (IDT), 250 nM ATP, 800 U/ml T4 DNA ligase in NEBuffer 2 (New

England Biolabs)) was added to the 50 uL of particles. Particles were placed on the tube revolver at room temperature for 30 min for the ligation reaction. Particles were washed 3 times with Rinse buffer again and then S-AP enzyme solution was added to a final concentration of 10 µg/ml in a 50 µL reaction volume. The particles and enzyme were mixed on the tube revolver at room temperature for 30 min. Particles were washed again with 3x Rinse buffer and then 50 µL of 5x substrate solution was added to 50 µL of particles. The precipitation reaction was carried out for 1 hour on the tube revolver at room temperature. For imaging, particles were washed once with 100 µL of Rinse buffer and then deposited onto an imaging well on a glass slide.

For total RNA experiments 500 ng of total RNA extracted from various different human tissue sources (colon, breast, and prostate) were used. The colon and breast tissue total RNA were purchased from BioChain, while the prostate tissue total RNA was purchased from Ambion. The total RNA was first heated to 95°C on a thermoshaker for 5 min and then cooled down over a period of 8 min before being added to the particles in hybridization buffer. Particles with a probe for cel-miR-54, a miRNA only found in C. elegans were used a negative control.

3.2.3 Imaging and Analysis

Imaging wells were created by attaching clear circular reinforcement labels (Avery) to a cleaned glass slide. The particles to be imaged were deposited inside the imaging well. Each well could hold 15 μL of volume and so the particles from each reaction typically filled two wells. The glass slide was inserted into the slide holder slot on the phone imaging stand as shown in the schematic in Figure 3-2B. A Samsung Galaxy S6 phone with a 4X macro lens attached (easymacro.com) was placed on top of the phone stand to photograph the particles. Images were taken on top of an orange rectangle (with RGB values 255,180,0) printed on white photo paper. In order to have a controlled lighting environment for imaging, adhesive LED lights (Chibitronics) were attached to the phone stand (powered by a cell battery and copper tape provided with the lights). To standardize ambient lighting conditions, the phone stand was used in a laminar flow cabinet with the overhead cabinet light

on (in a dark room, so that no other ambient light was present). The default camera application and settings were used.

The images were then cropped to exclude the imaging well in ImageJ (NIH) and then analyzed using a custom MATLAB script (see sample provided below). In the script, each image was separated into its RGB components. Both the blue and red channels were used to isolate particles using a fixed threshold as shown in Figure 3-2C (the blue channel worked best for low precipitate particles, while the red channel worked best at high precipitate levels). Particles were identified manually based on the shape, however this could be automated with existing shape detection algorithms. The script calculated the average red channel values for each particle along with the average background red value. Red channel values were inverted (255-value) and then normalized by the area of the control shape to account for the slight variation in project areas. Normalized net signal was calculated as background subtracted signal of the particle in question minus that of the control particle (0 nM biotin for reaction characterization, 0 fmol synthetic miRNA for calibration curves, or cel-miR-54 for total RNA). In cases where particles were touching each other and thresholding could not identify separate particles, average red channel values for particles were determined manually using ImageJ's polygon area selection tool.

The average net red channel signal was plotted against the biotin loading per particle on a semi-log scale and a line of best fit was fitted to the data using Origin Lab. The limit of detection (LOD) at each time point was determined as the biotin loading where the net signal is equal to 3 times the standard deviation of the control particles (3σ method). For total RNA data, a student's t-test was employed to determine whether the different between tumor and normal signal was significant.

A comparison of the signal from each of the RGB channels as well as grayscale is shown in Figure 3-1. Grayscale transformation from an RGB image in MATLAB obeys the following equation: $Grayscale = 0.2989R + 0.5870G + 0.1140B$ While net signal values are similar for red and green channels ($p>0.05$, student's t-test), the noise (standard deviation of the control particles) in the green channel results in a lower signal-to-noise ratio (SNR). The blue channel and grayscale net signals

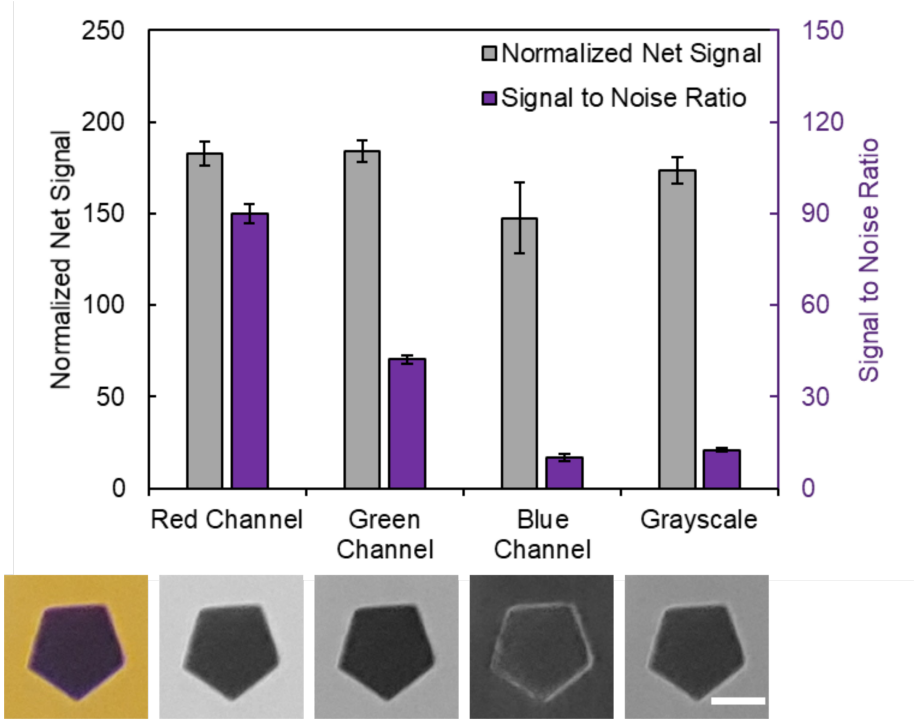

Figure 3-1: Normalized net signal from each individual color channel and grayscale transformation on the left axis. Corresponding signal-to-noise ratio on the right axis. Error bars represent 1 standard deviation. A representative particle image in each channel or after grayscale transformation is shown below each category. Scale bar is 200 µm.

are lower than red or green channels ($p<0.05$) and the noise is greater, resulting in a very low SNR. Thus, red channel signals result in the largest SNR, giving higher sensitivity compared to the other channels or a combination of all three.

3.3 Results and Discussion

3.3.1 Particle Fabrication and Imaging

Shape-encoded hydrogel particles were fabricated using SFL in PDMS microfluidic channels using previously published methods [73]. The photomask, as shown in Figure 3-2A determined the particle shape. The particles were made from a PEG-based prepolymer solution (20% polyethylene glycol diacrylate 700, 40% polyethylene glycol 600, 5% Darocur 1173 photoinitiator, and 35% 3x Tris-EDTA buffer) and copolymerized with DNA capture probes containing an acrylate group [106].

Particle imaging was carried out with a Samsung Galaxy S6 with a 4X macro lens

attached (easy-macro.com). The phone was placed on a custom-made 3D printed holder, which contained a slide holder for the samples as seen in Figure 3-2 (A sample CAD file is provided here). Photos were taken with the stock camera application with orange paper underneath the phone holder. The orange color is complementary to the indigo color of the precipitate and increases the contrast for colorless particles (which would not be visible on a white background). Thus, particles with precipitate were visible in the red channel upon RGB decomposition (where the orange background is nearly white) and particles that were colorless were visible in the blue channel (where the orange background is nearly black) as seen in Figure 3-2. Both red and blue channels were used to detect particles using thresholding. Of the three channels, as well as a combination of the three (grayscale), the red channel showed the largest signal to noise ratio as seen in Figure 3-1. Hence, the red channel was used for signal quantification, using a custom MATLAB script.

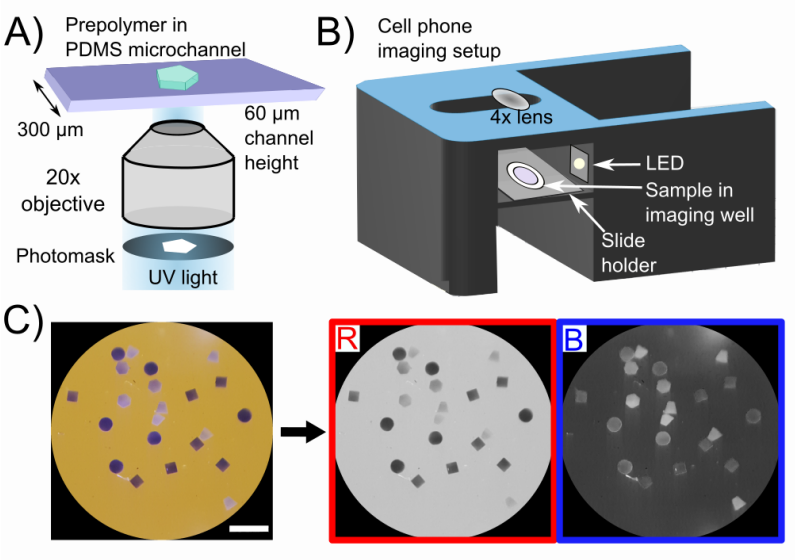

Figure 3-2: A) Fabrication of shape-encoded hydrogel particles using stop-flow lithography. Shape is defined using a photomask. B) Imaging setup consisting of a 3D-printed phone stand with a built-in slide holder. C) Representative image taken of particles after reaction using the phone setup. Scale bar is 1 mm. Imaging on an orange background allows for a near-white background in the red channel (used for analysis) and near-black background in the blue channel (allowing easy identification of all particles).

3.3.2 Precipitation Reaction Characterization within Hydrogel Particles

In order to characterize the precipitation reaction independent of target capture and labelling, we fabricated hydrogel particles with different concentrations of a short DNA probe containing a biotin moiety as shown in Figure 3-3A. These particles were conjugated to 10 µg/ml S-AP over a course of 30 minutes and then mixed with NBT-BCIP substrate for 15, 30, 60 or 90 minutes. After the set reaction time, the particles were deposited inside an imaging well for imaging with a cell phone. The average net red channel signal as a function of biotin probe concentration is shown in Figure 3-3B. The probe concentration is based on the particle volume and it represents how much biotin and consequently enzyme is incorporated into each particle. Hence, the LOD is a measure of the minimum amount of enzyme necessary to produce a detectable signal in a given amount of time. The LOD generally increases with time but there is little improvement after 60 minutes of reaction, where the LOD reaches 6.8 nM. This corresponds to a biotin loading of 20 amol biotin/particle. The net signals start saturating at the highest biotin concentrations tested after 60 minutes as evidenced in the both the plot and photos shown in Figure 3-3B.

Increasing the substrate concentration up-to 5-fold results in this saturation occurring at lower concentrations as shown in Figure 3-4. This leads to higher signal for particles with concentrations from 6 – 15 nM biotin, accompanied with a slight improvement in the LOD (5.3 nM). Based on these reaction characterization experiments a reaction time of 60 minutes using 5x substrate was used for the colorimetric detection of miRNA.

It should be noted that the particles with different biotin concentrations were all in the same tube during enzyme conjugation and reaction (Figure 3-3A), but maintain distinct shades and hence have minimal cross-talk. After 60 minutes, the reaction solution starts turning blue. We hypothesize that at this point the high concentration biotin particles have reached a saturation limit for how much precipitate they can hold but the enzymes conjugated within keep generating more precipitate, which

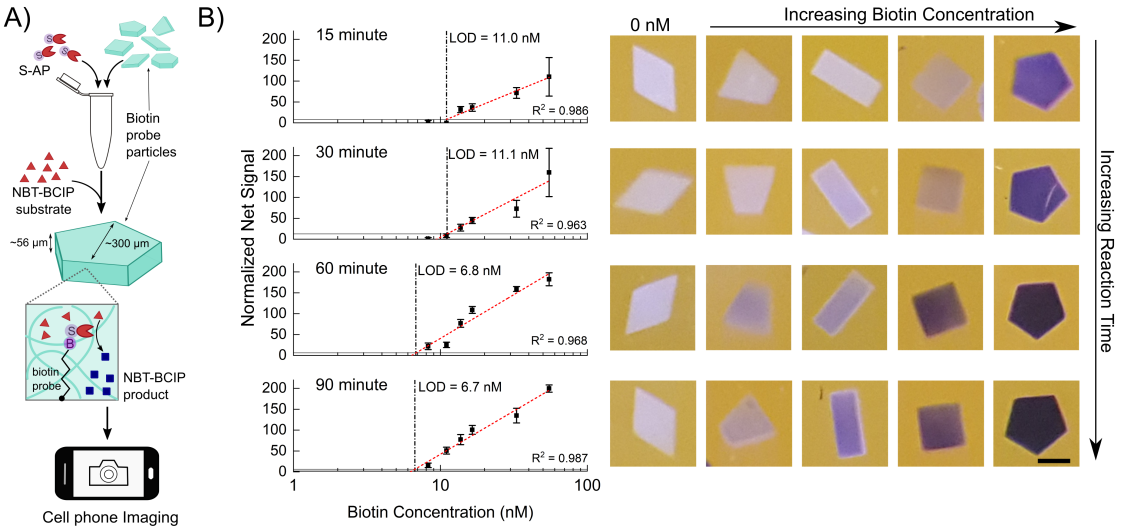

Figure 3-3: A) Workflow of the reaction characterization experiments. Particles with different biotin concentrations are conjugated to S-AP in solution, to which NBT-BCIP substrate is added. The enzymatic reaction within the hydrogels produces the blue precipitate product. Particles are then imaged with a cell phone. B) Normalized net signal as a function of biotin probe concentration at after a reaction time of 15 minutes, 30 minutes, 60 minutes and 90 minutes. Vertical dashed lines show the limit of detection. Horizontal lines show the 3σ level. Error bars represent 1 standard deviation. R^2 values represent Pearson correlation coefficients. Representative particle images are to the right of each graph. Scale bar is 200 µm.

then seeps out of the hydrogel network and enters the solution phase. Yet the control particles stay free of precipitate even after 90 minutes of reaction, when there is free blue reaction product in the solution. This indicates that the precipitate stays considerably localized during the course of reaction and that the precipitate does not simply adsorb onto the particle from solution but must be generated within the particle to stay. Previous reports have shown that the NBT diformazan is more efficiently immobilized in porous 3D structures such as that of hydrogels [71, 84]. Moreover, there is some evidence that hydrophobic small molecules preferentially partition into the hydrogel matrix [107]. Thus a combination of in-situ precipitate generation and the relatively hydrophobic environment of the gel both result in the precipitate localization and build-up.

3.3.3 microRNA Detection

For miRNA detection, particles were co-polymerized with oligonucleotide DNA probes specific to different miRNA [45]. The shape of the particle encoded for the miRNA

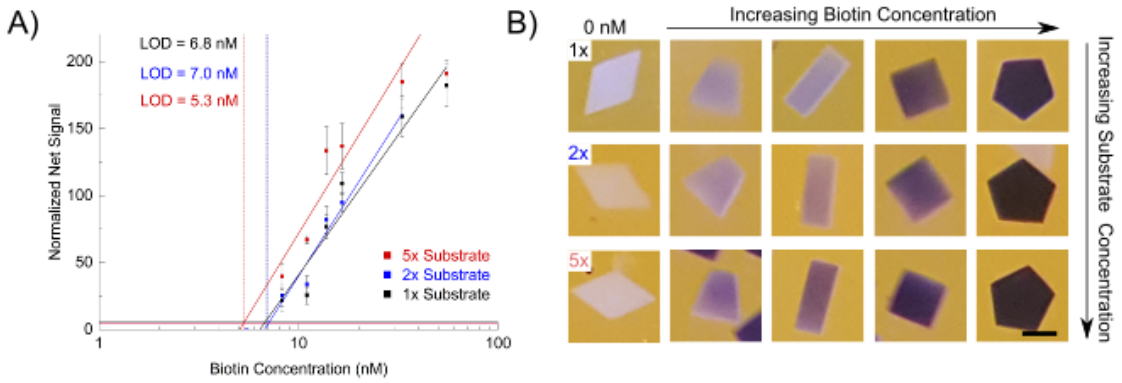

Figure 3-4: A) Normalized net signal as a function of biotin probe concentration using 1x, 2x, and 5x concentrated NBT-BCIP substrate solution. Reaction time was 60 minutes for all three. Vertical dashed lines show the limit of detection. Horizontal lines show the 3σ level. Error bars represent 1 standard deviation. Pearson's correlation coefficients for the semi-log fits are 0.968, 0.983, and 0.944 for 1x, 2x, and 5x respectively. B) Representative particle images at various biotin concentrations for each substrate concentration tested. Scale bar is 200 µm.

target. Target hybridization was conducted for 90 min at 55°C followed by 30 min of ligation of a universal biotinylated adapter using T4 DNA ligase as shown in Figure 3-5A. Hybridization and ligation times were optimized in our prior study.19 After ligation, the same steps as with a biotinylated probe were followed. The particles were conjugated with 10 µg/ml of S-AP enzyme for 30 minutes and then reacted with 5x NBT-BCIP substrate for 60 min after which, the particles were deposited inside an imaging well for imaging with a cell phone. Between each step shown in Figure 3A, the particles are washed by centrifugation three times to remove unbound target and reagents. For each wash, the particles are centrifuged for 20 s and the supernatant is removed and replaced with fresh buffer as detailed in the Experimental section.

Calibration curves for 3 different miRNA are shown in Figure 3-5B, in which the LODs are 0.22 fmol for miR-21, 0.42 fmol for miR-221, and 1.2 fmol for miR-141. This corresponds to 4.5 pM, 8.4 pM and 23.7 pM respectively based on the 50 µL hybridization volume. LODs were calculated using the 3σ method as was done with the biotin probe particles. Net signal increases linearly with miRNA total amounts. The higher signals with miR-21 could be attributed to the higher probe concentration used for miR-21. Previous work has shown that miR-21 target has a slower binding rate at short times leading to higher probe concentrations being used in the particle

[45]. Higher probe concentration, resulting in more negative charge in the hydrogel, could also be beneficial to the precipitation reaction.

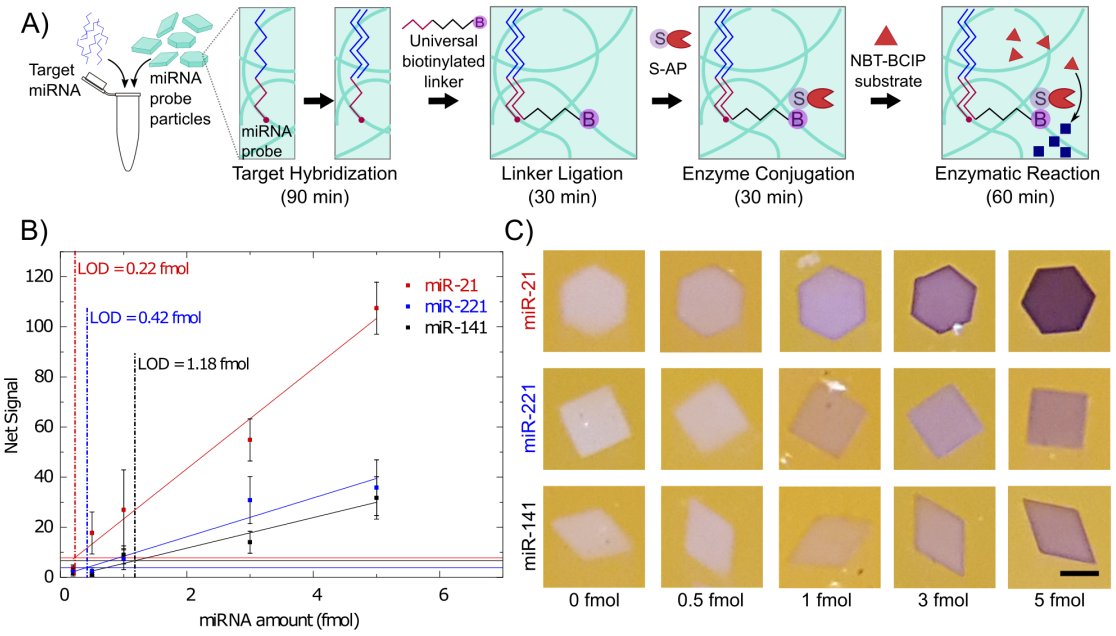

Figure 3-5: A) Schematic of miRNA hybridization assay. Particles are co-polymerized with an acrylated probe specific to a miRNA target. Each shape is specific to a different target. The target binds to the probe and then a universal biotinylated linker is ligated to the target. S-AP binds with the biotin and catalyzes the reaction converting NBT and BCIP to an insoluble NBT diformazan. B) Calibration curves of 3 different miRNA. Reaction time was 1 hour. Vertical dashed lines show the limit of detection. Horizontal lines show the 3σ level. Error bars represent 1 standard deviation. Pearson correlation coefficients for the linear fits are 0.99, 0.968, and 0.969 for miR-21, miR-221, and miR-141 respectively. C) Representative images of particles after 1 hour of reaction for each miRNA. Scale bar is 200 µm.

We hypothesize that the key source of variability in this detection scheme comes from the ability to ensure the particles are being well mixed in solution. The large size of these particles makes them prone to settling and sticking to the reaction tube even with continuous mixing. Improvements to the mixing protocol should result in reduced variability. As was demonstrated with the biotin probe experiments, there is a saturation limit on how much NBT precipitate can be contained within the hydrogels, limiting the dynamic range of this bioassay. However, we believe that this saturation limit should not be a concern due to the focus on analytes of low concentration. Moreover, for multiplexed experiments, the capture probe concentrations can be adjusted to account for large variances in analyte concentrations. While there exist solution-based colorimetric assays with higher sensitivity (by using nu-

cleic acid amplification), they cannot perform multiplexing [51, 90–93]. Moreover, it is possible to increase the sensitivity of this platform by combining it with upstream nucleic acid amplification, which is compatible with hydrogels, such as rolling circle amplification or hybridization chain reaction [55, 76]. These amplification schemes result in more biotin labels per target bound, resulting in more enzyme reporter labelling within the hydrogel particle.

Based on previous work with fluorescent reporters, the signal increases with decreasing overall hydrogel volume and with increasing ratio of surface area to 2D projected imaging area [62, 66, 105]. Thus, it should be possible to increase signal similarly in the colorimetric assay by manipulating these variables. For example, decreasing overall particle size (whilst staying within the imaging resolution of a cell phone), or hollowing out the particles to create a frame-like structure should concentrate the target into a smaller volume and increase the flux of target into the hydrogels [62]. It is interesting to note that a boundary layer (dark edge) is visible on the particles after reaction as shown in the images in Figure 3-5C. In fluorescence-based assays, a boundary layer is often visible and is indicative of a high Damköhler number (Da»1), where the reaction (hybridization in this case) is much faster than diffusion of target into the hydrogel [62, 66]. Figure 3-6 shows that the profile of this boundary layer is similar to that visible by direct fluorescent labelling, highlighting how well the NBT precipitate stays localized even within the particle.

To assess whether precipitation-based colorimetric detection could measure miRNA from complex samples containing a variety of other nucleic acids and other contaminants, miR-21 was detected from 500 ng total RNA extracted from 3 different types of healthy tissue: prostate, breast, and colon. As a negative control, particles with a probe for cel-miR-54, a miRNA only found in C. elegans, were also added for net signal calculations. All three tissues had similar miR-21 signal as shown in Figure 3-7. miR-21 is a known oncogenic miRNA upregulated in cancers [8, 22, 108]. Since the tissue samples were all healthy tissue, it follows that only baseline levels of miR-21 were present, and hence similar levels were found in all three tissues.

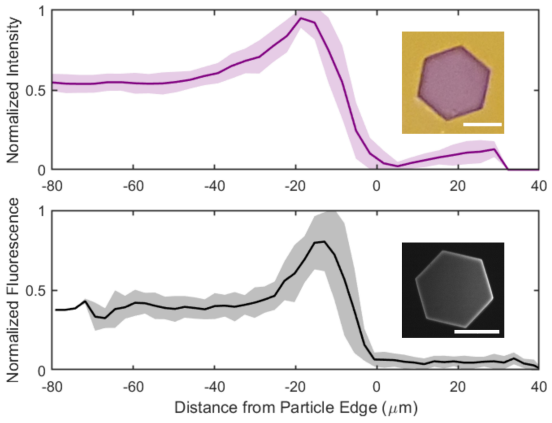

Figure 3-6: Top: Normalized red channel intensity for the particle shown (3 fmol miR-21, 1 hr reaction with 5x NBT-BCIP substrate) as a function of distance from particle edge. Bottom: Normalized fluorescence values for the particle shown (500 amol miR-21, labelled with streptavidin-phycoerythrin) as a function of the distance from the particle edge. In both cases, 20 intensity line scans around the particle boundary were averaged. Shaded regions represent 1 standard deviation. Scale bars are 200 µm.

3.3.4 Multiplexed microRNA Detection from Total RNA

When considering miRNA dysregulation patterns, a small panel of miRNA has better diagnostic value than individual miRNA, and hence multiplexed measurements from a single sample are especially important for miRNA detection [3, 70, 83]. Each particle shape encodes for a different miRNA probe, allowing for multiplexed measurements from the same sample. All the particles using for multiplexed miRNA detection have a similar surface area to volume ratio (coefficient of variation of 5.2%) for comparable target and enzyme diffusion.

In order to assess whether miRNA dysregulation patterns could be determined with this colorimetric platform, a multiplex miRNA detection assay was performed with total RNA extracted from colon tumor tissue and normal adjacent tissue. Again, particles specific to cel-miR-54 were added to each sample as a negative control. As seen in Figure 3-8A, high miR-21 concentrations were found in tumor total RNA. miR-21 is an oncogenic miRNA found to be upregulated in multiple different cancers and diseases including colon cancer tissue, and this is reflected in the data from colorimetric measurements as well as the clearly discernable purple hexagon particle in Figure 3-8B [8, 22, 109, 110]. In contrast, similar amounts of miR-16 were found in both tumor and normal total RNA. Previous reports have shown that in colon

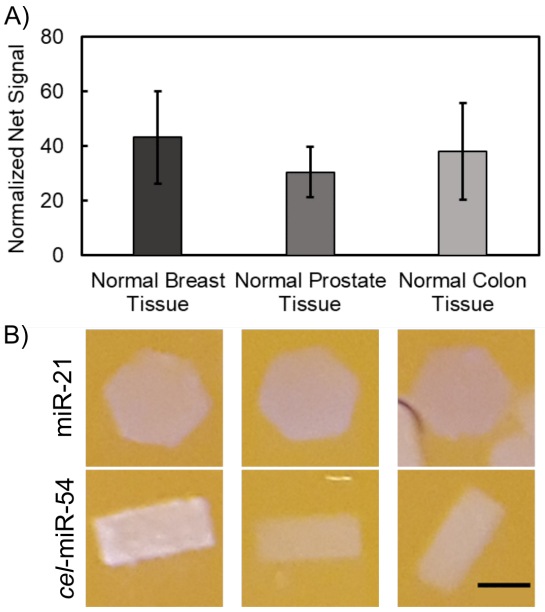

Figure 3-7: A) Net signal from miR-21 particles from 500 ng total RNA extracted from three different types of tissue. Negative control particles for cel-miR-54 were used for normalization. Error bars represent one standard deviation. No significant differences based on pair-wise comparisons using student's t-test ($p>0.05$). B) Representative image of particles after 1 hour of reaction. Scale bar is 200 µm.

cancer specifically, miR-16 has fairly stable, high expression levels and has hence been used as an endogenous standard in miRNA analysis of colon cancer [8, 110]. Upregulation of miR-141 has shown to be associated with poor prognosis in advanced colon cancer [111]. While miR-141 levels in this specific patient's tissue were found to be similar in both tumor and normal tissue, their low abundance, close to the limit of detection, prevents a true comparison.

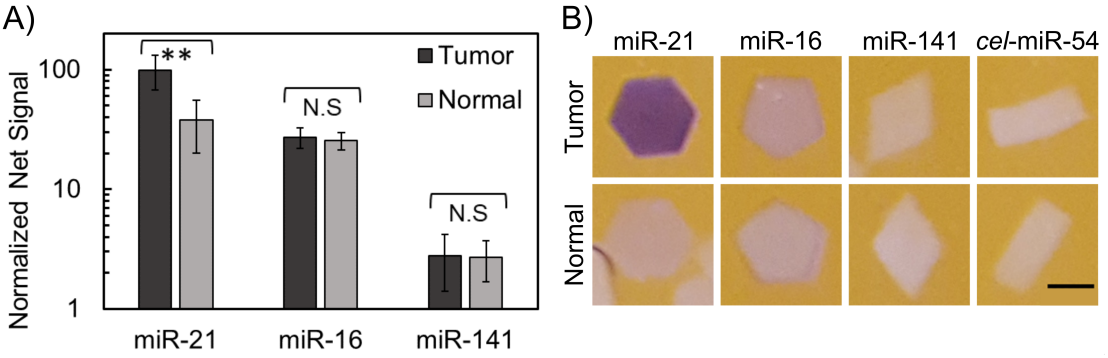

Figure 3-8: A) Normalized net signal of 3 different miRNA from 500 ng total RNA extracted from colon tumor tissue and colon normal adjacent tissue. Particles containing probe for cel-miR-54 were used as a negative control. ** = $p<0.001$. Error bars represent 1 standard deviation. B) Representative images of particles after multiplexed detection from colon total RNA. Scale bars are 500 µm.

Scaling Analysis for Substrate Depletion during Multiplexed miRNA Detection

For multiplexed miRNA detection (3-5 miRNA panel), we assume there is at most 10 fmol of target miRNA. Based on previous work in the Doyle group, we expect 50% of the miRNA hybridize within 90 minutes [105], thus giving about 5 fmol of S-AP enzyme bound in the reaction. Given the enzymatic activity (517 units/mg) and molecular weight (195 kDa) of S-AP, this results in 5 x 10-4 units in the reaction. One unit of S-AP hydrolyzes 1 µmol of p-nitrophenyl phosphate per minute at 23°C, pH 10.4 [112]. We assume a similar activity rate for NBT/BCIP in our reaction buffer. Therefore, over the course of a 60-minute reaction, the bound enzyme could convert at most 0.03 µmol of substrate. At 5x substrate concentration (2 mM NBT/BCIP), there is 0.1 µmol substrate present. Given these upper bounds on the enzymatic activity possible, we believe that in the time frame of the reaction, substrate depletion should be minimal.

3.4 Conclusions

In conclusion, we developed and characterized a precipitation-based colorimetric detection system that can be measured using a simple cell phone camera. This system combines the superior advantages offered by non-fouling, biocompatible hydrogel particles as a substrate for biomolecule detection assays with a facile and robust enzymatic, colorimetric precipitation reaction. The hydrogels act as both the reactor vessel and concentrator, leading to sensitive target detection. The indigo-purple NBT precipitate stays localized exceptionally well within the particles, even outlining the formation of a boundary layer at high target concentrations. The shape-encoded particles were fabricated using stop-flow lithography, enabling multiplexing even in complex samples, while preserving the superior kinetics of solution assays. As a result, multiplexed, colorimetric detection of miRNA was possible down to sub-femtomole amounts using a simple phone camera setup. Finally, this detection system is compatible with upstream nucleic acid amplification to improve sensitivity

and is applicable to many other biomolecules of interest such as protein and cytokine detection. The precipitation reaction within the hydrogel is independent of the type of target and only requires the ability to conjugate the enzyme alkaline phosphatase to the location of the target. We hope that the low-cost and ease of this cell-phone compatible, multiplexed, colorimetric detection system helps in translation of this platform to low resource settings where multiplexed measurements are ideal but fluorescence measurements are not possible.

Signal Amplification Strategies for microRNA Detection

In this chapter we present two different amplification techniques, precipitation-based enzymatic amplification and strand displacement amplification in hydrogels. We also discuss limitations, and possibilities for further progress.

4.1 Introduction

MicroRNA (miRNA) are small, non-coding RNAs that are an emerging class of biomarkers that have been shown to be dysregulated in many diseases including cancers, cardiac diseases, and cognitive disorders [8, 22]. miRNA regulate mRNA translation through either blocking the translation or degrading the target mRNA after binding to the 3' untranslated region [15, 16]. miRNAs have exceptional stability in blood in body fluids due to their association with proteins just as Argonaute, and packaging within extracellular vesicles (EVs), protecting them from RNasesM [14, 18, 19]. miRNA can be shuttled to other cells via EVs, RNA-binding proteins such as argonaute, and even certain classes of lipoproteins [20, 21]. This cell-to-cell transfer of miRNA has been implicated in tumor metastasis, tumor proliferation, and even drug resistance [16, 17]. As such miRNA are found in the blood and other body fluids and are a potent source of information since their miRNA dysregulation profiles can reflect state of diseases and tumors [16, 22].

However, miRNA only represent a small fraction (0.01%) of total RNA and accordingly, their concentration in bodily fluids is low and highly variable depending on the miRNA, disease, and person [46]. As such, some form of amplification becomes necessary to be able to detect miRNA at relevant physiological concentrations in serum and plasma, particularly for clinical and diagnostic end uses. Conventional strategies for amplified miRNA detection, include reverse-transcription qPCR (RT-qPCR), which is limited in multiplexing and involves complex multistep procedures [43, 44]. Moreover, quantitative detection with these traditional approaches is very difficult and seldom demonstrated in literature [44, 45]. Their small size (∼20-25 ribonucleotides) and variable GC content results in a large variance in melting temperatures (T_m) for annealing during PCR reactions, introducing sequence specific biases [46]. Couple with that, their high sequence homology and highly variable expression levels have made accurate detection and quantification difficult [44, 45, 47].

Specifically looking at extracellular vesicle-derived miRNA (EV-miRNA), concentrations vary over many orders of magnitude depending on the EV source and miRNA species. For example, a pancreatic cancer cell line was reported to have 14 miRNA copies per EV, while healthy plasma could have as low as 2×10^{-5} miRNA copies per EV [113, 114]. In order to measure miRNA at low copy numbers, signal amplification will be necessary. Amplification can be achieved through nucleic-acid based approaches and enzymatic approaches, while detection is typically achieved through optical, plasmonic or electrochemical methods [43].

Within optical-based miRNA detection, there exist many amplification schemes, however many are solution-based reactions and hence are limited by their spectral multiplexing ability [43, 48]. In contrast, hydrogel-bound miRNA capture and amplification reactions enable scalable multiplexed detection, through spatial or graphical encoding [45, 79]. Hydrogels are a versatile platform for biomolecule detection assays due to their biocompatibility, solution-like kinetics, non-fouling nature, and ability to incorporate capture agents inside a 3D network [67]. Previous work in the Doyle group has demonstrated multiplexed, unamplified miRNA detection using hydrogel

microparticles from a variety of sources such as cell lysate, FFPE tissue and total RNA extracts down to single attomole sensitivity [45, 67, 115]

Previous work on amplified miRNA detection within hydrogel particles were either based on nucleic acid amplification techniques such as rolling circle amplification (RCA) and hybridization chain reaction (HCR), or enzymatic signal amplification [70, 76, 77, 116]. RCA has been used in the Doyle group to detect miRNA with a limits of detection (LOD) ranging from 2.1 zmol -44 zmol (42 aM - 0.88 fM in 50 μL reactions used) [76]). However the protocol is long and arduous, requiring stringent buffer composition control. Recently, HCR has been successfully demonstrated in hydrogel particles, however the improvements in LOD are about 1 order of magnitude for the particular miRNA detection, and still above 1 amol LOD (20 fM) [116].

Enzymatic amplification using streptavidin-β-galactosidase (SAB) has also been successfully used in the Doyle group to reduce the miRNA LOD to 0.1 amol. (2 fM in 50 μL) This enzymatic amplification scheme converts a non-fluorescent substrate FDG (fluorescein di-β-D-galactopyranoside) into a fluorescent product [70, 77]. This particular enzyme and another substrate RBG (resorufin-β-galactopyranoside) is being used by the commercialized single-molecule array (Simoa) technology, reaching LODs of 1-30 fM for miRNAs [49, 60]. Both fluorescent products are water soluble, and thus a rapid oil isolation step is crucial for the signal to remain associated with that particular bead or particle [49, 77, 117, 118]. Moreover, the amplification is limited to the amount of substrate stored in the oil droplet, ultimately limiting the maximum amplification possible.

An overview of these amplification techniques is provided in table 4.1. To avoid and improve upon the weaknesses and difficulties associated with prior amplification strategies, we pursued 2 different amplification techniques, the first being an enzymatic signal amplification using a novel precipitating substrate and the second being strand displacement amplification (SDA) adapted from solution-based molecular beacon assays.

Table 4.1: Advantages and disadvantages of various amplification techniques for miRNA detection, focusing on optical detection methods.

Technique	**Advantages**	**Disadvantages**	**Ref.**
Rolling Circle amplification (RCA)	amplification continues as long as reactants and reporter probes are present	complex workflow; sensitive to reaction conditions	[52, 76]
Hybridization Chain Reaction (HCR)	amplification continues as long as reactants and reporter probes are present	complex workflow; steric hindrance from long chain could truncate reaction; sensitive to reaction conditions	[**Guo2017HybridizationMicroRNA** 51, 55, 116]
streptavidin-β-galactosidase (SAB) and FDG or RBG substrates	rapid fluorescent signal development	non-specific binding of enzyme leads to high background signal; soluble fluorescent product needs to be isolated to build signal	[70, 77, 117, 118]

4.2 ELF-97 Fluorescent Precipitation-based Enzymatic Amplification

Hydrogel-based detection assays typically label the captured target using a fluorescent reporter for signal readout. Taking a lesson from traditional immunohistochemical labelling techniques, the fluorescent reporter can be replaced with an enzyme capable of generating a fluorescent signal. Hydrogels have been shown to be capable with numerous different enzyme-substrate systems in which each target labelling event results in multiple reporters generated by the enzyme. However, the majority of systems using enzymatic amplification within hydrogels generated a fluorescent product that is soluble and thus must be contained for sufficient signal generation and multiplexing. Previous techniques have used oil isolation to contain the fluorescent product close to the hydrogel structures [49, 70, 77, 117, 118]. Thus, a limited amount of substrate is accessible for the reaction.

The Enzyme Labeled Fluorescence (ELF-97) technology developed by Molecular Probes circumvents the requirement for oil isolation. It is a proprietary small molecule that is soluble as a substrate, but upon cleavage of the phosphate group, it becomes insoluble in aqueous solutions and exhibits a large (>100 nm) stokes shift in fluorescence output. Phosphate cleavage is mediated by the enzyme alkaline phosphatase, commonly used with chromogenic products for western blots. The product forms an insoluble precipitate that stays localized [119, 120]. This technology has been tested with mRNA in-situ hybridization in cells, tissue sections as well as for immunocytochemistry staining [119, 120].

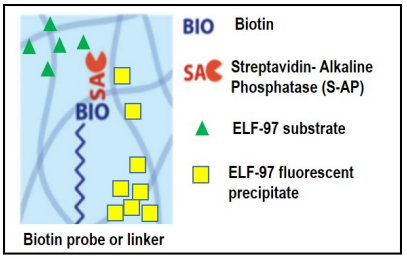

Figure 4-1: Schematic for ELF-97 based enzyme amplification. Streptavidin alkaline phosphatase binds to a biotin probe, which is covalently attached to the hydrogel or is part of the biotintylated linker. The ELF-97 substrate is converted to a fluorescent precipitate, which stays localized close to the enzyme.

This enzyme-substrate pair was explored for use in our hydrogel based miRNA assays in which the fluorescent product would precipitate inside the hydrogel and stay localized. No oil isolation would be necessary, and moreover, it would be possible to keep increasing the fluorescent signal by introducing more substrate. A schematic of how this could work in the hydrogels is shown in Figure 4-1. As the hydrogel is replenished with the ELF-97 substrate, the enzyme keeps generating product, which falls out of solution within the hydrogel. Since this enzyme is conjugated to streptavidin, it can be attached to the universal biotin linker in miRNA assays, or to a biotinylated DNA probe that is directly polymerized into the hydrogel.

4.2.1 Experimental

Glass microchannels were prepared as described in Chapter 2. Hydrogel posts with a biotinylated DNA probe at varying concentrations were polymerized into the channel

using projection lithography as described in Chapter 2. The ELF-97 mRNA in-situ hybridization kit (Molecular Probes, E6604) along with streptavidin alkaline phosphatase (S-AP, Invitrogen) were used for all studies.

A syringe pump attached to a pipette tip filled with fluid inserted into the inlet of the microchannel was used to drive flow into the channel. Pump speed was set to 5 μL/min. An empty pipette tip was inserted into the outlet to collect the outflow. Unless otherwise indicated, all steps were performed at room temperature. Each microchannel had 100 μm posts with biotin probe and blank control posts. The posts were first blocked with blocking buffer (component B) for 30 minutes before introducing S-AP enzyme (10μg/ml in blocking buffer) into the channels for binding with the biotin probes for 30 minutes. The channel was washed with 1x wash buffer (component A) for 1 hour to let any trapped enzymes diffuse out. The channel was then equilibriated with developing buffer (component C) for 5 minutes before introducing the substrate solution consisting of 0.5 mM ELF-97 substrate (component D) and 1:100 dilutions of additives 1 and 2 (components E and F) in developing buffer. This substrate solution was made fresh before each experiment and filtered with a 0.45 μm small volume filter before use. After the predetermined time for reaction, the channel was flushed with washer buffer rapidly with a pipette to stop the reaction. Posts were imaged with fluorescence microscopy using a UV long pass filter (ex:350/50, em: 420LP, Chroma).

For time series studies, at each time point, the channel was flushed with wash buffer, imaged, and then substrate solution was re-introduced into the same channel to continue the reaction. For comparison with SAPE labelling, biotin and control posts were labelled with a SAPE solution (20μg/ml in TET) for the same time frame as the corresponding precipitation reaction and then washed with TET before imaging with fluorescence filter set appropriate for SAPE (Omega XF101-2).

4.2.2 Results and Discussion

The compatibility of the ELF-97 substrate with hydrogels was established with experiments with hydrogel posts within glass channels so that substrate flow and reac-

tion could be monitored continuously. Hydrogel posts with a biotin probe were polymerized in a silanized and oxidized glass channel following established protocols[66, 70]. The hydrogel posts have the same composition as the particles. The kinetics of the precipitation reaction were assess using a time series study in which the ELF-97 substrate solution was introduced into the channel containing biotinylated (and control) posts labelled with S-AP at 1µL/min (Pe=3.3×10^4) for a specified time. Flow was stopped and the channel was flushed with wash buffer before imaging. Substrate flow was then reintroduced to continue the precipitation reaction and build the fluorescence signal from the precipitate. At Pe»1, the substrate concentration around the posts should be uniform over time, and hence no depletion zones should form around the posts. The time course for signal development is show in Figure 4-2. A parallel channel of posts were labelled with SAPE for comparison. Control posts (no biotin probe) were polymerized within the same channel and exhibited minimal non-specific fluorescence. Net signal calculations subtracted the average control signal at each time point.

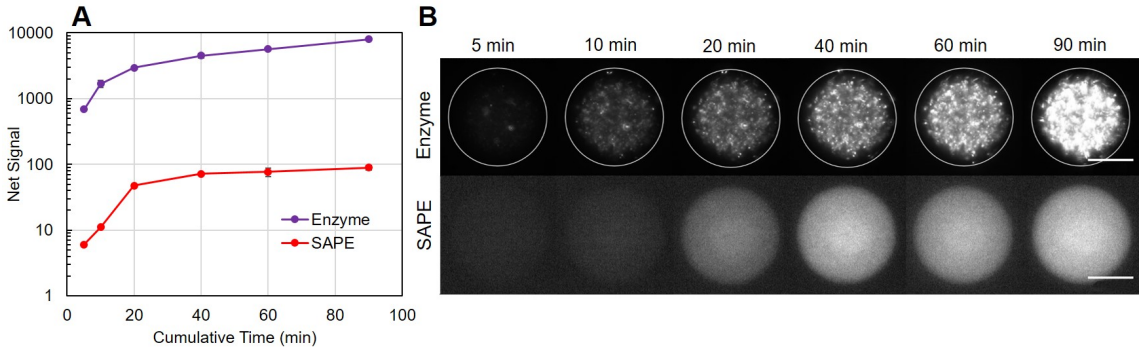

Figure 4-2: Fluorescent signal growth over time for ELF-97 enzyme amplification. A) Net fluorescent signal over time for both SAPE and ELF-97 precipitate (Enzyme). Cumulative time represents the total time under ELF-97 substrate/SAPE flow. The net signal is the background subtracted signal minus the negative control signal (non-biotintylated posts). Error bars represent one standard deviation. 8 posts were analyzed for each time point. B) Representative fluorescence images of the posts under ELF-97 (top) and SAPE (bottom) flow. The same post is shown at each time point. All enzyme images are presented at the same brightness and contrast. All SAPE images are presented at the same brightness and contrast. White outline indicates the post boundary. Scale bars are 50 µm.

The fluorescent product stayed localized within the hydrogel posts and the signal could be increased by continuing the flow of substrate. The signal was almost 100x higher than direct labelling with SAPE. These initial time series experiments were

done at high biotin concentrations of 100 nM biotin probe in the prepolymer solution, resulting in ∼11 nM incorporation into the hydrogel [105]. Given the size of each post, it is estimated that each post had 4 amol biotin. To test the ability of this method to work with low concentrations, a calibration curve study was conducted in which different concentrations of biotin probe in the hydrogel prepolymer were polymerized as shown in Figure 4-3. In a parallel channel, SAPE labelling of the biotin probes was conducted as a comparison. Images were taken after washing the channels three times after 60 minutes under substrate/SAPE flow. 60 minutes was sufficient time for precipitate to be visible (without contrast adjustment) in the 5 nM posts.

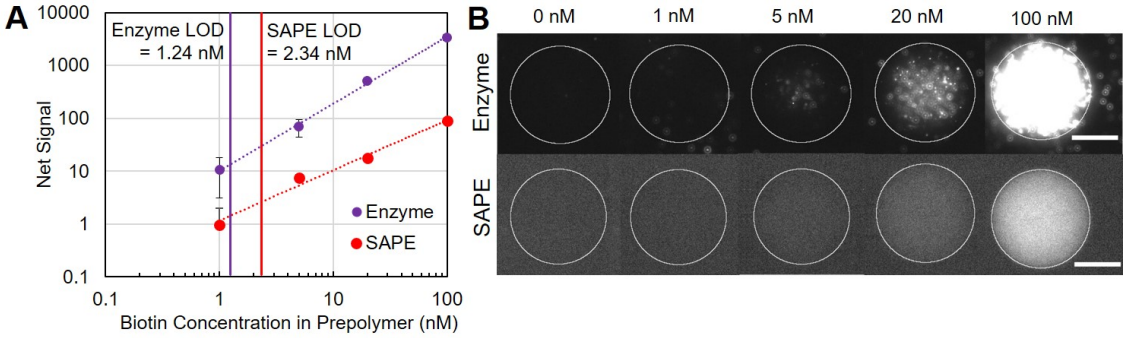

Figure 4-3: Biotintylated post calibration curve with ELF-97 enzyme amplification. A) Net fluorescence signal from SAPE and ELF-97 precipitate after enzyme amplification at different biotin concentrations. The net signal is the background subtracted signal minus the negative control signal (0 nM). The LODs of 1.24 nM for enzyme and 2.34 nM for SAPE were determined as the biotin concentration with a signal that was 3 times the negative control's standard deviation. Error bars represent one standard deviation. 6 posts were analyzed for each concentration. B) Representative fluorescence images of the posts under ELF-97 (top) and SAPE (bottom) flow. All enzyme images are presented at the same brightness and contrast. All SAPE images are presented at the same brightness and contrast. White outline indicates the post boundary. Scale bars are 50 µm.

The LOD using enzymatic amplification was 1.24 nM, a slight improvement compared to SAPE with a LOD of 2.34 nM. However, the higher background and higher slope mean that the significant difference in signal at higher concentrations was not reflected at lower concentrations.

Attempts to improve the conditions for precipitation by increasing temperature or substrate concentration did not result in improvement to the LOD. A second set of time series experiments were conducted in which the posts (100 nM and 20 nM biotin) were imaged during the substrate flow and subsequent washing. At high

biotin concentration, there was only a slight decrease in signal during washing. At low concentrations (20 nM biotin in the prepolymer solution), the product that was present in the posts washed out quickly, resulting in rapid loss of signal. Thus it was hypothesized that the minimum concentration threshold to trigger precipitation out of solution had not been reached and hence why the amplification factor at low biotin concentrations was small. Finally, proof of concept experiments with hydrogel particles were also conducted. Microparticles have better reproducibility and can be mass produced with stop flow lithography. Hydrogel microparticles can also be spatially encoded for different miRNA probes allowing for multiplexing [73, 74]. Particles with a biotin probe were labelled with S-AP in solution and then parked inside parking channels, where substrate flow was introduced. While the precipitate could stay isolated within the particles, the LOD was worse than with hydrogel posts, and did not show any improvement vs. SAPE labelling. Figure shows the results of these times series experiments during washing, as well as proof-of-concept experiments with hydrogel particles.

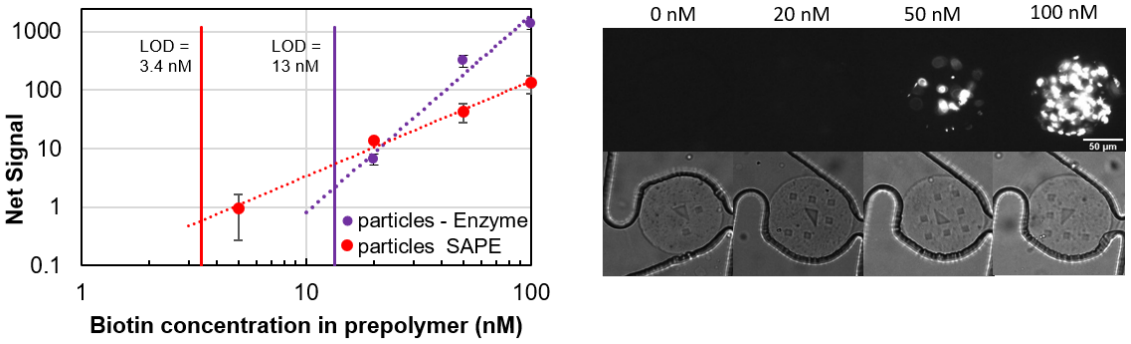

Figure 4-4: Average net signal from SAPE and ELF-97 precipitate after enzyme amplification within hydrogel particles at different biotin concentrations. The LODs of 13 nM for enzyme and 3.4 nM for SAPE were determined as the biotin concentration with a signal that was 3 times the negative control's standard deviation. Error bars represent one standard deviation. Representative fluorescence images of the parked particles after substrate flow with the corresponding brightfield images. Scale bars are 50 µm.

4.3 Hairpin Strand Displacement Amplification

In this work, we leveraged the benefits of hydrogel microparticles for miRNA target-triggered strand displacement amplification (SDA). This amplification scheme makes

use of a hairpin capture probe, resulting in specific target binding and rapid target recycling. This process results in signal amplification, while maintaining the many benefits of hydrogel microparticles, including graphically encoded multiplexing. This amplification scheme was chosen due to the ease with which a probe design could be incorporated within hydrogel particles, the universality of the primer design, and compatibility with upstream lysis protocols by having a separate miRNA capture and amplification step. Of the numerous versions of strand displacement amplification explored (including versions with a nicking enzyme and polymerase), the hairpin approach showed the most promising preliminary results.

SDA relies on the opening of a hairpin probe upon hybridization to the target. The opening allows a biotin primer to bind, which is then extended by a strand displacing polymerase. The displaced strand, the target, is allowed to bind to another hairpin probe. Thus, the target recycling enables rapid isothermal amplification. This is based on the molecular beacon assays in solution used for DNA and RNA amplification, in which a hairpin probe with a fluorophore and quencher is opened by the target, separating the fluorophore and quencher and producing a signal. A primer is allowed to bind and is extended by a polymerase in order to for the target to be recycled [58, 121–123].

SDA was adapted to hydrogel particles by copolymerizing an acrylated DNA hairpin probe specific to a target miRNA. The hairpin capture probe hybridized with the miRNA target, causing the hairpin to open as shown in the schematic in Figure 4-5. This allowed for a small biotinylated primer to bind to the top of the now-open probe. DNA polymerase extended the primer and displaced the bound target, allowing it to be recycled and open another hairpin probe. The biotinylated product strand was then labelled with streptavidin-phycoerythrin (SA-PE) for fluorescent imaging of the encoded particles.

The probe design was optimized through solution-based assays in a qPCR (Applied Biosystems 3500) in which a molecular beacon probe was tested with various primer lengths and primer binding locations for the amplification of let-7a. Particle-based assays were used for further optimization of probe-primer performance. Different

polymerases were also assessed using a solution-based assay.

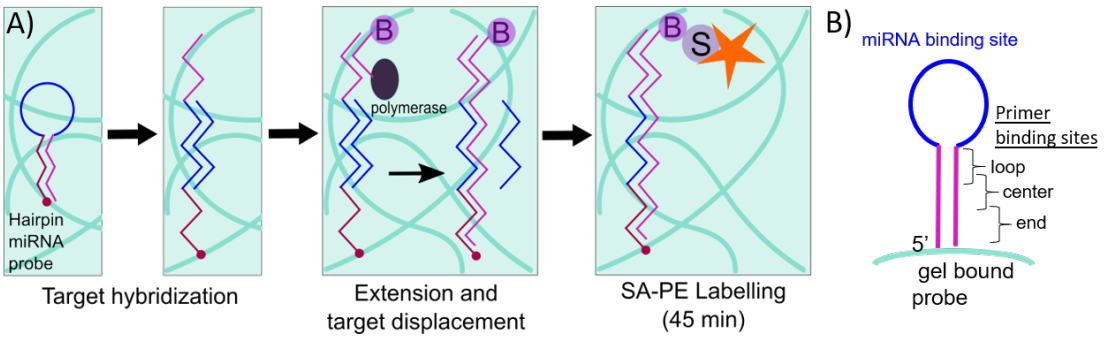

Figure 4-5: A) miRNA target binding opens the probe allowing the biotinylated primer to bind, which is then extended by a DNA polymerase. SA-PE is used to label the extended strands. B) A diagram of the different parts of the hairpin probe that will be referred to in this study.

4.3.1 Experimental

For solution assays, a molecular beacon probe with the same sequence as the acrydite probes used for particle assays was purchased from IDT DNA. It contained a FAM group on the 5' end and a Iowa Black FQ quencher on the 3' end. Target hybridization was conducted in the recommended buffer for the polymerase at 55°C for 90 minutes on a thermoshaker with shaking. After 90 minutes, the thermoshaker temperature control was turned off and the reaction was allowed to naturally cool down over the course of 30 minutes with shaking. After cooling down, the reaction tubes were kept on ice while the amplification reagents were added. Each reaction was supplemented with 1 μM primer (no modifications), 250 μM dNTP mix (New England Biolabs), and 0.1 U/μL polymerase (New England Biolabs). The reaction was pipetted into a qPCR plate in duplicate or triplicate (each well was 50 μL). The plate was sealed with PCR film and kept on ice until loading into the machine. An isothermal amplification was carried out in the qPCR at 45°C for varying amounts of time.

For particle assays, particles were co-polymerized with hairpin DNA probes specific to different miRNA as described in Chapter 2. A graphical code in the center of the particle encoded for the miRNA target. The particles (25 particles for each miRNA, per tube) and synthetic miRNA targets were combined in 1X NEB 2 buffer (New England Biolabs) supplemented with 300 mM of NaCl (final NaCl concentration of

350 mM). The increased salt concentration has previously been demonstrated to increase hybridization [70]. Target hybridization was conducted at 55°C for 90 minutes on a thermoshaker with shaking. After 90 minutes, the thermoshaker temperature control was turned off and the reaction was allowed to naturally cool down over the course of 30 minutes with shaking. After cooling down, the reaction tubes were washed 3 times with 1x NEB2. To each reaction tube, 5 µL of 10 µM biotin primer, 1.25 µL of dNTP mix, and 1 µL (5 U) Klenow exo$^-$ polymerase (New England Biolabs) was added. A master mix of reagents for all tubes was prepared to avoid pipetting small volumes. The amplification reaction was conducted at 37°C for 60 minutes on a thermoshaker with shaking. After amplification, reaction tubes were immediately placed on ice to stop the reaction. Particles were then washed 3 times with rinse buffer (TET + 50 mM NaCl). For labelling, particles were incubated with 5 µL of 20 µg/ml streptavidin-phycoerythrin (SA-PE) for 45 minutes at 21.5°C on the thermoshaker. Particles were washed 3 times with rinse buffer to remove excess SA-PE, and then imaged and analysed according to the methods described in Chapter 2.

4.3.2 Solution-based Assay Optimization

A screen of various strand displacement polymerases used in literature for strand displacement amplification was performed using the molecular beacon-based solution assay using a 9 nt end primer [121–123]. The polymerases included the Bst family (Bst 3.0, Bst 2.0, Bst LF), and Klenow exo$^-$. An amplification temperature that was suitable for all the enzymes was chosen (45 °C), since preliminary studies showed successful results at this temperature with Bst 3.0 polymerase (higher temperatures lead to high non-specific signal in preliminary experiments with particles). This is below the optimum temperature for the Bst family (55-65°C), and slightly higher than the recommended temperature for Klenow exo$^-$ (37 °C). At higher temperatures, while Bst polymerases were more active, the hairpin probe was more likely to open. Thus the lowest possible temperature suitable for enzymatic activity was desired. From figure 4-7, it is evident that Klenow exo$^-$ outperformed the Bst family in terms of polymerization efficiency.

Subsequently, using Klenow exo$^-$, a primer screen was conducted in which a variety of primers targeting different regions of the hairpins and different lengths were tested. The regions are identified in figure 4-5B. Both the loop primers showed the best performance, with the 9 nt primer significantly outperforming the rest. This data corroborates theoretical simulations performed on Multistrand (Multistrand.org) [124, 125], in which the stem closest to the loop was less likely to open than other end of the stem as shown in figure 4-6. Based on these solution-based optimization studies, a 16 bp stem with 9 bp primer closest to the hairpin loop using Klenow exo$^-$ polymerase gave the highest amplification efficiency.

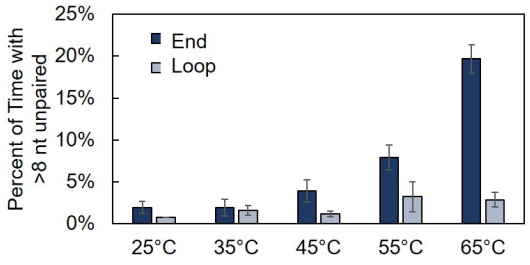

Figure 4-6: Results from simulating a 16bp stem probe for let-7a in "Transition" Mode at various temperatures for 0.01s in Multistrand [124]. The two states (ends and loop) correspond to when >8 nt in those regions are unpaired in the stem.

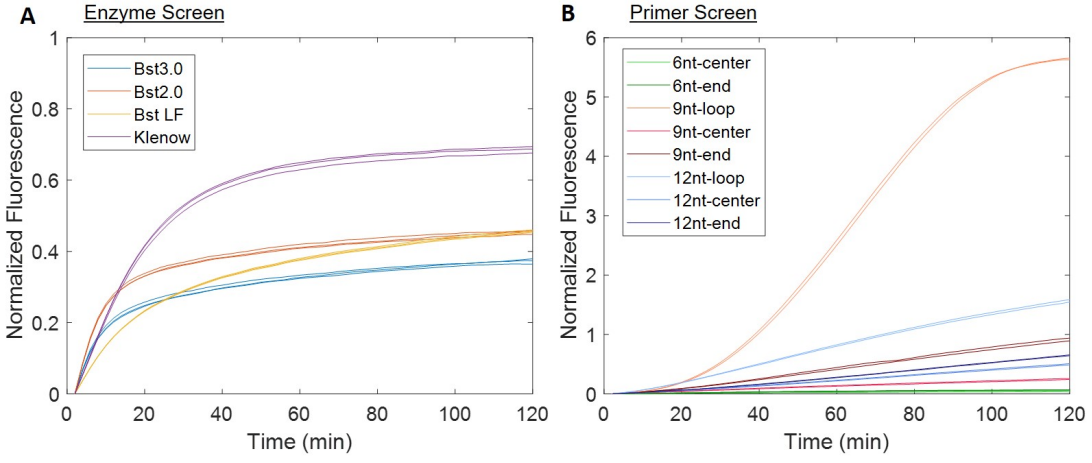

Figure 4-7: A) A screen of 4 different polymerases used for hairpin strand displacement amplification with a 9 nt end primer. B)A screen of various primers of different lengths and target binding locations for hairpin strand displacement amplification. For both experiments, amplification was conducted at 45 °C for 2 hours with equal amounts of target, dNTPs, primers, and equal units of enzyme. Averages of 3 replicate reaction wells are taken and the no target control averages are subtracted from that. This net signal is then normalized by the initial fluorescence value so that all curves start at the same baseline (differences in baseline occur due to different buffers for each polymerase.)

4.3.3 Hydrogel Particle-based Assay Optimization

A hydrogel-based primer screen was conducted as well, using the three 9 nt primers (loop, center, end) and a probes with varied stem length. The 12 bp and 14 bp stem probes give rise to rapid and efficient amplification, however, the negative control (no target) signal also increases, reducing the signal-to-noise ratio (SNR). The highest SNR was achieved by the longest tested stem probe (16 bp), with the 9 nt loop primer, corroborating the results seen in solution. These experiments were conducted with a FAM-labelled primer instead of a biotinylated one in order to remove the possibility of steric hindrance effects associated with SAPE labelling. Along this vein, a series of experiments were also done whereby biotin primers with different length poly-A tails were used to see if the increased distance from the hybridization duplex improves SAPE labelling, a strategy used in the standard miRNA assay [45]. However, the increased mobility for SAPE labelling comes at the cost of more difficulty for the primer to bind to the hairpin and be extended. Thus a primer with no tail gave the highest SNR.

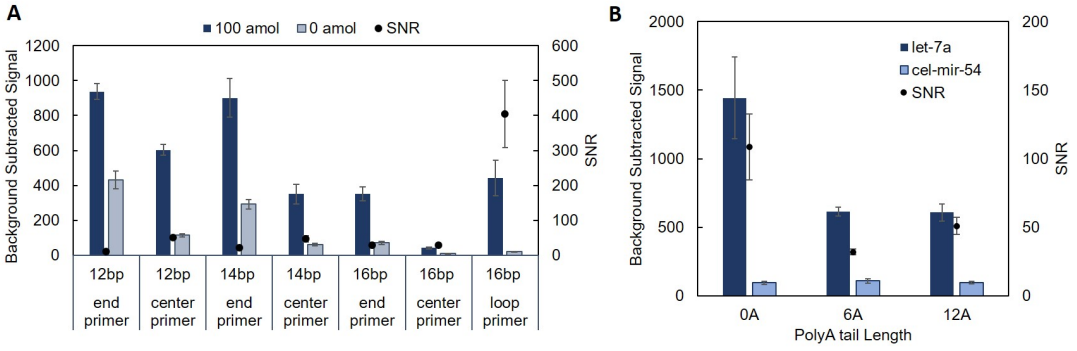

Figure 4-8: A) Background subtracted signal from SDA assay on particles using various probe length and primer location combinations. FAM-labelled primers targeting various locations and probes with varying stem lengths were tested with either 100 amol let-7a target or 0 amol (control). B) Background subtracted signal from SDA assay on particles with 16 bp stem probe and 9 nt loop primer, with either a 0, 6, or 12 poly-A tail, capped with biotin. SAPE was used to label the biotin primers after amplification. *cel*-miR-54 particles were used as the control.

Finally, a calibration curve was undertaken using the optimized primer-probe pair and polymerase conditions as shown in Figure 4-9. The hairpin SDA can give rise to rapid and efficient amplification, however, the negative control (no target) signal also had a relatively high and variable signal, resulting in no substantial improvement

in the limit of detection over the standard un-amplified assay (0.37 amol vs. 2 amol). It is hypothesized that the long (52 nt, ∼16 nm) hairpin probe is hindered by the hydrogel crosslinks (PEG 700 length ∼4 nm), preventing proper closing of the hairpins after hybridization. This causes the increased non-specific signal seen in particles, that is not present in the solution assay format. Moreover, the high probe concentration: target amount ratio used in hydrogel assays is many orders of magnitude higher than what is typically used for solution assays [121]. This means that even if 0.01% of probes are open in a hydrogel, a large non-specific signal is generated.

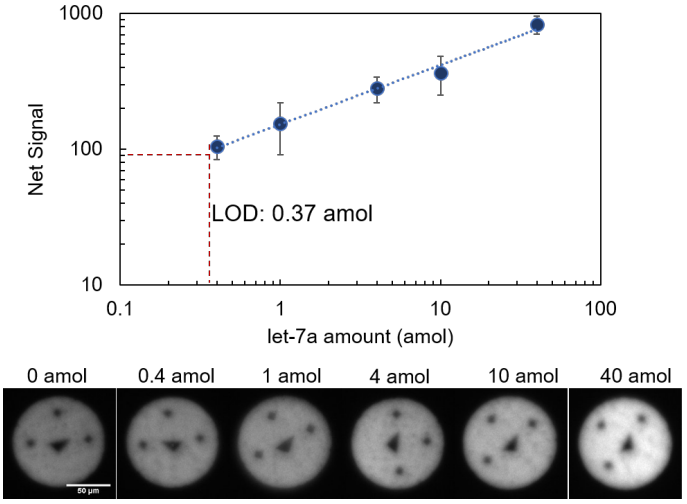

Figure 4-9: SDA Calibration curve for let-7a using a 9 nt loop primer with 16 bp stem probe, with 1 hour of amplification at 37 °C. Error bars represent 1 standard deviation. Representative images of particles at different miRNA concentrations are shown. Scale bars are 50μm

4.4 Concluding Remarks

In conclusion, we pursued two different amplification strategies to increase miRNA detection sensitivity, necessary for detection of many relevant miRNA in biologic samples like serum, urine, and extracellular vesicle fractions. The first was an enzymatic amplification strategy, utilizing the ELF-97 phosphatase substrate system, in which the cleaved product precipitates out of solution, whilst staying confined within the hydrogel matrix. This strategy was most suitable with hydrogel posts in which the LOD for biotin probe hydrogels was 1.24 nM, a slight improvement compared to directly labelling the biotin with SAPE (LOD of 2.34 nM). Attempts

to improve the conditions for precipitation by increasing temperature or substrate concentration did not result in improvement to the LOD. It was hypothesized that the minimum concentration threshold to trigger precipitation out of solution had not been reached and hence why the amplification factor at low biotin concentrations was small. There was however anecdotal evidence that changing the relative hydrophobicity of the hydrogels, by tuning the hydrogel chemistry may result in a much lower concentration threshold to trigger precipitation. This is based on the fluorescence seen from underpolymerized posts. Studies have been conducted on tuning hydrogel chemistry for the purpose of wetting applications [126], and we believe that similar concepts could be applied to tuning the hydrogel chemistry to decrease the relative hydrophobicity of the hydrogels to promote faster precipitation.

The second strategy was a nucleic acid amplification approach utilizing a hairpin probe for strand displacement amplification. SDA relies on the opening of a hairpin probe upon hybridization to the target. The opening allows a biotin primer to bind, which is then extended by a strand displacing polymerase. The displaced strand, the target, is allowed to bind to another hairpin probe. Thus, the target recycling enables rapid isothermal amplification. Optimization studies were performed in both solution-based and particle-based assay formats. Based on these optimization studies, a 16 bp stem with 9 bp primer closest to the hairpin loop using Klenow exo$^-$ polymerase gave the highest amplification efficiency. When adapted to particles the amplification was rapid and efficient, however, the negative control (no target) also had relatively high and variable signal, resulting in minimal improvement in the limit of detection over the standard un-amplified assay (0.37 amol vs. 2 amol). It is hypothesized that the long (52 nt, $\sim$16 nm) hairpin probe is hindered by the hydrogel crosslinks (PEG 700 length $\sim$4 nm), preventing proper closing of the hairpins after hybridization. This causes the increased non-specific signal seen in particles, that is not present in the solution assay format.

A few approaches are possible to address this limitation: the first is to conduct hybridization at low temperatures (i.e. 37 °C), such that the chance of hairpin opening during hybridization is minimized even further. These 16 bp hairpins have $T_m \sim 80$

°C, however even the current hybridization temperature of 55°C results in a small fraction of the hairpins to open, based on NUPACK thermodynamic analysis [127]. The specificity of the system for nucleotide mismatch discrimination at lower temperatures would need to be assessed, since there is some evidence to suggest that specificity for discrimination within the let-7 family decreases with decreasing hybridization temperature [70]. Another approach would be to increase the porosity of the hydrogel such that the hairpins can fold freely. Chapter 6 describes the synthesis of ultraporous hydrogels using large molecular weight PEG porogens. Similar approaches, or the use of larger molecular weight PEGDA as the crosslinker may be used to create such hydrogels. If these limitations are addressable, SDA has the potential to drastically improve limits of detection even at relatively short amplification times of 1-2 hours. ($\sim$ 4 hours total assay time).

Extracellular Vesicle microRNA Detection

In this chapter, we show the development and application of a method for quantitative and multiplex detection of extracellular vesicle-derived microRNA (EV-miRNA), via rolling circle amplification within encoded hydrogel microparticles. Via a one-pot extracellular vesicle (EV) lysis and miRNA capture step, we avoid the bias and losses associated with standard RNA extraction techniques. Orthogonal measurements of EV concentrations coupled with the direct, absolute quantification of the miRNA in the sample, results in quantitative measurements of miRNA copy numbers per volume sample, and per extracellular vesicle.

5.1 Introduction

MicroRNAs are short non-coding RNA that have emerged as highly promising diagnostic and prognostic biomarkers due to their gene regulatory functions and dysregulated patterns in many diseases including cancer [13, 14]. miRNAs have remarkable stability in blood in body fluids due to their association with proteins, and packaging within extracellular vesicles (EVs) [14, 18, 19]. Extracellular vesicles themselves are an emerging biomarker and have been implicated in a variety of biological functions, including disease progression, drug resistance and can act as a form of inter-cellular communication [5, 11, 128]. The contents within exosomes and other microvesicles are actively exported by the parent cells, and as such, EV-miRNAs are a particu-

lar attractive biomarkers, since they offer insights into disease conditions associated with the parent cells, while being easily accessible from bodily fluids such as serum and urine [113, 129].

Traditional strategies for miRNA detection, including reverse-transcription qPCR and microarrays, offer limited multiplexing and involve complex multistep procedures [43]. Moreover, quantitative detection with these traditional approaches is very difficult and seldom demonstrated in literature [45]. Many of the difficulties inherent to miRNA detection, such as sequence homology and variable expression levels, are also prevalent in EV-miRNA detection. Moreover, RNA isolation from EVs are itself a source of loss and bias, that can confound interpretation of results [130]. There are many studies that have profiled panels of EV-miRNA in a range of biofluids, however the differences in RNA isolation, EV isolation, and difficulties in data normalization with PCR-based and RNA-seq data makes comparison with other studies and absolute quantification difficult [21, 129, 131]. Few studies have also detected EV-miRNA directly from isolated EVs [23, 35, 114, 132, 133], however the demonstrated multiplexing ability is limited. Data on absolute EV-miRNA quantification is limited and highly desired to further research into the function of miRNAs transported in the body via exosomes and other vesicles.

The Doyle group has developed hydrogel microparticles, which are functionalizable, non-fouling and compatible with a variety of complex samples, facilitating direct miRNA detection from serum, cell lysate and FFPE tissue sections [67, 76, 115]. These particles demostrate favorable solution kinetics for RNA hybridization and are synthesized using a technique called stop-flow lithography, enabling graphically-encoded multiplexing. [45, 73, 105]. Utilizing the benefits of hydrogel microparticles for miRNA detection, this work presents a facile and sensitive technique for multiplexed detection of EV-miRNAs. After EV isolation from serum, the assay involves a one-pot EV lysis and miRNA capture step within encoded hydrogel microparticles. To achieve the sensitivity required for quantitative detection, an isothermal amplification strategy is exploited based on rolling circle amplification (RCA), which amplifies the signal instead of the target, avoiding the biases common in PCR as-

says Furthermore, the present system offers a large dynamic range (3 orders of magnitude), ease of multiplexing, and a sensitive zmol range limit of detection, demonstrating its utility and promise for use in clinical applications.

5.2 Experimental

5.2.1 Extracellular Vesicle Isolation using PEG Precipitation

Serum aliquots were thawed in a water bath at room temperature and then centrifuged at 2000g for 30 minutes to clarify the serum and remove debris. Aliquots of both raw and clarified serum were made the first time the serum was thawed and then stored at -20°C for subsequent use. EVs were isolated using a modified PEG precipitation recipe. A 60% w/v PEG 6000 solution was made by dissolving PEG 6000 in nuclease-free water and stirring on a hot plate at 60°C until the solution was clear and uniform. This solution was stored at 4°C. The PEG solution was added to the clarified serum in a 5:1 ratio resulting in a final concentration of 10% (w/v) PEG 6000. The mixture was thoroughly pipette mixed until it turned cloudy white and then stored upright at 4°C for 30 minutes. The mixture was then centrifuged at 10,000g for 10 minutes at room temperature. The supernatant was carefully removed without disturbing the pellet using a pipette tip. The pellet was resuspended in 20 nm filtered PBS (PBS filtered through a 20 nm Anotop syringe filter (Whatman)) by gentle mixing on a thermoshaker at room temperature for 30 minutes. The PBS volume was either the same as the starting serum volume (1x EV concentration) or 4-fold less (4x EV concentration). The purified EVs were split into aliquots and stored at 4°C for up to 48 hours, and then stored at -20°C for medium term storage (1 week to 2 months). For long term storage, EV and serum aliquots were moved to -80°C. It should be noted that initial experiments used a PEG reagent formulation with 0.5 M NaCl, however, the salt content occasionally caused difficulties in re-suspending the precipitated pellet.

5.2.2 Extracellular Vesicle Quantification

Nanparticle Tracking Analysis

EVs isolated from serum were diluted 10,000x in 20 nm-filtered PBS and introduced to the measurement chamber via a syringe pump. 31 videos, 30s each were taken of the particle scatter, with a 5s flush (at 150 μL/min) in between to introduce new particles into the field of view. A MATLAB script controls the syringe pump to coordinate with the timing of video acquisition. The detected number of particles in a field of view determines the absolute concentration measured by the Nanosight, while the particles with completed tracks informs the size distribution.

Microfluidic Resistive Pulse Sensing

EVs isolated from serum were diluted 200x-1000x in 20 nm-filtered PBS with 2% tween-20 and a 5 μL sample was added to the disposable chip and inserted into the instrument according to manufacturer protocols. At least 1000 particle events were collected for the size range of interest. The data was filtered according to user-defined thresholds and filters such that only events with diameters $>$75 nm, S/N $>$25 and transit time$<$80 ms were included for analysis. While the C-300 chips could reasonably detected smaller particles (down to 65 nm accounting for the noise floor), a higher threshold was set so that concentration values could be comparable with the C-400 chips. These filters were set based on calibration runs of NIST-certified calibration beads.

Protein Analysis

The Bio-Rad Protein Assay (based on the Bradford assay) was used for total protein quantification. A working dye reagent solution was made by mixing 1 part dye reagent concentrate with 4 parts DI water and then vacuum filtering through filter paper. This working solution is stable for 14 days at room temperature. EVs isolated from serum were diluted 10-30x in 20 nm-filtered PBS. 10 μL of each diluted sample was pipetted into a 96-well plate in triplicate. 200 μL of working dye reagent solution was added to each well and pipette-mixed. After 10 minutes, the absorbance of the

solutions were measured at 610 nm. A BSA calibration curve was prepared and tested at the same time for quantification. The standard curve was fit to a 3rd order polynomial and protein values were extrapolated using this equation of best fit.

5.2.3 Extracellar Vesicle Lysis

miRNA hybridization experiments optimizing lysis conditions were conducted using the standard assay as described in chapter 2. The hybridization buffer was modified with added SDS (2-5%). The EV sample was pre-heated for either 60°C or 90°C for varying amounts of time in the modified lysis and hybridization buffer. After lysis, 1 µL of Proteinase K (stock at 800 U/ml, NEB) was added to each tube along with particles containing probes for miR-21, *cel*-miR-54 (positive control), and *cel*-miR-39 (negative control). Finally 100 amol synthetic *cel*-miR-54 target was spiked into each tube.

Varying concentrations of SDS (0.5-5%) were assessed for performance and compatibility with miRNA hybridization. Lysis performance was assessed using Calcein AM, as an indicator for intact membranes. The dye molecule is non-fluorescent until it enters the EVs and is cleaved by esterases into a fluorescent product [134]. Isolated EVs from Sigma Aldrich serum were combined with lysis bufffer containing various SDS concentrations for 20 minutes at 60°C. Calcein AM dye was added at a 1:100 dilution of the stock solution, to a final concentration of 10 μM and incubated for 20 minutes at 37°C to promote esterase activity. The fluorescence was measured in a Tecan F200 Plate Reader with an excitation of 485 nm and emission of 515 nm in a black-walled 96-well plate.

5.2.4 microRNA Detection

The standard assay was conducted as described in chapter 2, with the additional optimized lysis protocol detailed below: 25 µL of purified EVs (1x or 4x concentration) was combined with 5 µL of 3.75 M NaCl and 10 µL of 25% w/v SDS. Both the NaCl and SDS solutions were made in 1x TE buffer with 0.125% Tween-20. EV lysis was conducted for 20 minutes at 60°C. After lysis, 1 µL of Proteinase K (stock at 800

U/ml, NEB) was added to each tube along with particles containing miRNA-specific probes were added to the reaction (25 particles per miRNA target per reaction), and positive control target spike-in, cel-mir-54. The final lysis-hybridization buffer composition was 5% SDS, 16 U/ml Proteinase K, 350 mM NaCl, and 0.05% Tween-20 in 1xTE in a 50 µL reaction volume. Hybridization was conducted at 55°C for 90 minutes, followed by 30 minute ligation at 21.5°C, and 45 minute SAPE labelling at 21.5°C. The particles were washed 3 times with rinse buffer in between steps. Details of the standard assay protocol are in Chapter 2.

For RCA, the circular template DNA was prepared based on a published protocol [135]. Briefly, a 50 nt linear precursor DNA was circularized using CircLigase II followed by enzymatic deactivation, exonuclease digestion, and purification using 30 kDa centrifugal filters. RCA-based miRNA detection deviates from the standard assay at the ligation step. Instead of a biotinylated linker, a linker sequence complementary to the circular template was ligated to each miRNA-probe complex. The circular template was then annealed to the linker and amplification was conducted for 4h at 30°C by the addition of Phi29 polymerase and dNTPs, generating a long ssDNA concatemer. Two distinct biotinylated reporters were used to tag the concatemers, followed by labelling with SAPE. Figure 5-1 presents a schematic of both the lysis and RCA assay for particle-based EV-miRNA detection.

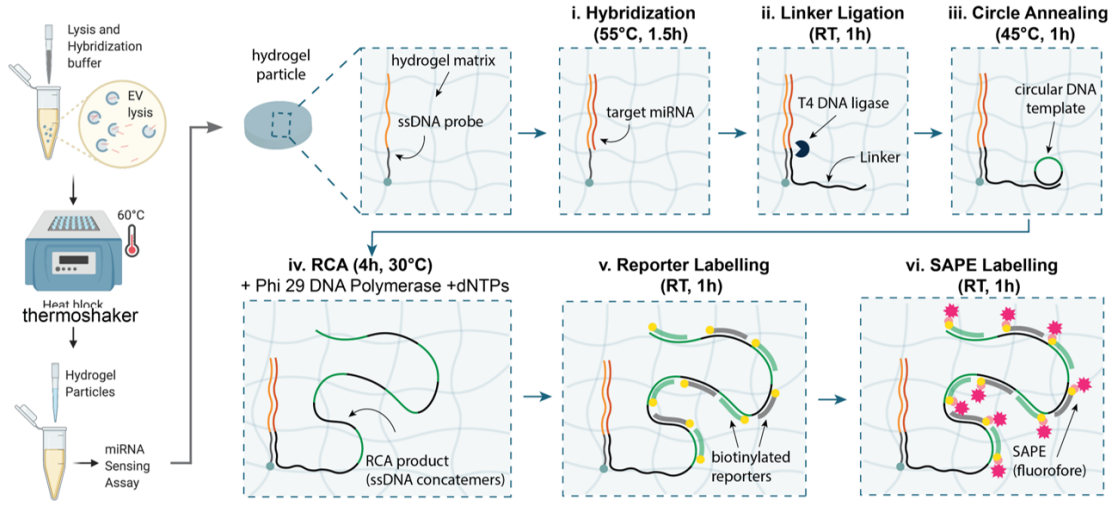

Figure 5-1: Schematic illustration of one-pot lysis and miRNA capture, followed by RCA in hydrogel microparticles.

5.3 Results and Discussion

5.3.1 Extracellar Vesicle Isolation and Quantification

There are numerous methods for EV isolation, the most popular being ultracentrifugation, size-exclusion chromatography or polymeric-reagent based precipitation.[26, 29, 136]. The table in figure 5-2 below from a review article by Yang and colleagues shows an overview of the numerous methods of EV isolation. [12]

Table 1. Current strategies for exosome separation

Isolation technique	Principle	Advantages	Disadvantages
Sequential ultracentrifugation	Particles have different density and size show different sediment speed under centrifugal force	• Low cost and • Low contamination risk with extra isolation reagents; •suitable for large volume preparation;	• High equipment requirement • Time consuming • Labor intensive • Potential mechanical damage due to high speed centrifugation • Protein aggregation • Not suitable for small volume diagnosis • Low portability
Gradient ultracentrifugation	After centrifugation in a dense medium, objects in a tube could stay in the position of the medium with similar density	• High purity of products • Allowing separation of subpopulation of exosomes	• Lower volume processability • High equipment requirement • Time consuming • Labor intensive • Potential mechanical damage due to high speed centrifugation • Not suitable for small volume diagnosis • Low portability
Ultrafiltration	Utilizing filter membrane with defined size-exclusion limit or molecular weight cut-off	• Low equipment cost • Fast procedure • good portability	• Moderate purity • Potential deterioration induced by shear stress • Possible loss due to clogging and membrane trapping
Size-exclusion chromatography	After adding to porous materials, substances eluted out in accordance with their particle size, with big particles eluted earlier	• High purity • Fast preparation • Keep native state of exosomes • Good reproducibility • Potential for both small and large sample capacity; • Capable of processing all type of samples	• Relatively high device costs • Additional method for exosome enrichment is required
Polymer Precipitation	High hydrophilic water-excluding polymers can alternate the solubility of exosomes	• Easy to use • Using ordinary equipment •Suitable for both small and large sample volume • High efficiency	• Contaminants of protein aggregates, other extracellular vesicles and polymeric contaminants • Extended processing time • Require complicated clean-up steps • Affecting downstream analysis and quantification
Immunoaffinity capture	Based on specific binding between exosome markers and immobilized antibodies (ligands)	• Suitable for separating exosomes of specific origin; • High-purity exosomes • Easy to use • No chemical contamination	• High-cost antibodies; • Exosome markers must be optimized • Low processing volume and yields • Extra step for exosome elution may damage native exosome structure
Microfluidics-based techniques	Based on different principles including immunoaffinity, size and density	• Highly efficient • Cost-effective • Portable • Easily automated & integrated with diagnosis	• Low sample capacity

Figure 5-2: Overview of exosome isolation techniques.[12]

In this thesis work, polyethylene glycol (PEG)-based precipitation was used for EV isolation. It is faster and more accessible than ultracentrifugation [12]. Moreover, given that the hydrogel particles used for miRNA detection are also PEG based, the potential issues related with the PEG reagent interfering with downstream analysis is not a concern [12]. While there are numerous commercial reagents avail-

able such as ExoQuick (System Biosciences) and Total Exosome Isolation Reagent (ThermoFisher), an in-house PEG recipe was used based on commercially available formulations and similar usage in literature[26, 28, 29, 137]. The in-house formulation consists of 10% PEG 6000 (final concentration mixed with serum). This formulation produced similar results as compared to the commercially available ExoQuick reagent as shown in figure 5-3. Human healthy serum from male AB -plasma (Sigma-Aldrich H4522) was used as the EV source for all optimization experiments related to EVs. For miRNA dysregulation studies, single-donor lung cancer serum and matched healthy serum (AmsBio) were used. Both donors were female in their 50s.

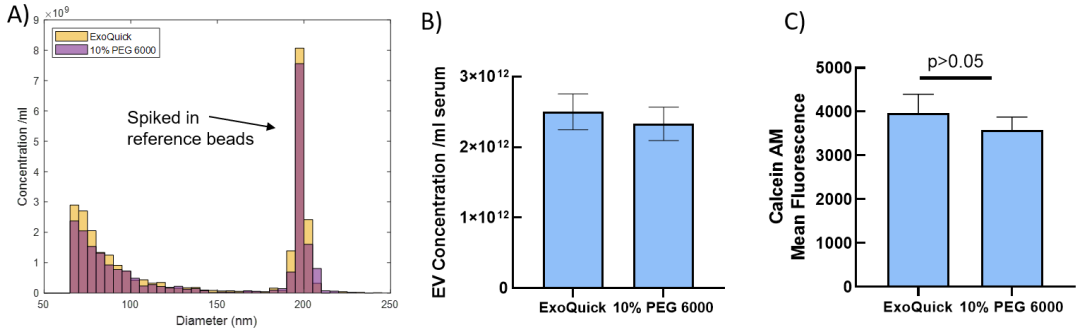

Figure 5-3: A) Particle size distribution and B) concentration based on MRPS measurements and C) membrane integrity as assessed by Calcein AM stain show no difference in the EVs isolated between ExoQuick and 10% PEG 6000. Exoquick isolation was conducted using the manufacturer's instructions.

Due to their size, exosomes and small EVs cannot be seen or measured with traditional light microscopy methods. In this thesis, two methods were used to for EV concentration measurements: nanoparticle tracking analysis, and microfluidic resistive pulse sensing. Additionally, total protein quantification was assessed using the Bradford Assay and membrane integrity was assessed with calcein AM stain [134].

Nanoparticle tracking analysis (NTA) is commonly used in the EV research community to characterize exosomes based on size distributions [7, 138, 139]. It is based on the forward scattering of light as a particle illuminated by a UV laser as it undergoes brownian motion in a defined fluid volume. The video camera records the scatter from the particles, and the associated software tracks individual particles in the field of view, generating a set of mean-square displacements (MSD) and position data for

each particle. It calculates a radius of the particle using Stokes-Einstein law based a calculated diffusivity of the particles based on the MSD data [138, 140]. Figure 5-4A below shows an example size distribution profile of lung cancer and matched healthy patient serum EVs.

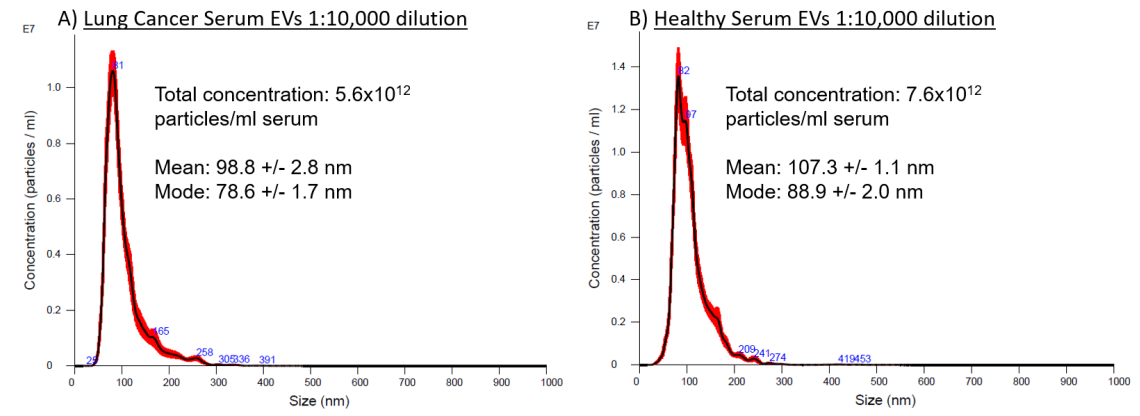

Figure 5-4: Concentration and size distribution of EVs isolated from matched lung cancer and healthy human serum as determined by NTA and standard Nanosight software.

There are a few problems associated with using NTA for EVs:

1. Larger particles scatter much more strongly than smaller ones, in a highly non-linear fashion. This can cause larger particles in a sample to block the scatter from neighboring small particles, hiding them from detection.

2. The scattering from a particle that index matches the fluid, like EVs, is much less than that from particles with higher index of refraction like polystyrene. This results in the scatter from small EVs to be too faint for detection.

3. For a polydisperse sample, when the particle size distribution is calculated based on diffusivities from individual particle tracks, the calculated size distribution will only converge to the true size distribution in the limit of infinite number of tracks and track length. Thus even with many particle tracks measured, the inherently finite length of each track (since the particle diffuses out of the field of view), results in a biased size distribution [140].

Thus, while NTA is quite suitable for solid, fairly monodisperse samples, it can artifically skew the size distribution towards higher diameters and give rise to a false

peak with EVs [139, 141].

As an orthogonal method to NTA, we utilized microfluidic resistive pulse sensing (MRPS) to assess EV size distribution and concentration. MRPS is based on a principle similar to a Coulter Counter in that a particle going through the measurement nanoconstriction results in a voltage drop proportional to the volume of the particle [139, 142, 143]. MRPS is conducted on the Spectradyne nCS1 instrument using both the C-300 (50-300 nm range) and C-400 (65-400 nm range) chips [139, 141]. The actual minimum detectable size for each chip is generally higher than the nominal size range, even in clean calibration bead runs, due to instrument noise. The high 2% tween-20 concentration was found to be necessary to ensure adequate priming of the chips, since each chip contains hundreds of constrictions upstream of the measurement nanoconstriction, which act as a filter. This high tween-20 concentration used during measurement is not expected to cause any changes or degradation to the EV samples based on studies of detergent sensitivity that found that exosomes are remarkably resistant to degradation even in the presence of up to 10% tween-20 [144]. NIST-certified calibration beads can be added to the sample for *in situ* calibration of the size and concentration, however, in our experience, it was found that samples with spiked-in calibration beads (from Polysciences) behaved differently from those without. The spiked-in calibration bead runs were not as consistent (i.e. from chip to chip, day-to-day), and sometimes would simply not show any measurable particles. It is hypothesized that interactions between the EVs, proteins (and other potential contaminants like lipoproteins) and the beads may have caused blockage events in filter region of the chip, where there are many nano-sized constrictions. Thus, the data presented below is for samples measured without any calibration beads.

Figure 5-5 shows the size distribution profile of lung cancer and matched healthy patient serum EVs, and the measured concentration (per ml serum), using the same filter thresholds for both cancer and healthy serum EVs. The protein measurements based on Bradford Assay indicate similar protein concentrations among cancer and healthy EVs ($p>0.05$) as shown in Figure 5-5.

These concentration measurements are comparable to and corroborate the NTA-

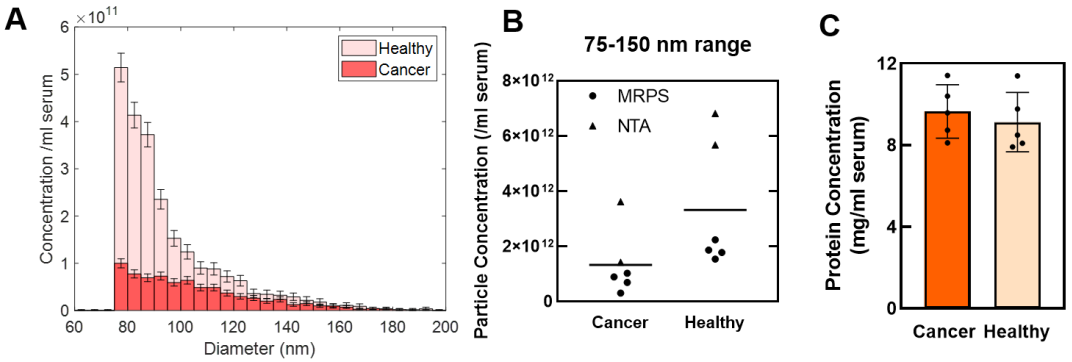

Figure 5-5: A) Size distribution of EVs (1:500 dilution) isolated from matched lung cancer and healthy human serum as determined by MRPS. Thresholds are diameter>75 nm, S/N >25 and transit time<80 ms. B) EV concentration measurements from MRPS and NTA. MRPS measurements were made at 3 different dilutions (1:200, 1:500, 1:1000), and the 1:500 was analysed in two different chips (C-300 and C-400), resulting in 4 replicate measurements that all agree with each other. NTA measurements were made at 2 different dilutions (1:5000 and 1:10,000). C) EV protein concentration measurements from lung cancer serum and healthy EV samples calculated from technical replicates at various dilutions (1:10, 1:20, 1:30).

based measurements over the same size range. Since MRPS is not an optical method and the voltage drop is only dependent on the volume of the particle (not surface charge, or density, etc.), the size bias that exists with NTA is not present in these measurements. The size distribution profiles follow a power-law function that has been reported to represent EV size distributions [139, 145]. The raw diameter vs. transit time data for both sets of EV samples are shown in figure 5-6. The healthy sample shows many particle detection events very close to the noise floor at 65 nm, that cannot be effectively separated from the noise floor. In comparison, the cancer sample shows a much lower and cleaner noise floor. It is hypothesized, that the increased noisiness of the healthy sample is due to the relatively higher levels of contaminating particles within it. This limited detection sensitivity in the <70 nm range, renders it difficult to differentiate between noise and true particle events and hence a high size cut-off of 75 nm is chosen to compare concentration measurements between samples, and between NTA and MRPS.

Overall, the serum EV concentrations based on two orthogonal measurement methods are in agreement with each other and what is expected by a precipitation method of isolation [146]. Interestingly, normal serum had more EV-sized particles as compared to cancer serum. While there are limitations in detection sensitivity associated

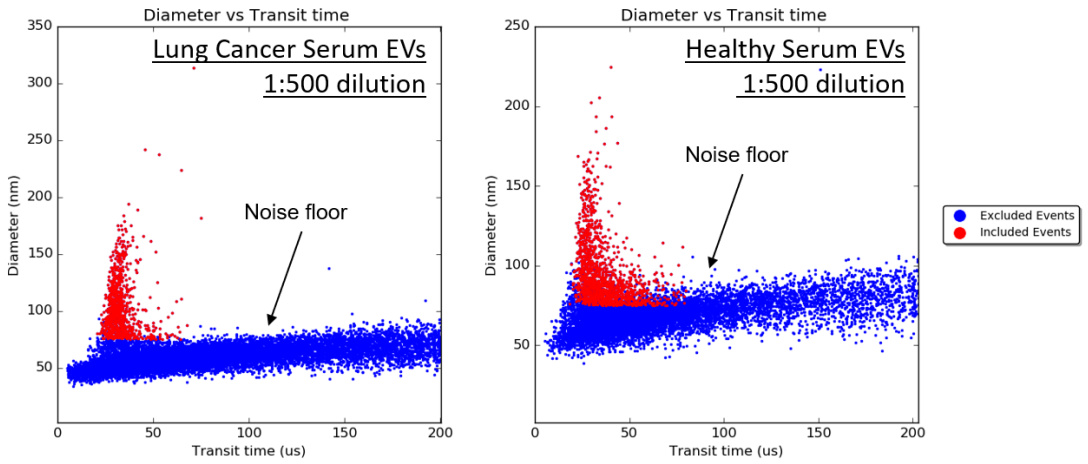

Figure 5-6: Raw diameter vs. transit time for 1:500 dilution of lung cancer and healthy serum EVs. The noise floor is indicated by the arrows.

with MRPS, it avoids the biases associated with NTA measurements, which are inherent to optical scattering methods. As such, the MRPS measurements give an unbiased estimate for absolute EV concentration for a defined size range and are used for miRNA stoichiometry calculations.

5.3.2 Extracellular Vesicle Lysis Optimization

The PEG hydrogel microparticles created using SFL have been shown to be non-fouling and compatible with a variety of complex samples like serum, cell lysate and FFPE tissue sections [67, 76, 115]. In these previous works, a one-pot lysis and hybridization step was implemented with an optimized lysis and hybridization buffer consisting of 2% SDS and 16 U Proteinase K in a TET buffer with a final salt concentration of 350 mM (accounting for the salt concentration of the sample). The SDS served as a lysing agent and the proteinase K degraded any RNA-associated proteins to release the bound miRNA. This lysis buffer was taken as the starting point for optimization of lysis of EV samples.

Initially, the protocol used for serum was utilized (given that the EV source is serum), in which the sample was mixed with the lysis buffer (without proteinase K) and then heated to 90°C for 10 minutes. Proteinase K, particles and synthetic positive control target were then added to the mix [76]. This protocol, when used

with 4x concentrated EVs, resulted in very high levels of non-specific signal on all miRNA probe particles in the assay, including the negative control *cel*-miR-39 particles. Increasing the time for this pre-heat step to 20 minutes lowered the non-specific signal marginally. However, by reducing the temperature to 60 °C, this non-specific signal was eliminated as shown in Figure 5-7. It was hypothesized that the non-specific signal at 90 °C was caused by lipids and lipoproteins sticking to the particles causing SAPE to stick during the labelling step, based on a series of experiments with PKH-26 staining of the particles. Since the lipid and lipoprotein content is highly dependent on the donor of the serum, we found that single donor serum from BioIVT had this non-specific signal, while pooled, male healthy donor serum from Sigma Aldrich did not. To ensure that the protocol would be valid for any type of serum sample, a 60 °C pre-heat step for 20 minutes was chosen for EV lysis.

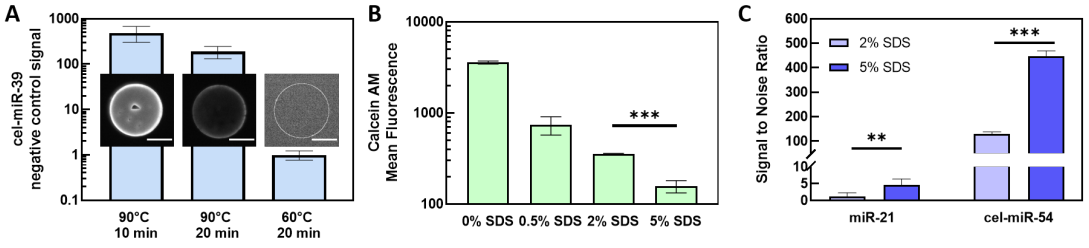

Figure 5-7: A) Effect of lysis temperature on non-specific signal on negative control *cel*-miR-39 particles. Representative images of negative control particles showing the extent of non-specific signal. Right-most particle is thresholded to show that no fluorescence is visible. B) Mean Fluorescence from EVs lysed with varying SDS concentration and subsequently incubated with Calcein AM dye. C) Signal-to-noise ratio from serum EVs after lysis with either 2% or 5% SDS (60°C, 20min lysis). The noise is calculated based on the standard deviation of the negative control *cel*-miR-39 signal. *cel*-miR-54 represents the positive spike-in control. Error bars throughout represent 1 standard deviation.

Additionally, the SDS concentration for EV lysis was optimized to maximize exosome rupture without inhibiting miRNA hybridization using calcein AM dye as a indicator for intact membranes[134]. Compared to previous work with cells, EVs have greater membrane surface area at the concentrations used for these assays. Thus it was hypothesized that 2% SDS may not be sufficient for complete lysis of the EV sample. Calcein AM dye was used as an indicator for intact membranes. The dye molecule is non-fluorescent until it enters the EVs and is cleaved by esterases present in intact EVs into a fluorescent product [134]. The results, shown in figure 5-7, show a clear

decrease in fluorescence with increasing SDS concentration.

miRNA hybridization efficiency was also assessed at 2% and 5% SDS to ensure that the high SDS concentrations did not interfere with hybridization. A standard assay was conducted with 4x Sigma Aldrich EVs with particles containing probes for miR-21, *cel*-miR-54 (spiked-in positive control), and *cel*-miR-39 (negative control). Figure 5-7 shows both the net signal and signal-to-noise ratio (SNR) for miR-21, and *cel*-miR-54. While net signals are similar at both SDS concentrations, the noise (standard deviation of the negative control signal) is lower at 5% SDS. The high, uniform signal from the positive control spike-in also indicates that the high SDS concentration does not interfere with hybridization.

Based on these sets of experiments, an optimized lysis protocol was developed, which consisted of heating the EV sample at 60°C for 20 minutes in 5% SDS, 350 mM NaCl in TET, followed by the addition of particles, proteinase K (16 U/ml) and positive control target to start miRNA hybridization.

5.3.3 microRNA Detection

EV-miRNA detection was conducted with hydrogel microparticles, which have been used by the Doyle group for miRNA detection assays from a variety of complex samples [67, 76, 115]. Both the standard assay, outlined in Chapter 2, and rolling circle amplification (RCA), an isothermal amplification assay, were utilized for miRNA detection. RCA is a signal amplification strategy, which amplifies the signal from the each ligated linker on a miRNA-probe complex [76]. RCA was optimized to minimize background non-specific signals and enhance sensitivity for the hydrogel particle format by Dr. Dana Al-Sulaiman, a post-doc in the Doyle group. This work was done in collaboration with her. To demonstrate the ability of hydrogel particle-based detection of EV-miRNA, we sought to profile the miRNA dysregulation patterns from a EVs isolated from a lung cancer patient serum and matched healthy control serum. The isolation and quantification of the vesicles is described in the sections above.

Figure 5-8 shows a comparison of standard assay with RCA with regards to the

sensitivity and dynamic range. Calibration curves with both the standard and RCA-based assays were conducted by varying the amount of synthetic target miR-21. A standard hybridization buffer (no SDS, or proteinase K) was used for synthetic target assays. Compared to the standard assay with a limit of detection (LOD) of 1 amol, the enhanced RCA strategy offered an LOD of 2.3 zmol, representing three orders of magnitude improvement in sensitivity. This is improvement in sensitivity over previous iterations of RCA in hydrogel particles by $\sim$ 6-fold, and a considerable improvement over other multiplexed amplification techniques, such as hybridization chain reaction [**Guo2017HybridizationMicroRNAs**, 116, 147]

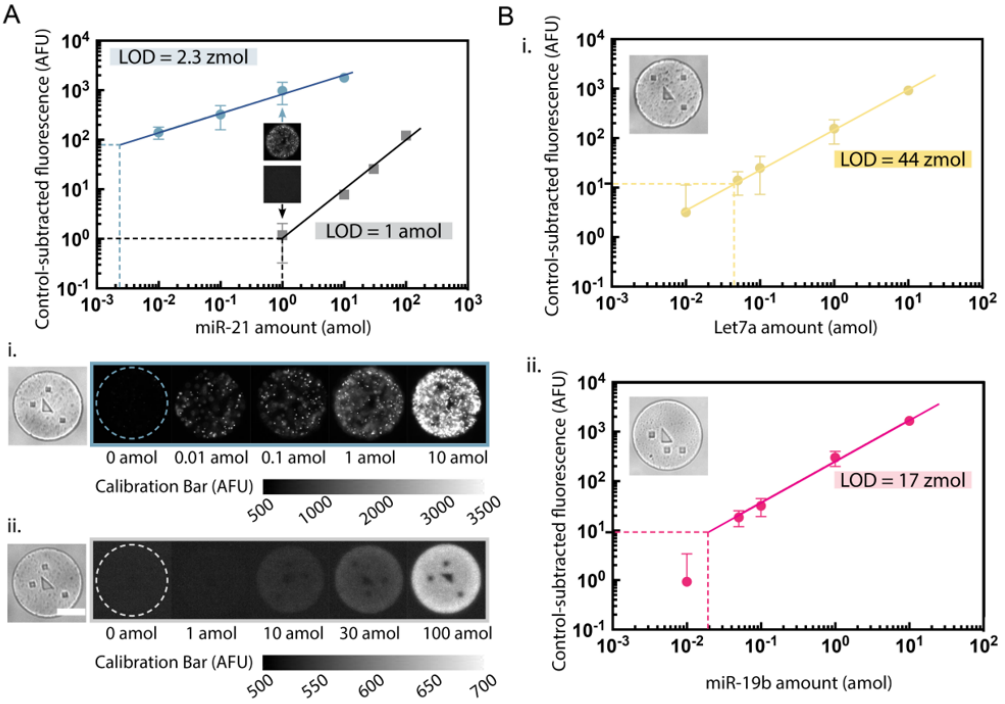

Figure 5-8: A) Calibration curve for miR-21 with standard (grey) and RCA (blue) assay. Dashed lines indicate LOD as three times standard deviation of control (0 amol) condition. Representative particles after miRNA detection with the standard (i) and RCA (ii) assay. B) RCA Calibration curves for let-7a and miR-19b. Dashed lines indicate LOD as three times standard deviation of control. Error bars throughout represent 1 standard deviation. scale bar = 50 µm).

Using the optimized lysis protocol and standard miRNA detection assay with 4x concentrated EVs, only two among five attempted miRNA targets were detectable (miR-21 and miR-19b) from both lung cancer and matched healthy patient EVs (Figure 5-9). let-7a was only detectable in healthy EVs. Moreover, all these targets are at concentrations approaching the limit of detection of the standard assay (single at-

tomole regime). To achieve the sensitivity necessary to reliably detect miRNA from 1x concentrated EVs, RCA was coupled with the lysis and hybridization protocol for EV-miRNA detection.

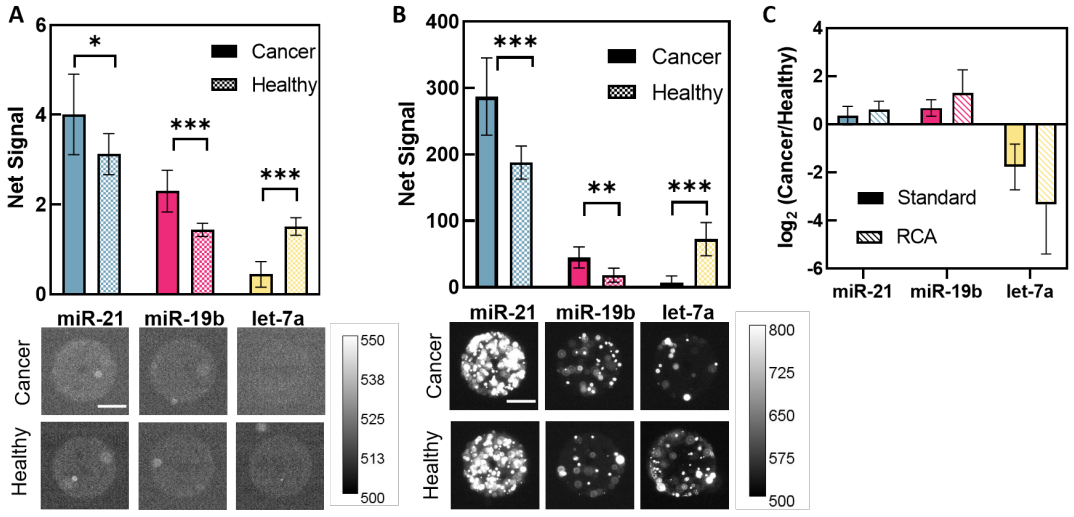

Figure 5-9: Representative particles after miRNA detection with the A) standard and B) RCA assay. 4x concentrated EVs were used for the standard assay, whereas 1x concentrated EVs were used for RCA. C) Fold change in signal between cancer and healthy EVs. Error bars throughout represent 1 standard deviation. Scale bar = 50 µm.

With higher sensitivity afforded by RCA, we were able to detect 3 miRNA (miR-21, miR-19b, let-7a) from 1x concentration EVs as shown in Figure 5-9. The miRNA profiles between the two assays are similar and show a distinct dysregulation pattern in line with literature in which both miR-21 and miR-19b are upregulated in cancer, while let-7a is downregulated and acts as a tumor supressant[3]. Moreover, the similarity in miRNA profiles between the standard assay and RCA demonstrates that RCA as an amplification strategy does not introduce biases common with other amplification strategies such as RT-PCR. [43, 45]. By combining the the absolute miRNA quantitation using the hydrogel particle platform and RCA, in conjugation with EV concentration data, we can calculate average miRNA copies per EV particle as shown in Table 5.1. Moreover, the bias and loss associated with RNA extraction is avoided completely with the direct lysis and capture protocol [130].

Table 5.1: Summary of average EV concentrations and miRNA copies for lung cancer and match healthy serum EVs.

Average EV-miRNA Copies/μL Serum		
	Cancer EV	Healthy EV
miR-21	1731.11	551.24
miR-19b	2892.26	1003.13
let-7a	1307.95	9906.31

Average miRNA Copies/EV		
	Cancer EV	Healthy EV
miR-21	9.45E-08	1.19E-08
miR-19b	1.58E-07	2.16E-08
let-7a	7.14E-08	2.13E-07

The literature on absolute miRNA quantification, particularly in exosomes and EVs is very limited. However, one study by Chevillet et al. used ddPCR to profile the most abundant miRNA from a range of samples including healthy and cancer patient plasma [113]. For these most abundant miRNA, the copy numbers ranged from $5 \times 10^4 - 2 \times 10^6$ miRNA copies/ μL plasma, and copies/EV values ranged from $10^{-5} - 10^{-3}$. Moreover, they showed that there is considerable human-to-human variation in both EV counts and miRNA copy numbers [113]. Another study into the EV-miRNA profiles in control and melanoma cancer plasma found miRNA concentrations of $\sim 9.8 \times 10^3$ copies/μL plasma for miR-19b and $\sim 1.4 \times 10^4$ copies/μL plasma for miR-21 in their control cohort (n=13 patients) based on RT-PCR with a known spiked-in synthetic target for normalization. Finally, two non-PCR based detection methods found single fM concentrations for exosomal miR-10b in healthy normal donor plasma, as measured by localized surface plasmon resonance (LSPR) and surface enhanced Raman spectroscopy (SERS), which would correspond to $\sim 1 \times 10^3$ copies/μL plasma [148, 149].

Given the differences in exosome isolation methods and miRNA detection methods, the copies numbers and copies/EV values calculated using our hydrogel platform is within the concentration ranges for EV-miRNA in literature. Plasma and serum are known to have similar miRNA concentrations, and hence the plasma-based studies are reasonable comparisons for serum EV-miRNA concentrations [14]. The data also agrees with the general trend of the low stoichiometry and low abundance of EV-associated miRNAs in plasma and serum [113]. Future studies will seek to expand the range of detectable miRNAs from a larger cohort of cancer serum

samples in order to confirm the trends presented above and serve as a reference on the concentrations and relative prevalence of EV-associated miRNAs.

5.4 Conclusions

In this study, we presented a platform for multiplexed EV-associated miRNA detection and showed how this platform can be used to determine miRNA dysregulation patterns in a pair of cancer and matched healthy serum-derived EVs. Two orthogonal methods, NTA and MRPS, were used for EV quantification, which complemented each other and provided a accurate estimate for concentration values. We then optimized the lysis procedures for direct detection of miRNAs from isolated EVs using a one-pot lysis and miRNA hybridization recipe. Finally, rolling circle amplification was utilized for ultrasensitive measurements of the EV-associated miRNA, resulting in copy number estimates in agreement with other studies in literature with absolute quantification. The RCA-based assay showed a very similar miRNA dysregulation pattern as the standard assay, demonstrating that this form of amplification does not skew the resulting amplified detection signals. This paves the way for quantitative measurements from a variety of samples expected to have low-abundance of miRNA.

Porous Functionalized Hydrogel Microparticles for Multiplexed Extracellular Vesicle Capture

In this chapter,we described the mulitplexed capture and profiling of small extracellular vesicles using graphically encoded porous hydrogel microparticles. Ultra porous hydrogels were fabricated with high molecular weight PEG porogens and characterized by diffusion studies of fluorescence nanobeads. We then characterized and optimized the thiol-acrylate Michael addition reaction for conjugation of capture antibodies into porous hydrogels. Finally, CD9 and EpCAM capture antibodies were conjugated into graphically encoded porous hydrogel particles using these optimized reaction parameters. Exosomes and small EVs from breast cancer and healthy serum were captured and profiled using the porous particles.

6.1 Introduction

Extracellular vesicles (EVs) are an emerging class of biomarkers and have been implicated in a variety of biological functions, including disease progression, drug resistance and can act as a form of inter-cellular communication [5, 11, 128]. EVs are membrane-bound vesicles released by cells and carry a variety of cargo such as proteins, mRNA, miRNA and lipids [5, 6, 9, 12]. They are found in most bodily fluids such as blood, urine, saliva, as well as in the supernatant of cultured cells [5,

33]. Small extracellular vesicles (<150 nm) include both exosomes (∼30-150 nm) and small microvesicles (100 -1000 nm) and are produced by the fusion of multivesicular bodies with the cell membrane and by outward budding of the plasma membrane respectively. As a result of these biogenesis pathways, they carry both EV-specific cargo (specifically packaged for release), as well as elements of the plasma membrane of the parent cell [9]. As such, the surface proteins found on EVs can be used for profiling, diagnostics and even further subtyping for downstream EV cargo analysis.

There exist many immunocapture-based methods for EV profiling through the use of capture antibodies specific to surface markers present on the vesicle membrane, such as tetraspanins (CD9, CD63, CD81) and disease-specific markers (EpCAM, HER2, CA125) [9, 33]. Many of these methods involve antibodies immobilized on planar surfaces (i.e. microfluidic channels, well plates), limiting antibody capture kinetics, and hence there has been a increasing emphasis on created 3D or nanostructured surfaces for EV capture [32, 37–39]. These surfaces are difficult to manufacture and scale-up. In contrast, commercial magnetic-bead based systems offer easy scale-up and fast capture kinetics through micron sized particles and rigorous mixing [12, 41]. However, there is a limited capture antibody selection and multiplexing is limited to the spectral limitations of the instrument (i.e. for flow cytometry). In this work, we demonstrate the use of ultra-porous hydrogel microparticles for multiplexed EV capture and profiling.

Hydrogel microparticles are an ideal substrate for a variety of bioassays due to their biocompatibility, solution-like kinetics, non-fouling nature, and ability to incorporate capture agents inside a 3D network [61, 62] and have previously been used for specific cell capture [150]. Graphically encoded hydrogels have previously been used for the mulitplexed detection of variety of biomarkers such as microRNA, mRNA, proteins and cytokines directly from complex samples such as live cells and cell lysate, serum, and FFPE tissue [45, 62–69]. These polyethylene glycol diacrylate (PEGDA)-based hydrogel particles are created through stop flow lithography (SFL), a technique pioneered in the Doyle Group to create 2D-extruded particles in arbitrary mask-defined shapes, useful for graphical encoding [73]. PEG-based porogens

in the prepolymer solution serve to induce polymerization-induced phase separation, creating a highly-porous 3D structure for biomarker diffusion [63, 151].

Antibody incorporation into hydrogel particles created with SFL has traditionally been done with acrylated capture antibodies. However, the low solubility of the antibody in the presence of the high photoinitiator content in the prepolymer solution creates unwanted antibody aggregation and a splotchy signal as a result [62, 69]. Recently, another method for functionalizing SFL hydrogel particles was demonstrated by the Bong group in which the leftover acrylate groups present after photopolymerization using SFL were used as handles for the post-synthesis functionalization using the thiol-acrylate Michael addition reaction [64, 69, 152]. The thiol-acrylate Michael addition "click" reaction is one of many thiol-Michael addition reactions used in materials science and a versatile tool for polymer functionalization [153]. It demonstrates high conversion in mild aqueous conditions and makes use of pendant functional groups already present in our hydrogel particles [152, 154]. Performance of the thiol-acrylate Michael addition reaction for conjugation was characterized using ^{1}H-NMR and fluorescence imaging using a model macromer, FITC-PEG-SH. Subsequently, antibodies were conjugated into hydrogel particles with the thiol-acrylate reaction using a heterobifunctional PEG linker, NHS-PEG-SH, and compared with the standard co-polymerization technique. The antibody conjugation efficiency was further optimized by tuning the antibody-to-linker ratio to maximize antibody capture function within the porous hydrogels.

EVs from breast cancer and healthy serum were captured and profiled using porous particles conjugated with CD9 and EpCAM in a multiplexed fashion with a simple overnight capture and sandwich assay workflow, similar to that used for magnetic beads [41]. Hydrogel microparticle manufacturing is scalable [73, 155] and assay workflow is similar to that of magnetic beads. Moreover, graphically encoded hydrogel particles enable multiplexing using single channel fluorescence, from a single sample, greatly simplifying, and in turn, enhancing assay workflow for EV capture and profiling studies.

6.2 Experimental

6.2.1 Antibody Reagents

For antibody conjugation optimization experiments, TSH antibody (Biospacific, Anti-TSH 5409 SPTNE-5) labelled with Dyomics DY647-P4 NHS ester. The labelling protocol is detailed in previous work [62]. The labelled antibody was stored at PBS at a stock concentration of 6 mg/ml. For antibody capture optimization experiments, the MEK1 antibody pair kit (Abcam, ab219523) was used. The capture antibody was a 1 mg/ml in PBS and was used without further purification in conjugation reactions. The lyophilized protein standard was reconstituted to 2 μg/ml in DI water and aliquots were stored frozen at -20°C. The biotinylated reporter antibody was diluted to a working concentration of 10μg/ml in 5% BSA-PBST for use in immunoassay experiments. For EV capture experiments, lyophilized antibodies from R&D Systems (anti CD9, MAB25292; anti-EpCAM, MAB9601) were purchased and reconstituted in 20 nm-filtered PBS to create 5 mg/ml stock concentrations. Reconstituted antibodies were stored at 4°C. Biotinylated CD9 antibody (Biolegend, clone HI9a) was used as the EV reporter antibody and diluted to a working concentration of 10μg/ml in 5% BSA-PBST.

6.2.2 Fabrication of Hydrogel Microparticles

PDMS microfluidic device fabrication for particle synthesis were carried out as described in Chapter 2. The hydrogel microparticles were synthesized using stop flow lithography as detailed in Chapter 2. For standard particles, the standard prepolymer formulation outlined under **40% PEG 600** in Table 6.1 below was used. For particles with the FAM-labelled DNA probes, the base prepolymer solution was combined with the acrydite modified DNA probe at a 9:1 ratio before loading into the microfluidic device. For particles with antibody co-polymerized into the particle, the base prepolymer solution was combined with the acrylated antibody in a 9:1 ratio immediately before loading into the microfluidic device. For particles with both antibody and DNA co-polymerized into the particle, the base prepolymer

solution was combined with the acrylated antibody and acrydite-modified DNA in a 9 : 0.5 : 0.5 ratio such that the concentrations in the final prepolymer solution were equivalent to those used for DNA-only or antibody-only co-polymerization.

For porous particle synthesis, the prepolymer formulation outlined under **40% PEG 2000** in Table 6.1 below was used. PEG 2000 was first dissolved in DI water (960 mg/ml) by stirring on a hot plate at 50°C until the solution was clear. Then, a prepolymer mixture comprising of 20% PEGDA 700, 50% v/v of the 960 mg/ml PEG 2000 solution, 5% Darocur 1173, and 25% PBS was loaded into the 42 μm tall PDMS channel for particle synthesis. The prepolymer mixture was thoroughly vortexed before loading to ensure that there was no macro-scale phase separation visible in the bulk solution or during SFL.

For all particles, an exposure time of 95 ms was used and particles were washed 3 times in PBST after collection from the microfluidic outlet and stored in PBST at 4°C for further use.

6.2.3 Porosity Characterization

Glass microchannel preparation for hydrogel posts was carried out as described in Chapter 2. Hydrogel posts of different composition were polymerized in glass microchannels using projection lithography as described in Chapter 2. The compositions used for generating porous hydrogels are detailed in Table 6.1 below. Note that 40% PEG 600 is the standard formulation detailed in Chapter 2 and used for miRNA assays throughout this thesis work. Higher molecular weight PEGs were incorporated into the prepolymer solution by first dissolving them in DI water while stirring on a hot plate, and then combining this concentrated PEG solution with the rest of the prepolymer components. The concentration of the higher molecular weight PEG solutions were determined such that mass of PEG added to the prepolymer would be equivalent to the mass of PEG 600 added in the standard formulation (i.e. equivalent to 40%v/v).

Table 6.1: Composition of different prepolymer solutions used for porous hydrogel synthesis. All percentages listed are on a volume per volume basis (%v/v).

40% PEG 600	**60% PEG 600**	**40% PEG 2000**	**60% PEG 2000**	**40% PEG 6000**	**60% PEG 6000**
20% PEGDA 700	20% PEGDA 700	20% PEGDA 700	20% PEGDA 700	20% PEGDA 700	20% PEGDA 700
40% PEG 600	60% PEG 600	50% of a 960 mg/ml PEG 2000 solution	75% of a 960 mg/ml PEG 2000 solution	50% of a 960 mg/ml PEG 6000 solution	75% of a 960 mg/ml PEG 6000 solution
5% Darocur 1173	5% Darocur 1173	5% Darocur 1173	5% Darocur 1173	5% Darocur 1173	5% Darocur 1173
35% DI water	15% DI water	25% DI water	–	25% DI water	–

Each prepolymer solution was combined in a 9:1 ratio with 10 mg/ml Rhodamine acrylate and thoroughly vortex-mixed before introducing into the glass microchannel. Hydrogel posts were polymerized using a 100 μm diameter circle mask with 100 ms exposure. The posts and channel were further treated with $KMnO_4$ and Pluronic F-108 as detailed in Chapter 2. At least 3 posts of each composition was polymerized in a single channel for diffusion studies.

The partitioning of fluorescent 100 nm beads (FluoSpheres F8803, Invitrogen) within the porous hydrogel posts was assessed by monitoring the diffusion of the beads through the posts under gravity flow. A pipette tip with the fluorescent bead solution (1:10 dilution of stock solution $\sim 4.5 \times 10^{12}/ml$) was loaded at the inlet of the glass microchannel and fluorescence images of the posts in the channel at various time points were acquired with an inverted microscope (Zeiss Axio Observer) equipped with a LED excitation source (X-Cite 120 LED) and appropriate filter set (Omega XF100-2). The pipette tip was refilled with beads solution periodically to maintain similar gravity flow speeds throughout the experiment.

6.2.4 Particle Functionalization using Thiol-Acrylate Michael Addition Reaction

The thiol-acrylate Michael addition reaction in the context of PEGDA hydrogel particles was characterized with ^{1}H-NMR spectroscopy of hydrolyzed microparticles and with fluorescence imaging after reaction with FITC-PEG-SH, a model thiol-bearing macromer.

^{1}H-NMR Spectroscopy

Hydrogel particles with the standard 40% PEG 600 formulation were synthesized with SFL as described, washed 3 times in PBST and then subjected to a 48 hr thiol-acrylate reaction with 30 mM mPEG$_{550}$-SH (Nanocs), and then washed again 3 times in PBST. The particles were then hydrolyzed for 24 hours with 0.1M NaOH. The hydrolyzed particle solution was diluted to 800 μL in D_2) with 0.005 wt% 3-(trimethylsilyl)propionic-2,2,3,3-d4 acid (Sigma Aldrich) and ^{1}H-NMR spectra was obtained with 128 cycles on a Bruker Avance Neo 500 MHz NMR spectrometer. As a comparison, washed particles (no thiol-acrylate reaction), and an equivalent volume of prepolymer solution were also hydrolyzed and analysed similarly. Spectra were analysed using Mnova software.

FITC-PEG-SH

A 100 mM FITC-PEG$_{1000}$-SH (Nanocs) stock solution made by dissolving the waxy solid in anhydrous DMSO. Both the solid form and the stock solution were flushed with argon gas before storage at -20°C. Hydrogel particles synthesized using SFL were conjugated with FITC-PEG-SH by combining $\sim$ 100 particles with varying concentrations of FITC-PEG-SH in 0.1 M PBST (10x PBS + 0.05% tween-20) in a 50 μL reaction volume at either 21.5°C or 37 °C. After 24 hours and 48 hours, the particles were washed 3 times with TET and imaged under a fluorescence microscope (Zeiss Axio Observer) equipped with a LED excitation source (X-Cite 120 LED) and appropriate filter set for FITC (Omega XF100-2).

6.2.5 Antibody Conjugation

Hydrogel particles synthesized using SFL were conjugated with antibodies using NHS-PEG_{2000}-SH, a heterobifunctional PEG linker. The PEG linker was dissolved in argon-purged PBST at a stock concentration of 100 mg/ml immediately before adding the appropriate amount to a mixture of hydrogel particles ($\sim$ 10 particles/μL) and antibody in argon-purged PBST with 2 mM EDTA. The argon-purged PBST in combination with the EDTA was to prevent oxidation of the thiol group and was found to increase antibody incorporation in comparison to no purging or EDTA. The conjugation reaction proceeded at 21.5°C for 24 hours on a thermoshaker. Particles were washed 3 times with TET after the conjugation reaction in order to quench any unreacted NHS ester groups.

For studies comparing the thiol-acrylate reaction with copolymerization, antibody concentration in the thiol-acrylate reaction was kept the same as the antibody concentration in the prepolymer solution for copolymerization, at 0.2 mg/ml.

For antibody copolymerization, the antibody was acrylated with NHS-PEG_{2000}-acrylate (Creative PEGWorks) using a previously developed protocol [69, 156]. Briefly, 5 mg/ml of antibody in PBS was combined with 50 mg/ml NHS-PEG-acrylate linker in a 4:1 ratio for 3 hours at room temperature (Final concentrations: 4 mg/ml antibody, 10 mg/ml linker = 5 mM). This acrylated antibody was then used without further purification for co-polymerization into the hydrogel particles as described above.

6.2.6 Porous Particle-based Immunoassay for Antibody Conjugation Optimization

Porous particles were conjugated with 0.1 mg/ml MEK1 antibody as described above. The PEG linker concentration was varied from 20-400 μg/ml (10-200 μM). Target capture was conducted with 20 ng/ml MEK1 protein standard for 30 minutes at 37°C in 50 μL PBST with 1% BSA. A no target control assay was conducted alongside at each PEG linker concentration. The particles were washed 3 times

with PBST before addition of MEK1 biotinylated reporter antibody (2 μg/ml final concentration). Reporter antibody labelled was conducted for 1 hour at 21.5°C in PBST with 1% BSA. Particles were washed 3 times to remove excess reporter antibody before labelled with SAPE (4 μg/ml final concentration)for 30 minutes at 21.5°C in PBST with 1% BSA. All of the above incubation steps were conducted on a thermoshaker with shaking at 1500 rpm to ensure adequate mixing of the particles. After 30 minutes, particles were washed 3 times with PBST before imaging under a fluorescence microscope (Zeiss Axio Observer) equipped with a LED excitation source (X-Cite 120 LED) and appropriate filter set for SAPE (Semrock) as described in Chapter 2.

6.2.7 Serum Extracellular Vesicle Purification

Extracellular vesicles (EVs) were purified from human serum (BioIVT) using PEG precipitation. Briefly, serum was thawed in a water bath at room then centrifuged at 2000g for 30 minutes and then at 10,000g for 5 minutes to clarify the serum and remove debris. The supernatant was filtered through a cell strainer and then combined with a 60% w/v PEG 6000 solution in a 5:1 ratio resulting in a final concentration of 10% (w/v) PEG 6000. The mixture was thoroughly pipette mixed until it turned cloudy white and then stored upright at 4°C for 30 minutes. The mixture was then centrifuged at 10,000g for 10 minutes at room temperature to pellet the extracellular vesicles. The supernatant was carefully removed without disturbing the pellet using a pipette tip. The pellet was resuspended in 20 nm filtered PBS (PBS filtered through a 20 nm Anotop syringe filter (Whatman)) by gentle mixing on a thermoshaker at room temperature for 30 minutes.

6.2.8 Extracellular Vesicle Capture and Labelling

Multiplexed capture and profiling of extracellular vesicles (EVs) was conducted with porous encoded hydrogel particles in which each graphical code represented a different capture antibody. 25 μL purified serum EVs were combined with capture particles ($\sim$ 25 particles per capture antibody) in PBS with 0.1% tween-20 in a

total 50 μL capture volume over a period of 18 hours at 4°C on an orbital mixer. Particles were washed 3 times with PBST the next day and the particles with captured EVS were labelled with the biotin-CD9 reporter antibody solution (2 μg/ml final concentration) in PBST with 1% BSA for 1 hour at 21.5°C. After washing the particles 3 times with PBST, the particles were labelled with SAPE (4 μg/ml final concentration) in PBST with 1% BSA for 30 minutes at 21.5°C. The EV labelling steps were conducted on a thermoshaker with shaking at 1500 rpm to ensure adequate mixing of the particles. Particles were washed 3 times with PBST before imaging under a fluorescence microscope (Zeiss Axio Observer) equipped with a LED excitation source (X-Cite 120 LED) and appropriate filter set for SAPE (Semrock) as described in Chapter 2.

6.3 Results and Discussion

6.3.1 Porous Hydrogel Fabrication

Previous work in the Doyle group had employed the use of PEG 600 as a porogen in order to increase the porosity of the particles to allow for diffusion and hybridization of full-length mRNA [63] and for miRNA assays involving enzymatic amplification [106]. This porosity inducement is based on PEGDA undergoing polymerization-induced phase separation (PIPS) in the presence of PEG porogens [63, 151, 157].

The diffusion studies using PEG 600 were based on 500 kDa FITC-dextran with an estimated radius of ∼15 nm [63]. Based on these studies, and the general size of exosomes and small EVs (30-150 nm) [5, 6], PEG 600 as a porogen would not create a sufficiently porous hydrogel for diffusion of exosomes into the network.

To increase porosity even further of hydrogel particles created using SFL, PEG 2000 and PEG 6000 were used as the pore-forming agent and compared with PEG 600. The effect of the pore-forming agent on hydrogel porosity was assessed by estimating the partition coefficient of 100 nm fluorescent beads (Fluospheres, Invitrogen) by visualizing the diffusion of the beads into the hydrogels over time. The average size of exosomes tends to be 100 nm or less [5, 139] and therefore, a 100 nm bead size was

chosen as a suitable model for assessing porosity. Hydrogel posts (mask diameter = 100 μm, height = 50 μm) made with the three different MW PEGs as porogens at either 40% or 60% concentration were polymerized inside a glass microchannel. All posts were polymerized in a single 1.5 mm width glass channel spaced out along its $\sim$ 1 cm length. using the same circular mask and the same exposure (100 ms) and UV LED settings. Rhodamine acrylate dye was included in the prepolymer solution and the rhodamine incorporation into the hydrogel post was used as a metric to assess polymerization efficiency.

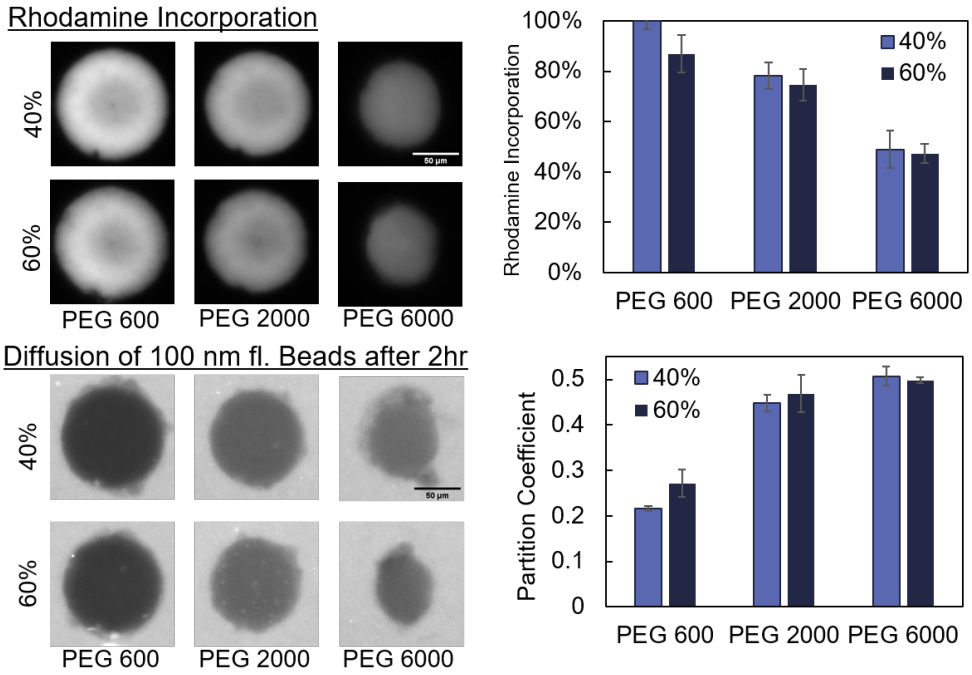

Figure 6-1: A) Rhodamine incorporation in posts polymerized with various MW PEGs as either 40% or 60% v/v. Representative images of the 40% composition posts are shown below each set of bars. B) Partition coefficients at 2 hours. Partition Coefficient = (I_{post}(2hr)-I_{post}(before flow))/($I_{background}$(2hr)-$I_{background}$(before flow)). Representative images of the 40% composition posts are shown below each set of bars. Error bars represent one standard deviation. Scale bars are 50μm

Figure 6-1 shows representative images of rhodamine signal in the posts and the partitioning of fluorescent beads after 2 hours. PEG 6000 produced under-polymerized posts, and had the lowest rhodamine incorporation. PEG 2000 produced well-formed posts with a 70% polymerization efficiency based on relative rhodamine incoporation compared to the standard 40% PEG 600, while also increasing the partition coefficient significantly ($p<0.05$ between PEG 600 and PEG 2000). Between 40%

and 60% PEG 2000, there was no significant difference in partitioning ($p>0.05$), and hence 40% PEG 2000 was chosen as the optimal porogen, due to its increased partition coefficient and relatively high polymerization efficiency, for the purpose of creating highly porous hydrogels for exosome capture.

6.3.2 Particle Functionalization using Thiol-Acrylate Michael Addition Reaction

Thiol-Acrylate Reaction Characterization in Hydrogels

In order to assess the potential of the thiol-acrylate reaction in hydrogel microparticles, the click reaction was characterized with ^{1}H-NMR spectroscopy using mPEG-SH as a model thiol-containing moiety. Hydrogels microparticles created with SFL were reacted with an access of mPEG-SH for 48 hours before hydrolyzing with NaOH for liquid NMR spectroscopy. As a baseline, an equivalent volume of prepolymer solution and an equivalent number of particles without undergoing the thiol reaction were also hydrolyzed and measured. As shown in Figure 6-2, the acrylate peaks present in the prepolymer solution and in the control particles are not visible in the particles after the thiol-acrylate reaction. Moreover, a new set of peaks corresponding to the creation of the thioether bond appear, confirming that the mPEG-SH was able to successfully react with an eliminate the acrylate pendant groups left from photopolymerization. Based on quantification of the area under the acrylate peaks in the prepolymer and control particles sample, 2.8% of the original amount of acrylates are unconverted in particles after polymerization and washing. This results in a concentration of $\sim$ 0.19 mM acrylate groups present in the hydrogel volume ($\sim$ 5 pmol per 100 μm disk-shaped particle). The concentration of thioether groups present after the thiol-acrylate reaction (run with access mPEG-SH) closely matches this value at 0.27 mM based on the thioether peaks in the spectra after the click reaction. All peak areas were normalized with the spiked in reference standard (3-(trimethylsilyl)propionic-2,2,3,3-d4 acid). The NMR data indicates that there is a large capacity for conjugation using the thiol-acrylate reaction based on the abundance of acrylate groups present in the hydrogels.

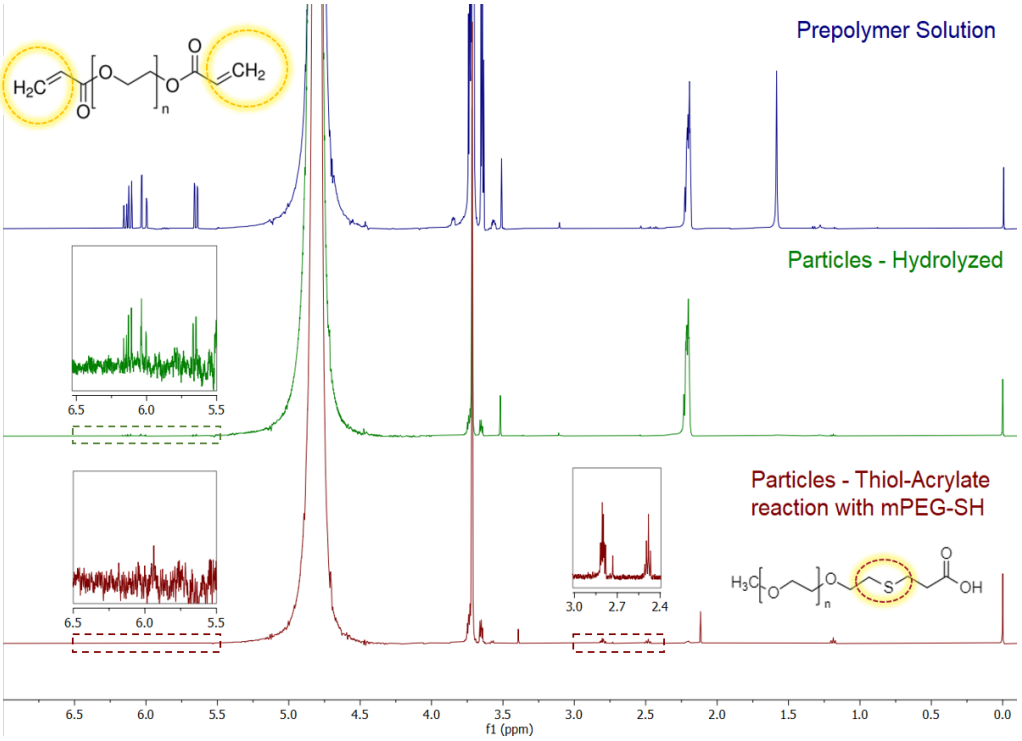

Figure 6-2: H-NMR spectra of equivalent volumes of hydrolyzed prepolymer solution (top), washed particles (middle), or particles reacted with mPEG-SH (bottom). The acrylate proton peaks appear in the 6.5-5.5 ppm range and shown in the insets for washed and thiol-reacted particles. The proton peaks corresponding to the methyl groups beside a thioether bond appear at 3.0-2.2 ppm are shown in the inset for the thiol-reacted particles.

To map out the operating space for the thiol-acrylate reaction with hydrogel particles, we used FITC-PEG-SH to monitor the reaction at various -SH concentrations at both 21.5°C and 37°C. The particles were washed and imaged after 24 and 48 hours and fluorescence images were acquired. The results of this mapping are shown in Figure 6-3. FITC-PEG incorporation increases linearly with concentration, and there is a dramatic increase in conjugation efficiency at 37°C vs. at 21. 5°C. A longer reaction time of 48 hours also increases conjugation across the concentration range tested. Finally, to demonstrate the that the FITC was covalently conjugated, the particles were washed for over 16 hours by shaking on an orbital mixture in PBST buffer after 48 hours of reaction with the FITC-PEG-SH. There was little to no decrease in FITC signal after the rigorous washing, indicating that FITC signal truly originates from covalently conjugation vs non-specific adsorption or entrapment within the hydrogel particles. Moreover the conjugation is remarkably uniform across the particle as shown in the inset fluorescence image of a particle

after reacting with 10 μM FITC-PEG-SH at 37°C for 48 hours.

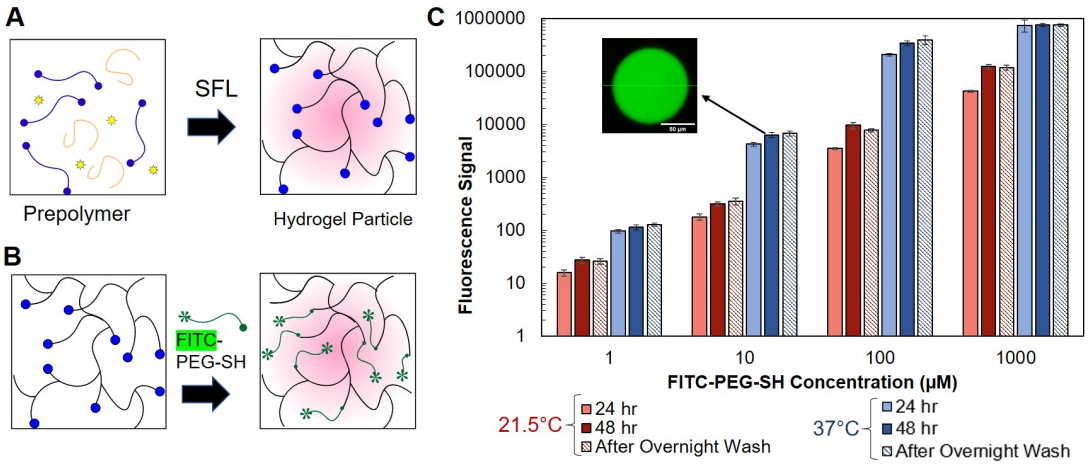

Figure 6-3: A) Schematic of the formation of pendant acrylate groups within the hydrogel after SFL. B) Schematic of conjugation of FITC-PEG-SH to pendant acrylate groups. C) Average fluorescence signal from hydrogel particles reacted with FITC-PEG-SH at various concentrations. Error bars represent 1 standard deviation. Inset fluorescence image of a particle after reacting with 10 μM FITC-PEG-SH at 37°C for 48 hours. Scale bar is 50 μm.

6.3.3 Antibody Conjugation

A model fluorescent-labelled antibody (anti-TSH labelled with DY647-P4) was used for optimizing the incorporation of antibodies using the thiol-acrylate reaction. The antibody was conjugated to either plain standard porosity particles (PEG 600-based) or standard particles with a FAM-labelled DNA probe copolymerized into the particle. A heterobifunctional PEG linker with a thiol group on one end and an NHS ester group on the other end was used to link the antibodies to the acrylate pendant groups within the hydrogel particles. The NHS ester group reacts with free amine groups present on lysine residues in the antibody and is commonly used for protein and antibody conjugation [158]. Antibody conjugation was conducted at 21.5°C since preliminary experiments showed very little improvement in conjugation at 37°C as shown in Figure 6-4. The slight difference between the two temperatures is nullified after overnight washing of the particles. Moreover, the antibody stability could be affected by performing conjugation reactions at elevated temperatures.

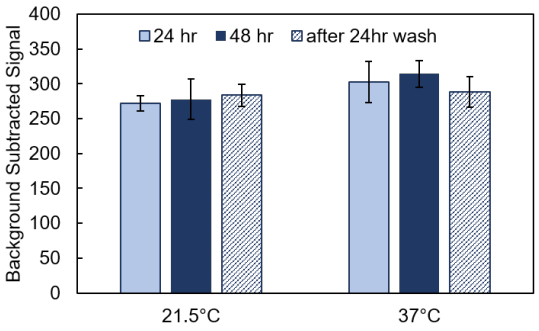

Figure 6-4: Average fluorescence signal from hydrogel particles after 24 hours or 48 hours conjugation reaction with DY647-P4 labelled anti-TSH with NHS-PEG-SH at 21.5°C and 37°C. Error bars represent 1 standard deviation.

Comparison to Co-polymerization

A schematic illustration of antibody copolymerization vs. the thiol-acrylate conjugation method is shown in figure 6-5. The conjugation efficiency of the thiol-acrylate reaction was compared with co-polymerization of the antibody as shown in figure 6-6. The concentration of the antibody in the prepolymer solution was the same as the concentration of the antibody in the thiol-acrylate reaction mixture (0.2 mg/ml) and the same concentration of PEG linker (either NHS-PEG-acrylate or NHS-PEG-SH) was used in both cases. The thiol-acrylate reaction shows a >2-fold improvement in antibody incorporation in comparison to copolymerization with an acrylated antibody. Moreover, it allows for dual-functionalization of particles by "clicking" onto particles that already contain copolymerized DNA probes, without reducing the efficiency of the DNA incorporation.

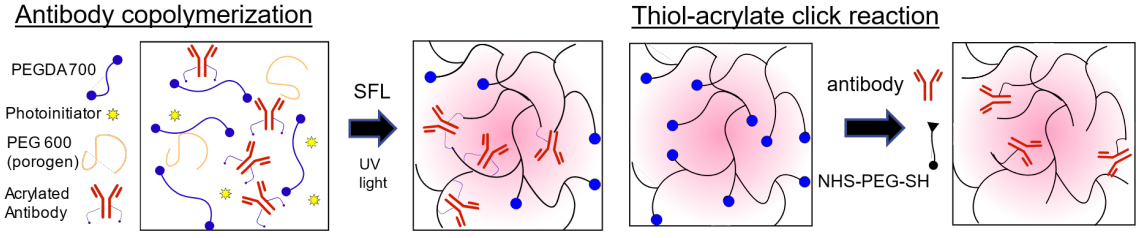

Figure 6-5: In antibody copolymerization, a prepolymer mixture containing PEGDA 700, photoinitiator, PEG porogen, and the acrylated antibody are all polymerized using SFL. In the thiol-acrylate reaction, hydrogel particles made using SFL are reacted with the antibody using the NHS-PEG-SH heterobifunctional linker.

The conjugation after 24 hours was not significantly different than after 48 hours ($p>0.05$), a trend also noticeable in preliminary data shown in figure 6-4. This is

different from the trends seen with FITC-PEG-SH and we hypothesize that this is because the NHS - amine reaction is the rate controlling step for antibody incorporation. The NHS ester is known to hydrolyze in the time span of a few hours, and ultimately dictates how much antibody is thiolated [159]. Thus, increasing the time for the thiol-acrylate reaction from 24 hours to 48 hours does not increase incorporation of the TSH antibody into the hydrogels.

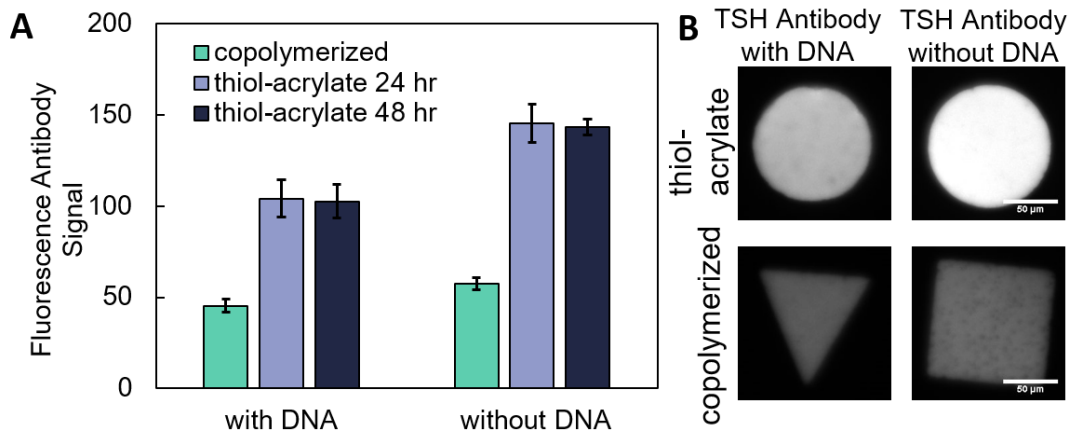

Figure 6-6: Average fluorescence signal (1% LED) of hydrogel particles after conjugation with DY647-P4 labelled anti-TSH through either copolymerization with or without FAM-labelled DNA or through thiol-acrylate reaction with NHS-PEG-SH. The thiol-acrylate reaction was conducted for 24 or 48 hours at 21.5°C using either plain particles or particles co-polymerized with FAM-labelled DNA. Error bars represent 1 standard deviation. Fluorescence images are thresholded to the same range. Scale bar is 50 μm.

Antibody to Linker Ratio Optimization

The antibody conjugation reaction was further optimized by varying the antibody-to-linker molar ratio as shown in figure 6-7. Since this is a one-pot reaction, the free NHS-PEG-SH linker competes with the thiolated antibody for acrylate groups within the particle. By decreasing the linker concentration to 50 μM (increasing the antibody-to-linker ratio from 1.3:5000 to 1.3:50), the antibody incorporation was increased by >5-fold. A lower linker concentration of 5 μM ($\sim$ 3.75 linker molecules per antibody) resulted in insufficient modification of the antibody and resulted in the lowest antibody conjugation.

A slightly higher conjugation efficiency was found with porous particles made with PEG 2000 as shown in Figure 6-8. We hypothesize this is due to particle shrinking

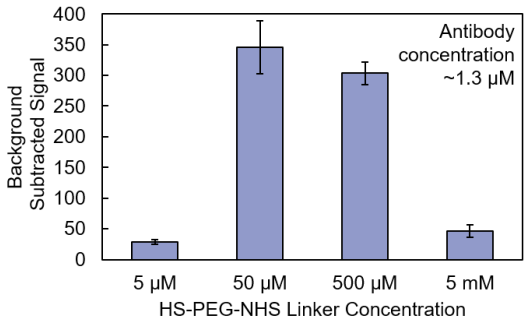

Figure 6-7: Average fluorescence signal (1% LED) of hydrogel particles after conjugation with DY647-P4 labelled anti-TSH with varying concentrations of NHS-PEG-SH linker. The thiol-acrylate reactions were conducted for 24 hours at 21.5°C using particles co-polymerized with FAM-labelled DNA. Error bars represent 1 standard deviation.

after polymerization as shown in figure 6-8, resulting in a higher average signal from the fluorescent-labelled antibody. This is evidenced by the fact that the FAM signal from the copolymerized DNA is similar even though polymerization efficiency is expected to be ∼25% less based on rhodamine acrylate incorporation data during porosity characterization experiments shown in figure 6-1. Further optimization studies were conducted with porous PEG 2000 particles.

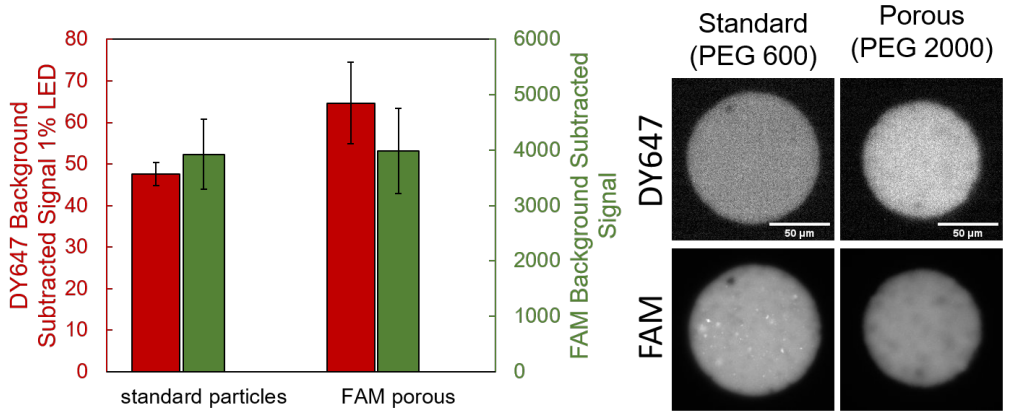

Figure 6-8: Comparison of TSH antibody conjugation with PEG 600 particles and PEG 2000 particles. The thiol-acrylate reactions were conducted for 24 hours at 21.5°C using particles co-polymerized with FAM-labelled DNA (for both PEG 600 and PEG 2000 particles). Error bars represent 1 standard deviation. Fluorescence images are thresholded to the same range. Scale bar is 50 μm.

Since the model antibody was fluorescently labelled, some of it's lysine residues were already modified by the fluorophore. Moreover, the fluorescent signal may not correspond to a functioning antibody capable of capturing it's antigen. Thus, to

further optimize the antibody-to-linker ratio for the purpose of increasing functional antibody incorporation in porous particles, unmodified MEK1 capture antibodies were conjugated into porous PEG 2000 particles at various antibody-to-linker ratios and a protein sandwich assay was performed with MEK1 antigen target and the corresponding MEK1 biotinylated reporter antibody. A short target incubation period of 30 minutes was utilized so that the corresponding signal would be dependent on capture antibody incorporation [62]. The reporter antibodies were labelled with SAPE for fluorescence imaging. Control assays with no target protein were also conducted for each linker concentration. The results are shown in figure 6-9. For a fixed antibody concentration, as the linker concentration increased, both the target signal and control (no target) signal increased accordingly. As a result, the highest net signal (target-control) and signal-to-noise ratio were achieved at the lowest linker concentration of 10 μM, corresponding to a antibody-to-linker ratio of 7.5. It is hypothesized that the control signal was a result of non-specific interactions between the reporter antibody and unquenched NHS ester groups present in the hydrogel [107]. Attempts at reducing this non-specific binding by quenching the NHS ester groups with ethanolamine or glycine buffers resulted in no improvement, and in the case of ethanolamine, caused sticky, debris-covered particles.

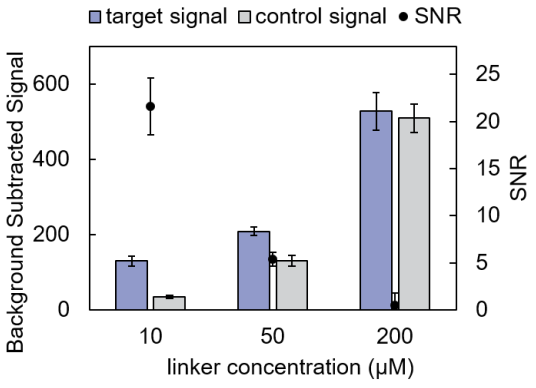

Figure 6-9: MEK1 protein sandwich assay with porous hydrogel particles conjugated with MEK1 capture antibody at different NHS-PEG-SH concentrations. MEK1 concentration during conjugation was 0.2 mg/ml $\sim$ 1.3 μM. A) Background subtracted fluorescence signal from particles incubated with target or without target (control). B) Net signal (target - control signal) and signal-to-noise ratio at various linker concentrations. Error bars represent 1 standard deviation.

6.3.4 Extracellular Vesicle Capture

In protein detection assays, the signal scales with capture probe concentration, especially with short hybridization times [62]. However, a long overnight (18 hr) capture was utilized for EVs, based on commercial bead-based methods[41]. Thus, the optimized conjugation protocol with a antibody-to-linker molar ratio of 1.3:10 ($\sim$ 7.5 linker molecules per antibody) was used to conjugate CD9 antibodies (R&D Systems) into graphically encoded porous particles at three different concentrations, 0.1 mg/ml, 0.5 mg/ml, and 1 mg/ml. CD9 is one of the tetraspanin proteins expressed on most exosomes [5, 9].

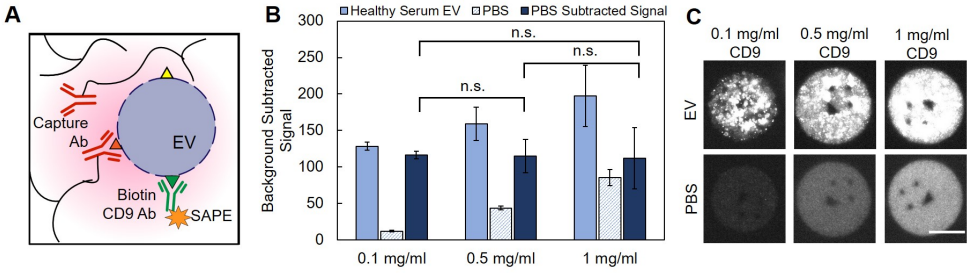

Figure 6-10: A) Schematic of EV capture using CD9 capture antibodies conjugated to hydrogel using thiol-acrylate reaction. Captured EVs are labelled with biotin-CD9 antibody followed by SAPE. B) Fluorescence signal from CD9 particles incubated with healthy serum EVs or PBS (control) for 18 hours at 4°C. Net Signal is the background subtracted fluorescence signal from EVs - background subtracted fluorescence signal from PBS. Error bars represent 1 standard deviation. No significant difference ($p>0.05$) in PBS-subtracted signal between the three antibody concentrations tested. C) Fluorescence images of particles after capture. Fluorescence images are thresholded to the same range. Scale bar is 50 μm.

Healthy serum EVs (BioIVT) isolated using PEG precipitation were captured on CD9 porous particles overnight ($\sim$ 18 hours) while mixing on an orbital mixer at 4°C. The captured EVs were then labelled with biotinylated CD9 reporter antibody (BioLegend) and SAPE as shown in figure 6-10. Particles incubated with just PBS were subject to the same labelling steps as a control. Interestingly, there was no significant difference in the net signal (EV-PBS control) between the three antibody concentrations. The control signal scaled with the higher antibody (and linker) concentration, as a result of more non-specific interactions between the capture and detection antibody and between the PEG linker and the detection antibody. It is

likely that the steric hindrance plays a large role in EV capture and hence increasing capture antibody concentration did not result in increased capture since there is limited space and mobility for EVs inside the hydrogel network.

Multiplexed Capture and Profiling of Extracellular Vesicles

To demonstrate the ability for multiplexed capture and profiling of EVs based on their surface markers, encoded porous particles conjugated with CD9 and EpCAM were used to capture EVs isolated from breast cancer and matched healthy serum (BioIVT). Particles for both CD9 and EpCAM (each with its own graphical code) were combined with the isolated EVs overnight ($\sim$ 18 hours) while mixing on an orbital mixer at 4°C. The captured EVs on both sets of particles were then labelled with biotinylated CD9 reporter antibody (BioLegend) and SAPE. Particles incubated with just PBS were subject to the same labelling steps as a control.

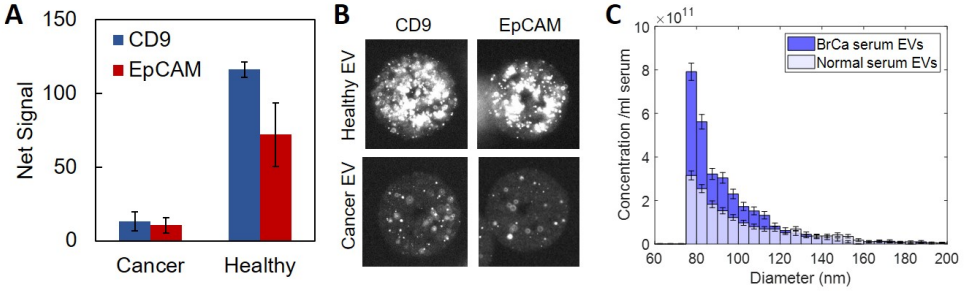

Figure 6-11: A) Net Fluorescence signal from CD9 and EpCAM particles incubated with breast cancer and healthy serum EVs for 18 hours at 4°C. Error bars represent 1 standard deviation. B) Fluorescence images of particles after capture. Fluorescence images are thresholded to the same range. Scale bar is 50 μm. C)Size distribution of EVs (1:500 dilution) isolated from matched breast cancer and healthy human serum as determined by MRPS. Thresholds are diameter>75 nm, S/N >25 and transit time<80 ms.

Figure 6-11 shows the PBS-subtracted net signal of CD9 and EpCAM for breast cancer and healthy EVs. Surprisingly the healthy EVs had a higher CD9+ and EpCAM+ concentration of EVs than the breast cancer EVs, even though the breast cancer serum had slightly higher EV concentration than the matched normal control (2.9×10^{12} vs. 1.6×10^{12} EVs/ ml serum) as measured by MRPS. This breast cancer donor had metastasis and it has been shown that circulating tumor cells from metastatic breast cancer lose EpCAM expression after epithelial-to-mesenchymal

transition [160]. Moreover, there is evidence to suggest that EpCAM is cleaved from breast cancer serum exosomes [161] and hence the low EpCAM and CD9 expression levels may be reflective of such a phenomenon.

6.4 Conclusions

In this work, we described the mulitplexed capture and profiling of small extracellular vesicles using graphically encoded porous hydrogel microparticles. We increased the porosity of the hydrogels by incorporating high molecular weight PEG porogens and then characterized the porosity with diffusion studies of 100 nm fluorescent beads. With PEG 2000 as the porogen, we achieved high porosity, with a partition coefficient of 0.45, while maintaining polymerization efficiency.

We then characterized and optimized the thiol-acrylate Michael addition reaction for conjugation of capture antibodies into porous hydrogels. The thiol-acrylate Michael addition reaction was characterized using NMR and fluorescence imaging using a model macromer, FITC-PEG-SH. Based on these findings, antibodies were conjugated into hydrogel particles with the thiol-acrylate reaction using a heterobifunctional PEG linker, NHS-PEG-SH, and compared with the standard co-polymerization technique. The click reaction resulted in a >2-fold improvement in conjugation efficiency over co-polymerization. Interestingly, increases in reaction time or temperature did not increase conjugation as they had for the model FITC-PEG-SH.

The antibody conjugation efficiency was further optimized by tuning the antibody-to-linker ratio to maximize antibody capture function within the porous hydrogels. A low linker concentration (antibody:linker ratio of 1:7.5) prevented competition between the free linker and thiolated antibody, resulting in higher incorporation, and it reduced non-specific binding during sandwich assays with a reporter antibody.

Finally, CD9 and EpCAM capture antibodies were conjugated into graphically encoded porous hydrogel particles using these optimized reaction parameters. Exosomes and small EVs from breast cancer and healthy serum were captured and

profiled using the porous particles with a simple overnight capture and sandwich assay workflow. The profiling showed increased CD9+ and EpCAM+ exosomes in the normal serum vs. the metastatic breast cancer serum, a triend that has been described in literature [160, 161]. Future studies will look into profiling EVs from a variety of samples with an expanded panel of antibody markers.

Overall, we demonstrate that porous hydrogel particles can be easily functionalized for multiplexed EV capture and profiling. With commercial magnetic beads-based methods, there is a limited antibody selection and multiplexing within the same sample is limited, resulting in larger sample requirements for EV profiling [12]. Our porous hydrogel particles can be customized with any antibody of choice and more importantly multiplexed profiling is possible from a single sample. The hydrogel particles can also be analysed using a single-channel fluorescence microscopy setup, vs. multi-laser flow cytometers necessary for commercial bead applications. Given the non-fouling nature of PEG hydrogel particles [79], we anticipate that this platform should allow for EV capture directly from complex samples like urine, serum or cell culture supernatant. Porous hydrogel particles have the potential to considerably enhance the workflow for exosome capture and profiling experiments, through multiplexing, fewer sample preparation requirements, and customizable nature, hence furthering exosome and EV studies in general.

EV Commercialization Potential and Market Analysis

7.1 Introduction

Extracellular vesicles (EVs) are small membrane-bound particles that are secreted by cells into the extracellular environment. They are an emerging class of biomarkers and have been implicated in a variety of biological functions, including disease progression, drug resistance and can act as a form of inter-cellular communication [5, 11, 128]. Recent studies have shown that exosomes and other EVs have tremendous potential in both diagnostics and therapeutics. [5, 9]. Small extracellular vesicles (<150 nm) include both exosomes (∼30-150 nm) and small microvesicles (100 -1000 nm) and are produced by the fusion of multivesicular bodies with the cell membrane and by outward budding of the plasma membrane respectively. As a result of these biogenesis pathways, they carry both EV-specific cargo (specifically packaged for release), as well as elements of the plasma membrane of the parent cell [9].

Exosomes and EVs have gained significant attention in the field of diagnostics due to their ability to carry biomolecules that reflect the physiological and pathological status of the originating cells. For example, exosomes derived from cancer cells carry specific proteins, lipids, and nucleic acids that can serve as biomarkers for early cancer detection [162]. Additionally, exosomes and EVs can be isolated from various bodily fluids, such as blood, urine, and cerebrospinal fluid, making them a

non-invasive source of diagnostic biomarkers [5, 12].

EVs have also shown great potential in the field of therapeutics due to their ability to deliver bioactive molecules to target cells. They can be engineered to carry therapeutic molecules such as small interfering RNA (siRNA), microRNA (miRNA), and a variety of drug molecules (proteins, small molecules), and can deliver these molecules to specific target cells [163]. This has significant potential in the development of novel therapies for various diseases in which precision drug delivery is required, including cancer, cardiovascular disease, and neurological disorders.

7.1.1 EV Cargo

Exosomes are thought to play a crucial role in cell-to-cell communication, as they contain a variety of bioactive molecules such as proteins, nucleic acids, and lipids, which can be transferred between cells and modulate cellular behavior. An overview of the variety of cargo that EVs carry is shown in Figure 7-1

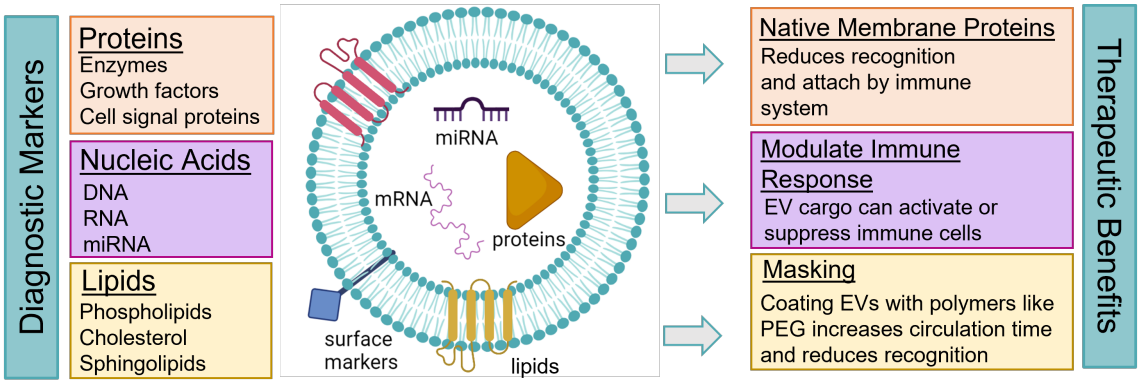

Figure 7-1: Schematic of exosome-associated cargo, which can be potential diagnostic markers and result in therapeutic benefits. Exosomes are small membraneous vesicles 30-150 nm in diameter.

EVs can carry a wide range of proteins, including enzymes, growth factors, and signaling molecules. These proteins can regulate various cellular processes and are involved in many physiological and pathological conditions [164]. For example, exosomes derived from stem cells can carry various growth factors that promote tissue repair and regeneration [165]. EVs can also carry various types of nucleic acids, such as DNA, RNA, and microRNAs (miRNAs). These molecules can modulate gene

expression and have important roles in cellular functions and diseases [166]. For example, exosomes derived from cancer cells can carry miRNAs that promote tumor growth and metastasis [35]. On the other hand, exosomes derived from mesenchymal stem cells can carry miRNAs that have anti-inflammatory and immunomodulatory effects [167]. EVs can carry various lipids, such as phospholipids, cholesterol, and sphingolipids. These lipids can modulate cellular signaling and membrane dynamics and play important roles in cellular functions and diseases [168]. For example, exosomes derived from cancer cells can carry lipids that promote tumor growth and metastasis [169].

Apart from their cargo-carrying functionality, EVs have numerous features that make them ideal as therapeutic delivery vehicles. EVs and exosomes have a natural stealth property that makes them less immunogenic than other types of therapeutic agents. This is because they are derived from cells and carry membrane proteins that are similar to those of the cells of origin. This similarity reduces the chances of recognition and attack by the immune system [170]. They can actively modulate the immune response by carrying molecules that suppress or activate immune cells. For example, exosomes derived from mesenchymal stem cells can carry molecules that suppress T cells and promote regulatory T cell differentiation, which can help to reduce inflammation and promote tissue repair [167]. Finally, EVs and exosomes can be modified to enhance their stealth properties and reduce their immunogenicity through masking techniques used by traditional nanoparticle delivery systems. These include coating EVs with polyethylene glycol (PEG) or other polymers to increase their circulation time and reduce recognition by the immune system [171]. The ability of EVs and exosomes to evade the immune response is an important advantage for their therapeutic use. This property allows them to be used as drug delivery vehicles, immune modulators, and regenerative agents without triggering adverse immune reactions.

7.2 Market Analysis

7.2.1 Market definition and Evaluation

The global EV market size was estimated to be $71 M USD in 2020 with a compound annual growth rate (CAGR) of 39% over the next five years. The overall market can be segmented by application: therapeutics, diagnostics, and research tools. Figure 7-2 presents the estimated global market size and growth rate for EVs by application. [172] Diagnostics currently represents 58% of the market and is slated to maintain it's lead and grow to 63% market share by 2023. Diagnostics field is more advanced commercially than the therapeutics segment

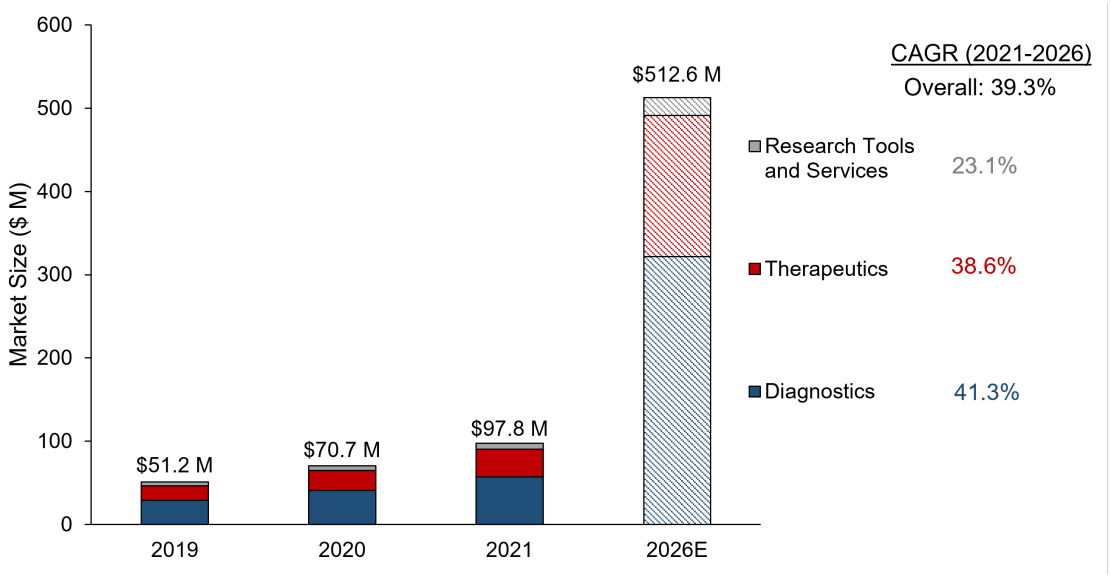

Figure 7-2: Global EV market size and growth by application.

7.2.2 Growth Drivers and Challenges

Diagnostics

The increasing prevalence of chronic diseases such as cancer, cardiovascular diseases, and neurological disorders is driving the demand for non-invasive and accurate diagnostic tools. EVs and exosomes have the potential to serve as biomarkers for early detection, diagnosis, and segmentation of these diseases, as they carry specific cargo that reflects the disease state [32]. Segmenting disease populations, allows for more

precision therapeutics to be developed, which have a higher degree of success. Thus EVs could become the next potential area for the field of companion diagnostics, however currently no large biopharma companies are publicly pursuing EV diagnostics. One of the challenges for the use of EVs and exosomes in diagnostics is the standardization and validation of assays and methods for their isolation and detection. The heterogeneity of EVs and the variability in their cargo make it challenging to establish reproducible and sensitive diagnostic assays [173]. In addition, the regulatory requirements for clinical validation and approval of EV-based diagnostic tests are not well-established, which can hinder the translation of research findings into clinical practice.

Therapeutics

The increasing demand for targeted and personalized therapies is driving the development of EV-based therapeutics. EVs and exosomes can be used as drug delivery vehicles to target specific cells and tissues, as they have natural targeting properties and can carry various cargo molecules [163]. In addition, the ability of EVs to modulate the immune response and promote tissue repair makes them attractive candidates for regenerative medicine applications [165]. One of the challenges for the use of EVs and exosomes in therapeutics is the development of scalable and reproducible methods for their production and purification. The yield and quality of EVs can be affected by various factors such as the cell source, culture conditions, and isolation methods [170] In addition, the regulatory requirements for the approval of EV-based therapeutics are not well-established, which can hinder the translation of preclinical findings into clinical trials and commercial products.

Research tools

The increasing interest in EVs and exosomes as biological mediators and biomarkers is driving the demand for research tools that can isolate, characterize, and analyze these vesicles. Various companies are developing innovative technologies for EV isolation and analysis, such as microfluidic devices, nanoparticle tracking analysis, and mass spectrometry [170]. One of the challenges for the EV research tools market

is the standardization and validation of assays and methods for EV isolation and characterization. The heterogeneity of EVs and the lack of consensus on the best practices for isolation and characterization can make it challenging to compare and interpret results from different studies [173]. Overall, the EV market is expected to grow in the coming years, driven by the increasing demand for non-invasive and personalized diagnostic and therapeutic tools. However, the market also faces challenges related to standardization, robustness, and regulatory approval, which need to be addressed to fully realize the potential of EVs in furthering the biotechnology space.

7.3 Funding Landscape

Much like the rest of the biotechnology space, the majority of EV-focused companies are funded through venture capital. From 2017 to 2022, venture capital funded 80-95% of all companies working on EVs, based on Pitchbook analysis. Other forms of funding include private equity acquisitions, acquisitions and mergers by other corporations (corporate M&A), and public markets through initial public offerings (IPO) and secondary offerings. VC funding mirrored the general biotechnology space and peaked in 2021 as a result of renewed focus from the Covid-19 pandemic and the low interest environment making risky investment decisions like venture capital more rewarding. Deal counts increased steadily from 2018-2021, with the majority of the increases being seed and early stage financing rounds as shown in Figure 7-3. This indicates that more new startups were being spun out (and funded) in this time. Total capital raised has remained fairly steady from 2017-2020. Analysis from Pitchbook shows that 2021 was an outlier year in terms of total capital raised, spurred by high valuations for late-stage startups. Even with the higher interest rates and general funding downturn in 2022, the number of deals remained fairly steady, and the total capital raised returned to pre-2021 levels. Average deal size was skewed heavily due to high valuation outliers, particularly for later stage deals, as shown in Figure 7-4. Median deal size was $0.28 M for Angel funding, $1.17 M for seed round, $5.58 M for early stage rounds, and $8.87 M for later stage rounds.

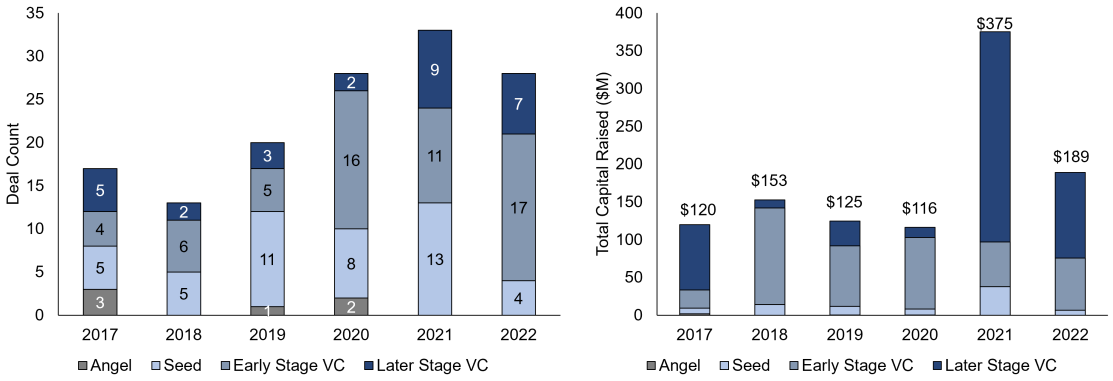

Figure 7-3: Funding Landscape for EV market. Left: Deal count by different deal type from 2017-2022. Right: Total capital raised by different deal type from 2017-2022. Angel funding is from individuals not associated with venture firms. Seed funding is typically the first institutional funding round. Early stage VC consists of Series A and B funding rounds. Later stage VC consists of Series C+. Bridge rounds were categorized based on what the prior funding round was. Not all companies disclosed deal amounts and hence were not included in total capital raised. Data from Pitchbook.

Median deal size increased 300% when moving from angel to early stage funding rounds, but only 60% when moving to later stage funding rounds.

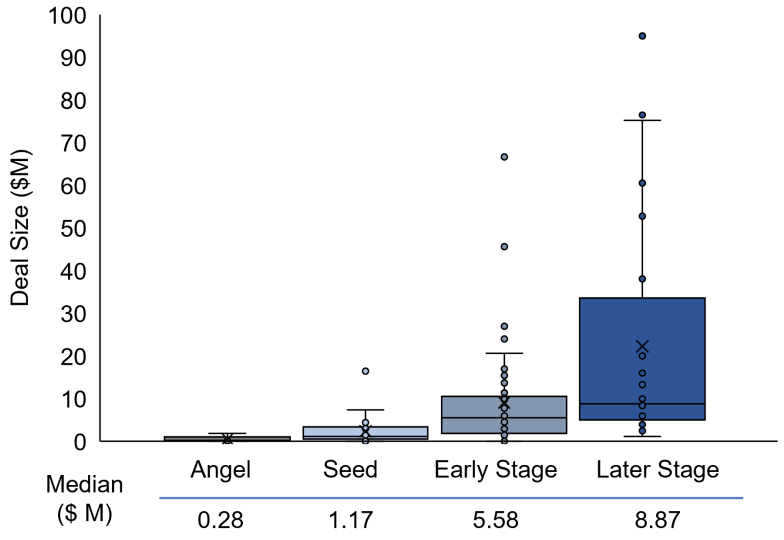

Figure 7-4: Deal size distribution by deal type. Data aggregated for deals from 2017-2022. Angel funding is from individuals not associated with venture firms. Seed funding is typically the first institutional funding round. Early stage consists of Series A and B funding rounds. Later stage consists of Series C+. Bridge rounds were categorized based on what the prior funding round was. Not all companies disclosed deal amounts and hence were not included in the distributions above. Data from Pitchbook.

7.4 Market Landscape

The overall market can be segmented by application: therapeutics, diagnostics, and research tools. Diagnostics currently represents 58% of the market and is slated to maintain it's lead and grow to 63% market share by 2023 as seen in figure 7-2. Market size is determined by revenues, and due to the long development time necessary to get therapeutics to market (as compared to diagnostics, which receive approval through the medical device or CLIA FDA pathways), the diagnostics field is more advanced commercially than the therapeutics segment. It is dominated by players using exosomes and EVs for liquid biopsy applications. Many of the startups in this segment have been acquired by larger research tools companies. For example, Exosome Diagnostics, one of the first companies to develop an FDA-approved liquid biopsy test, was acquired by Bio-Techne, a global life sciences company, in 2018. As a result, diagnostics has had the least startup capital raised, but holds the largest market share of the three segments.

The therapeutics segment, on the other hand, is more diverse. An analysis of key startups and established players in the field shows that there are more startups, with much more startup capital raised in the therapeutics space. Companies in the therapeutics segment can be categorized by their core business: novel drug discovery, drug delivery, or CDMO. A market map of key companies is shown in figure 7-5. This market map was created with data and information from Pitchbook as well as the respective company websites and press releases. As such, it focuses more on new players and startups in the space (with at least $5 M in capital raised), vs. large conglomerate companies who are now entering the space through either organic development or acquisition.

Companies involved in drug delivery focus on developing exosomes to be carriers for other types of drug classes (proteins, antibodies, antisense oligonucleotides, etc.), leveraging the high uptake of exosomes by recepient cells and immune evasion. The gene therapy companies like STRM.BIO and Carmine are a subset of these in that they specifically focus on engineering exosomes to be gene therapy vehicles. Com-

panies involved in novel drug discovery want to develop exosomes as both the active drug and the drug carrier. Many of these companies focus on exosomes from stem cell sources, thought to carry a potent mix of proteins and nucleic acids for diseases. The consumer goods-focused companies look to engineering exosomes from stem cell sources for anti-aging and other cosmetics benefits. Finally, CDMO (contract development and manufacturing organization) companies focus on building capabilities for scalable exosome manufacturing for other companies.

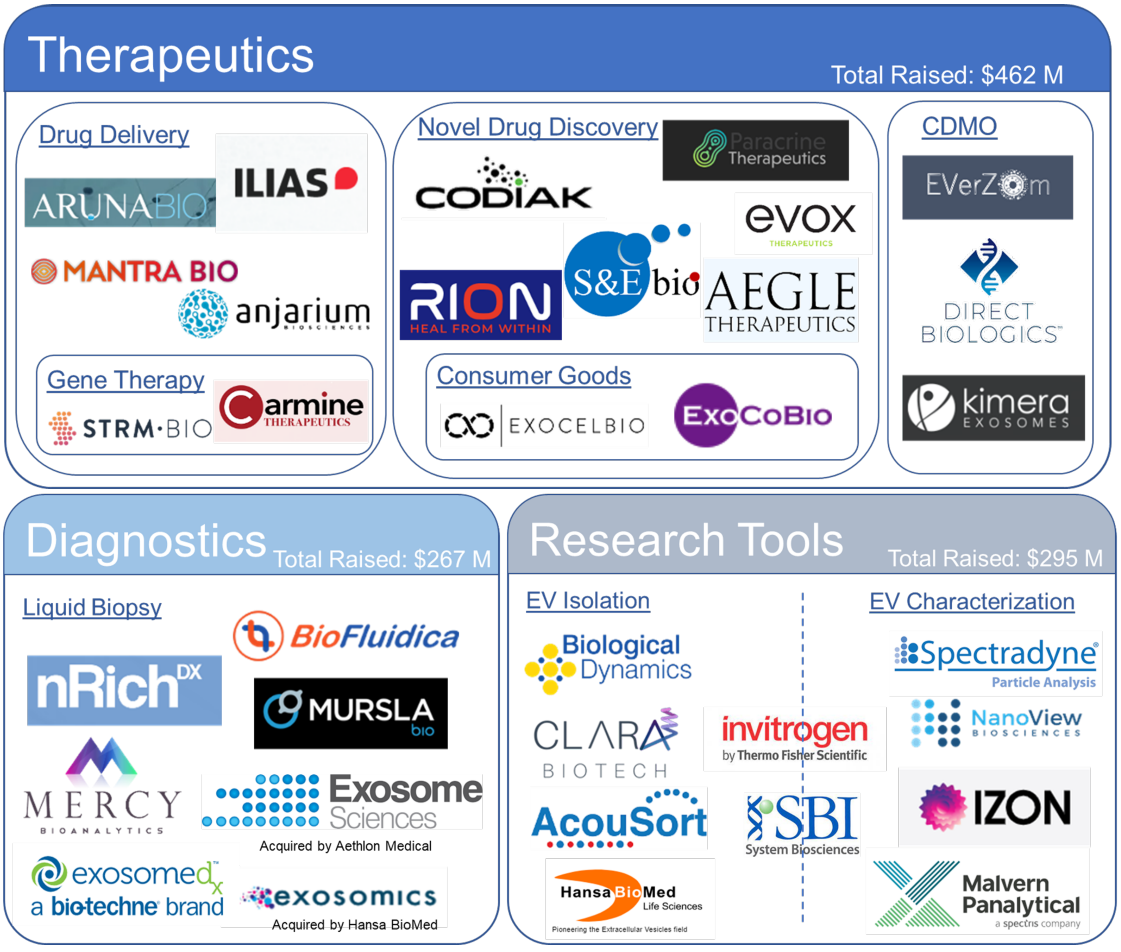

Figure 7-5: EV market map organized by application segment and core business. Created with data and information from Pitchbook as well as the respective company websites and press releases. Total capital raised only includes publicly disclosed venture capital funding.

Finally the research tools and services segment includes companies that create products for non-clinical end-use, specifically the research community. Companies either create products, instrumentation or provide services for EV isolation or for characterization. Some large, established research tools players like Invitrogen (party

of ThermoFisher) and System Biosciences provide a full ecosystem of products for both isolation and characterization. The four EV characterization companies included in the market map in figure 7-5 are all involved in size and surface marker characterization of EVs, a key challenge within the EV field. Many of the companies that provide research tools are also entering the diagnostics space as they move from non-clinical end use to clinical end-use, particularly in academic hospital centers and clinical trials.

An overview of the companies in the market map and their financial status is shown in tables below.

Company	Sub category	Total raised to date ($M)	Latest valuation/ market cap ($M)
Codiak BioSciences (NAS: CDAK)	drug discovery	N/A	278.91
STRM.BIO	gene therapy	17.18	26
Paracrine Therapeutics	drug discovery	4.54	71.92
Mantra Bio	drug delivery	39	55
Carmine Therapeutics	gene therapy	31.12	9.15
S&E Bio	drug discovery	1.44	28.09
Aruna Bio	drug delivery	33.37	N/A
Aegle Therapeutics	drug discovery	9	N/A
Anjarium Biosciences	drug delivery	60.54	104.94
Evox Therapeutics	drug discovery	155.21	254.25
EverZom	CDMO	0.95	N/A
Rion	drug discovery	5.16	N/A
ILIAS	drug delivery	37.6	N/A
ExoCoBio	consumer goods	55.3	N/A
Direct Biologics	CDMO	11.5	N/A
Exocel Bio	consumer goods	N/A	N/A
Kimera Labs	CDMO	N/A	N/A

Figure 7-6: List of EV therapeutics companies, the total venture capital raised, and latest valuation. If company is public, their ticker is listed and market cap value is used instead. If company was acquired or is part of a larger conglomerate, the parent company is noted. N/A signifies that funding details were not publicly disclosed. Data from Pitchbook.

Company	Sub-Category	total raised to date ($M)	latest valuation/ market cap ($M)
Mercy BioAnalytics	liquid biopsy	68.28	112
nRichDX	liquid biopsy	33	N/A
Mursla	liquid biopsy	5.56	19.96
BioFluidica	liquid biopsy	23.23	85
Exosomics (acquired by Lonza)	liquid biopsy	N/A	N/A
Exosome Sciences (acquired by Aethlon Medical)	liquid biopsy	N/A	8.77
Exosome Diagnostics (acquired by Bio-Techne)	liquid biopsy	137.38	576.6

Figure 7-7: List of EV diagnostics companies, the total venture capital raised, and latest valuation. If company is public, their ticker is listed and market cap value is used instead. If company was acquired or is part of a larger conglomerate, the parent company is noted. N/A signifies that funding details were not publicly disclosed. Data from Pitchbook.

Company	Sub-Category	total raised to date ($M)	latest valuation/ market cap ($M)
Biological Dynamics	EV isolation	146.25	188.5
Nanoview Biosciences	EV characterization	22.25	28
Clara Biotech	EV isolation	2.7	5.3
Izon Science	EV characterization	11.33	34.42
Acousort (STO: ACOU)	EV isolation		22.76
Malvern Pananalytical	EV characterization	113.03	222.81
HansaBioMed (part of Lonza)	EV isolation	N/A	N/A
Invitrogen (part of ThermoFisher Scientific)	EV isolation + characterization	N/A	N/A
System BioSciences	EV isolation + characterization	N/A	N/A
SpectraDyne LLC	EV characterization	1.5	N/A

Figure 7-8: List of EV research tools companies, the total venture capital raised, and latest valuation. If company is public, their ticker is listed and market cap value is used instead. If company was acquired or is part of a larger conglomerate, the parent company is noted. N/A signifies that funding details were not publicly disclosed. Data from Pitchbook.

7.4.1 Company Strategy Deep Dives

The business model and strategy were dissected for a representative company for each of the three segments, based on the value creation, capture, and isolation framework proposed by Teece.[174]

Aruna Bio

Aruna Bio is a small, privately held biotechnology company that develops engineered neural exosomes for therapeutics to be able to cross the blood-brain barrier (BBB). It's key product is the "AB126" exosome, which is an allogenic neural exosome derived from neural stem cells. Due to its neural origin, it contains surface proteins that allow it to pass the BBB. While the company is testing AB126 as a therapeutic agent in itself, its value proposition is as a payload delivery system for CNS diseases. Their pipeline targets acute diseases such as ischemic stroke (most advanced in pipeline) and traumatic brain injury, as well as chronic CNS diseases such as ALS and vascular dementia. The company creates value through partnerships with pharmaceutical and biotech companies already established in neurodegenerative diseases as well as through continued research into the stand-alone therapeutic benefits of neural exosomes. As their pipeline advances in clinical trials, the company de-risks the technology, creating value.

As with other therapeutics companies, regulatory approval is necessary to capitalize on the technology and development and market the product. However, by partnering with more established companies with more experience in regulatory approvals, Aruna improves their ability to succeed through the clinical trial and regulatory process. Other exit strategies include M&A with established companies, in which case the pipeline would be absorbed by the parent company or licensing and distribution deals to outsource those functions upon receiving regulatory approval. In order to have commercial success, particularly within the US healthcare context, the payer also needs to approve payment for the drug. The centers for Medicare and Medicaid (CMS) must approve payment for the drug in order to achieve widespread adoption since private insurance tends to follow the precedence set by CMS as was seen in the

case with Aduhelm. A strong IP strategy enables the product life to be stretched beyond its original patent life of 20 years, in particular through the exclusivity periods granted for biologics (12 years). Such an IP strategy would protect both the core technology (neural exosomes), as well as manufacturing methods, and cargo/carrier combinations developed. A summary of their business model is detailed in the value capture flowchart below.

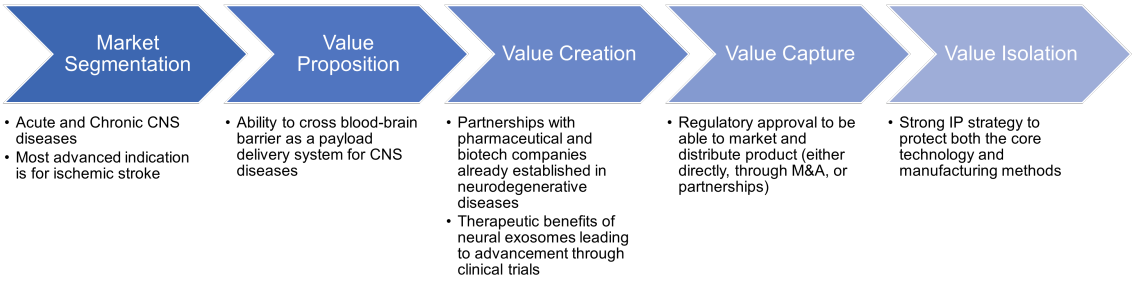

Figure 7-9: Value Capture Flowchart for Aruna Bio outlining their business model.

System Biosciences

System Biosciences (SBI) is a small, privately held biotechnology company that provides research tools (reagents, assays, services) for a variety of EV research. The company's EV research tools portfolio includes the ExoQuick Exosome Precipitation Solution, and the Exo-Fect Exosome Transfection Kit for EV cargo delivery. SBI specifically targets research segments that are emerging (exosomes, Crispr/Cas9, gene expression vectors, miRNA/incRNA) and do not have well established laboratory methods in place, or the existing methods are time or resource intensive. They develop innovative, first-to-market products that change how research is conducted, creating a new standard for research methodology. For example, their exosome isolation products were the first of their kind and would take 1-2 hours compared to existing methods that would take 10 hours, with fewer equipment requirements. Their research workforce includes a high proportion of PhD-level scientists and their products are either developed in-house or in-licensed. As such, their workforce and IP are key to their success and ability to launch new research tools. By targeting the niche emerging research segments, SBI has a high market share in those segments,

which is fueled by a high willingness to pay for their efficiency-driving products and services. Their key value proposition is that their products and services provide time-savings and consistency in research, which are highly valued in high-caliber research, particularly in emerging fields where new discoveries are made constantly.

As more researchers use their products successfully, their product lines get cited in peer-reviewed journals, creating more awareness within the community. Since the research segment is quite niche, they gain market share quickly through this "free" peer-to-peer marketing. By developing brand recognition and respectability within the field, they also increase their ability to recruit talent and in-license more technologies. Finally, once researchers switch their lab protocols to using a particular set of research tools, it takes a lot of time and work to switch to something else due to the number of validation experiments that would need to be done. The new tool would need to be cheaper, higher quality, or save even more time and resources to be pursued. Hence the nature of the industry creates a moat for the products because the barriers to switching are relatively high. SBI handles all their manufacturing in-house and distributes themselves within the US. They partner with distributors worldwide in order to provide their products to researchers outside the US. A summary of their business model is detailed in the value capture flowchart below.

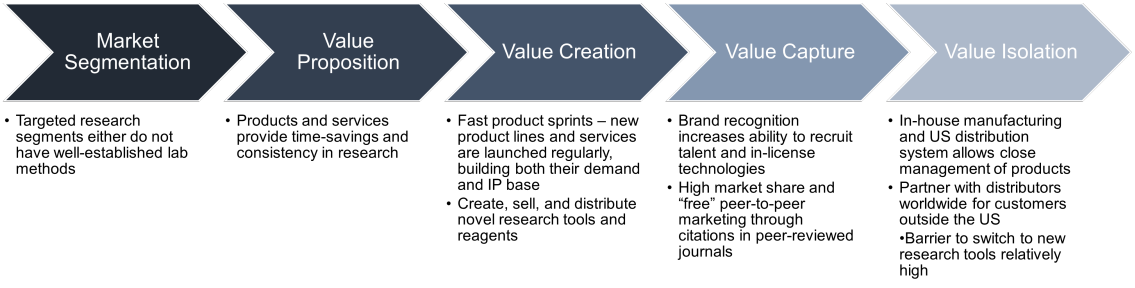

Figure 7-10: Value Capture Flowchart for System Biosciences outlining their business model.

Exosome Diagnostics

Exosome Dx is a biotechnology company that was acquired by Bio-Techne in 2018. It was the first to develop commercialize, and receive FDA approval for a liquid biopsy

test, namely the ExoDx Prostate (Intelliscore) Test, which helped assist physicians in making treatment decisions after ambiguous results from the PSA test (standard of care). Even though they have developed a large IP portfolio (>200 patents), this is still their only commercialized test.[175] Instead of commercializing more liquid biopsy tests, they have instead chosen to build out the ecosystem necessary for widespread testing adoption, using the prostate test. The test is traditionally performed at a physicians office or clinic and sent to a central processing facility to run the actual assay and diagnostics on the sample. As a result, they have put quite a bit of resources into physician outreach and marketing in order to increase the prescription of the test. They have also developed an at-home collection kit in order to collect the urine sample and ship to a central processing facility. This would increase adoption particularly during the pandemic and the emergence of telemedicine. Finally they also focus on patient outreach and marketing in order to empower the patients themselves to seek out physicians who may prescribe this test for them. This dual-pronged marketing approach targets both categories of consumers of its product. Finally, CMS approval for Medicare coverage ensures that insurance access is not a barrier for its patients. A summary of their business model is detailed in the value capture flowchart below.

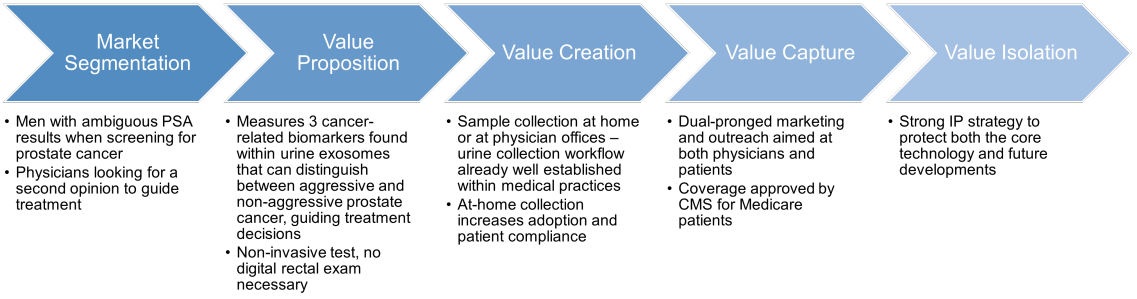

Figure 7-11: Value Capture Flowchart for Exosome Diagnostics outlining their business model.

7.5 Summary

Overall, exosomes and other EVs have shown tremendous potential in both diagnostics and therapeutics. These tiny particles can be used to detect diseases at an early stage, monitor disease progression, and deliver therapeutic molecules to target

cells. With ongoing research, exosomes and EVs could play a crucial role in the development of novel diagnostic and therapeutic approaches, potentially transforming the field of medicine. The cargo that EVs can carry is diverse and complex, and the specific cargo carried by different EV populations can vary depending on the cell type, physiological condition, and pathological state. Understanding the cargo carried by EVs is crucial for further development of diagnostic and therapeutic capabilities. The market has grown considerably over the last few years and is slated to grow considerably (39% CAGR) in the next five years. Even with the recent economic downturn and unfavorable market conditions, venture capital deal counts and sizes have continued with their pre-pandemic trends. The market landscape can be divided into three segments by application: therapeutics, diagnostics, and research tools; with sub-fields within them.

Therapeutics companies are leveraging the unique properties of EVs, including their ability to cross biological barriers and target specific cells, to develop innovative and effective therapies for various diseases. However, the regulatory landscape for EV-based therapeutics is still evolving, and obtaining regulatory approval for these therapies can be a lengthy and complex process. In addition, there are still many scientific and technical challenges to overcome, such as optimizing the production and purification of clinical-grade EVs, ensuring their safety and efficacy, and developing appropriate delivery methods.

Diagnostic-focused companies are investing heavily in research and development to improve the sensitivity, specificity, and reproducibility of their EV-based diagnostic tests. The diagnostics field is more commercially advanced than therapeutics and will likely complement and spur future growth within therapeutics through the development of companion diagnostics. Similar to therapeutics however, the regulatory landscape for EV-based diagnostics is still evolving, and obtaining regulatory approval for these tests can be a lengthy and complex process.

Finally companies focused on EV research tools are developing innovative and high-quality research tools and reagents to help scientists and researchers isolate, purify, and analyze EVs and their cargo with greater precision and accuracy. However,

the market for EV research tools is highly competitive, and companies need to continually innovate and improve their products to stay ahead of the competition. In addition, there is a growing demand for more standardized and reproducible EV isolation and analysis protocols, which presents both a challenge and an opportunity for companies in the EV research tools market. Companies with established products become the standard setters, while new technologies have an continually increasing benchmark to meet in terms of sensitivity and reproducibility. This segment also has seen the most MA activity as large life-science research companies have entered the space through acquisitions.

Conclusions and Outlook

The goal of this thesis was to develop a system to capture extracellular vesicles and profile the miRNA patterns present within them. We developed various amplification strategies in hydrogel particles for microRNA detection, including a colorimetric detection platform that could be translated to point-of-care settings. Then we developed methods for extracellular vesicle lysis and microRNA detection using a one-pot lysis and microRNA capture method. Finally, we tuned hydrogel particle porosity and use novel functionalization techniques to capture and profile extracellular vesicles based on their surface markers. In doing so, we took advantage of the various benefits of hydrogels for biomolecule detection.

8.1 Conclusions

In Chapter 3, we developed and characterized a precipitation-based colorimetric detection system that could be measured using a simple cell phone camera. This system combined the superior advantages offered by non-fouling, biocompatible hydrogel particles as a substrate for biomolecule detection assays with a robust enzymatic, colorimetric precipitation reaction. The indigo-purple NBT precipitate localized exceptionally well within the shape-encoded particles enabling multiplexing even in complex samples, while preserving the superior kinetics of solution assays. As a result, multiplexed, colorimetric detection of miRNA was possible down to sub-femtomole amounts using a simple phone camera setup.

In Chapter 4, we explored two amplification strategies to increase miRNA detection sensitivity, necessary for detection of many relevant miRNA in biologic samples like serum, urine, and extracellular vesicle fractions. The first was an enzymatic amplification strategy, utilizing the ELF-97 phosphatase substrate system, in which the cleaved product precipitates out of solution, whilst staying confined within the hydrogel matrix. The second strategy was a nucleic acid amplification approach utilizing a hairpin probe for strand displacement amplification. The optimization and proof-of-concept experiments conducted for these two amplification strategies provide the basis for further studies into them.

In Chapter 5, we described the development a platform for quantitative and multiplexed detection of extracellular vesicle-derived miRNA, via rolling circle amplification within encoded hydrogel microparticles. We showed how this platform could be used to determine miRNA dysregulation patterns in a pair of cancer and matched healthy serum-derived EVs. Two orthogonal methods, NTA and MRPS, were used for EV quantification, which complemented each other and provided a accurate estimate for concentration values. We then developed a protocol for EV lysis for the direct detection of miRNAs from isolated EVs, avoiding non-specific binding and losses associated with RNA extraction. using a one-pot lysis and miRNA hybridization recipe. Finally, rolling circle amplification was utlized for multiplexed miRNA measurements, enabling absolute quantification of EV-miRNA directly from serum EVs.

In Chapter 6, we described the mulitplexed capture and profiling of small extracellular vesicles using graphically encoded porous hydrogel microparticles. We increased the porosity of the hydrogels by incorporating PEG 2000 and then characterized the porosity with diffusion studies of 100 nm fluorescent beads. We then characterized and optimized the thiol-acrylate Michael addition reaction for conjugation of capture antibodies into porous hydrogels. The antibody conjugation efficiency was further optimized by tuning the antibody-to-linker ratio to maximize antibody capture function within the porous hydrogels, resulting in significantly higher antibody incorporation compared to conventional co-polymerization approaches. Finally, CD9

and EpCAM capture antibodies were conjugated into graphically encoded porous hydrogel particles for the capture of EVs isolated from breast cancer and healthy serum.

8.2 Future Work

8.2.1 Multiplexed Colorimetric Detection

The platform for colorimetric detection utilizes a streptavidin-conjugated enzyme for the precipitation reaction. Thus, it can replace a fluorophore like SAPE in a variety of assays to translate them from fluorescent-based to colorimetric detection. It is compatible with upstream nucleic acid amplification to improve sensitivity and is applicable to many other biomolecules of interest such as protein and cytokine detection. It could also be coupled with hydrogel motifs embedded within fibrous substrates recently developed in the group [176], and hence remove fluorescence measurement requirements, resulting in easier translation to clinical diagnostics and point-of-care applications.

8.2.2 Signal Amplification Strategies

For enzymatic precipitation-based amplification, we hypothesize that changing the relative hydrophobicity of the hydrogels, by tuning the hydrogel chemistry may result in a much lower concentration threshold to trigger precipitation. By creating a environment within the hydrogels, that is more favorable for precipitation, we could shift the equilibrium to a lower concentration threshold, ultimately lowering the limit of detection. Studies have been conducted on tuning hydrogel chemistry for the purpose of wetting applications [126], and we believe that similar concepts could be applied to tuning the hydrogel chemistry to promote faster precipitation.

For strand displacement amplification, we hypothesize that the hydrogel matrix (PEG 700 length ∼4 nm) is hindering the mobility of the long (52 nt, ∼16 nm) hairpin probe, preventing proper closing of the hairpins after hybridization. A few approaches are possible to address this limitation: the first is to conduct hybridiza-

tion at low temperatures (i.e. 37 °C), such that the chance of hairpin opening during hybridization is minimized even further. These 16 bp hairpins have $T_m \sim 80$ °C, however even the current hybridization temperature of 55°C results in a small fraction of the hairpins to open, based on NUPACK thermodynamic analysis [127]. The specificity of the system for nucleotide mismatch discrimination at lower temperatures would need to be assessed, since there is some evidence to suggest that specificity for discrimination within the let-7 family decreases with decreasing hybridization temperature [70]. Another approach would be to increase the porosity of the hydrogel such that the hairpins can fold freely. Chapter 6 describes the synthesis of ultraporous hydrogels using large molecular weight PEG porogens. Similar approaches, or the use of larger molecular weight PEGDA as the crosslinker may be used to create such hydrogels. If these limitations are addressable, SDA has the potential to drastically improve limits of detection with relatively short amplification and assay times.

8.2.3 Extracellular Vesicle miRNA Detection

In this study, we presented a platform for multiplexed EV-associated miRNA detection and showed how this platform can be used to determine miRNA dysregulation patterns in a pair of cancer and matched healthy serum-derived EVs. The RCA-based assay showed a very similar miRNA dysregulation pattern as the standard assay, demonstrating that this form of amplification does not skew the resulting amplified detection signals. The RCA signal is similar to digital assays where there is a bright spot indicating a bound miRNA. In this study we had simply used whole particle average fluorescence for quantification. However, image analysis for spot counting could be utilized and achieve even lower detection limits, and more detectable miRNA [76]. This paves the way for quantitative measurements from a variety of samples expected to have low-abundance of miRNA. Future studies will seek to expand the range of detectable miRNAs from a larger cohort of cancer serum samples in order to confirm the trends presented above and serve as a reference on the concentrations and relative prevalence of EV-associated miRNAs.

8.2.4 Extracellular Vesicle Capture from Cells

We demonstrated that porous hydrogel particles can be easily functionalized for multiplexed EV capture and profiling. Future studies will look into profiling EVs from a variety of samples with an expanded panel of antibody markers. Given the non-fouling nature of PEG hydrogel particles [79], we anticipate that this platform should allow for EV capture directly from complex samples like urine, serum or cell culture supernatant. Porous hydrogel particles have the potential to considerably enhance the workflow for exosome capture and profiling experiments, through multiplexing, fewer sample preparation requirements, and customizable nature, hence furthering exosome and EV studies in general.

Finally, the ability to synthesize dual-functional hydrogel particles was demonstrated in which particles contained both DNA probes for miRNA assays and antibodies for EV capture. The miRNA content of EVs originating from cell culture supernatant has been shown to be higher, per EV, than in biological samples like serum and urine [113, 114]. However, the concentration of EVs in cell culture is orders of magnitude lower. These porous hydrogel particles could be used with large volumes of cell culture supernatant to capture and and concentrate into the hydrogel particle. At the stoichiometry displayed in literature for cell-line derived EVs, it may be possible for the dual capture and miRNA detection of EV-miRNA directly from cell culture supernatant. Moreover, the many amplification schemes discussed, including RCA, could be utilized to achieve the sensitivity necessary.

8.3 Outlook

Throughout this thesis we took advantage of the various benefits of hydrogels for biomolecule detection, namely their biocompatibility, solution-like kinetics, non-fouling nature, and tunable chemistry. The extracellular vesicle field is still relatively nascent and much is still unknown about them. In the time of my thesis, the naming convention for exosomes changed to small EVs, the assumption that tetraspanins were specific to exosomes was refuted, and the types of cargo and data found with

EV studies has grown tremendously [9, 145]. The technologies for EV capture, quantification, and profiling are all relatively new, and there are many technological gaps to be addressed for further EV research and understanding. Hydrogels stand to provide a whole new platform for EV research, in which capture, profiling and cargo analysis could all be done on a single platform, with high efficiency and tremendous modularity and flexibility.

Appendix A

Table A.1: Nucleic Acid Sequences used in this thesis.

Name	Sequence
Colorimetric assay, standard fluorescence assay, and RCA assay probes	
Biotin probe	5'/Acryd/ATA GCA GAT CAG CAG CCA GA/Bio/3'
miR-21 probe	5'/Acryd/GAT ATA TTT TAT CAA CAT CAG TCT GAT AAG CTA/InvdT/3'
miR-221 probe	5'/Acryd/GAT ATA TTT TAG AAA CCC AGC AGA CAA TGT AGC T/InvdT/3'
miR-141 probe	5'/Acryd/GAT ATA TTT TAC CAT CTT TAC CAG ACA GTG TTA/InvdT/3'
miR-19b-3p probe	5'/Acryd/GAT ATA TTT TAT CAG TTT TGC ATG GAT TTG CAC A/InvdT/3'
miR-16-5p probe	5'/Acryd/GAT ATA TTT TAC GCC AAT ATT TAC GTG CTG CTA/InvdT/3'
let-7a probe	5'/Acryd/GAT ATA TTT TAA ACT ATA CAA CCT ACT ACC TCA/InvdT/3'
cel miR-39 probe	5'/Acryd/GAT ATA TTT TAC AAG CTG ATT TAC ACC CGG TGA/InvdT/3'
cel miR-54 probe	5'/Acryd/GAT ATA TTT TAC TCGGAT TAT GAA GAT TAC GGG TA/InvdT/3'
Universal biotinylated linker	5'/Phos/TAA AAT ATA TAA AAA AAA AAA A/Bio/3'
Colorimetric assay, standard fluorescence assay, and RCA assay targets	
miR-21 target	5'/rUrArG rCrUrU rArUrC rArGrA rCrUrG rArUrG rUrUrG rA/3'
miR-221 target	5'/rArGrC rUrArC rArUrU rGrUrC rUrGrC rUrGrG rGrUrU rUrC/3'
miR-141 target	5'/rUrArA rCrArCrU rGrUrCrU rGrGrU rArArA rGrArU rGrG/3'
miR-19b-3p target	5'/rUrGrU rGrCrA rArArU rCrCrA rUrGrC rArArA rArCrU rGrA/3'
miR-16-5p target	5'/rUrArG rCrArG rCrArC rGrUrA rArArU rArUrU rGrGrC rG/3'
let-7a target	5'/rUrGrArGrGrUrArGrUrArGrGrUrUrGrUrArUrArGrUrU/3'
cel miR-54 target	5'/rUrArCrCrCrGrArArUrCrUrUrCrArUrArArUrCrCrGrArG/3'
RCA sequences	
Universal Adapter	5'/Phos/ TAA AAT ATA TAA AAA AAA AAA ATC AGA ACA GTC TCG GAA GGA/3'
Circular Template	5'/Phos/ TAA GTC ATT CGC ACA GGA GCA ACA GAC GAG TCC TTC CGA GAC TGT TCT GA/3'
Reporter oligo 1	GCA CAG GAG CAA CAG ACG AGA AAA AA /Bio/3'
Reporter oligo 2	CGA GAC TGT TCT GAT AAG TAA AAA A /Bio/3'
RCA Probe	/5Acryd/ TAA AAT ATA TAA AAA AAA AAA ATC AGA ACA GTC TCG GAA GGA/InvdT/3'
SDA sequences	
let-7a 16bp SDA probe (in gel)	5'/Acryd/CCCAACCCACTAGTCCAACTATACAACCTACTACCTCAGGACTAGTGGGTTGGG/InvdT/3'
let-7a 16bp SDA probe (solution)	5'/FAM/CCCAACCCACTAGTCCAACTATACAACCTACTACCTCAGGACTAGTGGGTTGGG/IABkFQ/3'
let-7a 12bp SDA probe (in gel)	5'/Acryd/CCCAACCCACTAAACTATACAACCTACTACCTCATTACTAGTGGGTTGGG/InvdT/3'
let-7a 14bp SDA probe (in gel)	5'/Acryd/CCCAACCCACTAAACTATACAACCTACTACCTCACCTTTAGTGGGTTGGG/InvdT/3'
9 nt end primer	5'/CCC AAC CCA/3' *biotinylated and FAM versions have 5'/Biosg/ or 5'/FAM/
9 nt center primer	5'/AAC CCA CTA/3' *biotinylated and FAM versions have 5'/Biosg/ or 5'/FAM/
9 nt loop primer	5'/CACTAGTCC/3' *biotinylated and FAM versions have 5'/Biosg/ or 5'/FAM/
6 nt end primer	5'/CCC AAC/3'
6 nt center primer	5'/CCCACT/3'
6 nt loop primer	5'/TAGTCC/3'
12 nt end primer	5'/CCCAACCCACTA/3'
12 nt center primer	5'/CAACCCACTAGT/3'
12 nt loop primer	5'/ACCCACTAGTCC/3'

Appendix B

This appendix contains MATLAB code used for analysing data.

B.1 Shape-encoded particles analysis

This script uses the phone images taken of particles on orange background. It separates the RGB channels, thresholds to find particles, and then calculates the mean red channel value of each found object.

```
1
2  \end{}
3  close all
4  clear all
5  clc
6
7  %IMPORTING THE IMAGE--------------------------------
8
9  %Request image:
10 [filename, pathname] = ...
11      uigetfile({'*.jpg;*.tif;*.png'},'Choose Image','MultiSelect','on
           ');
12
13 I=imread([pathname filesep filename]);
14 \%figure,imshow(I),title(filechar);
```

```
15
16 %--Crop----------------
17 %Icrop=imcrop(I);
18
19 %--- split image----------------------
20 [Ired,Igreen,Iblue]=imsplit(I); \%split image into rgb channels
21
22 Iinverted=imcomplement(Ired);
23
24 %plot
25 % figure
26 % s(1)=subplot(2,2,1);imshow(I);
27 % s(2)=subplot(2,2,2); imshow(Iblue);
28 % s(3)=subplot(2,2,3); imshow(Ired);
29 % s(4)=subplot(2,2,4); imshow(Iinverted);
30 % title(s(1),'RGB image')
31 % title(s(2),'blue channel')
32 % title(s(3),'red channel')
33 % title(s(4),'red inverted')
34
35 %Threshold the image:
36 bluethresh = 160/255;
37 redthresh = 100/255;
38 bwIblue = imbinarize(Iblue,bluethresh);
39 bwIred = imbinarize(Iinverted,redthresh);
40
41 \%fill and remove all objects containing fewer than 1000 pixels:
42 bwIblue2 = imfill(bwIblue,4,'holes');
43 bwIred2 = imfill(bwIred,4,'holes');
44
45 bwIblue3 = bwareaopen(bwIblue2,1000);
```

```
46 bwIred3 = bwareaopen(bwIred2,1000);
47
48 bwI=bwIblue3+bwIred3;
49
50 bwI(bwI==2)=1; \%any overlap is set back to 1.
51
52 %find background rgb values
53 backgroundthresh=10/255;
54 background=imbinarize(Ired,backgroundthresh)-bwI;
55 bgred=regionprops(background,Ired,'MeanIntensity');
56 bgblue=regionprops(background,Iblue,'MeanIntensity');
57
58 %print to command window
59 sprintf('background blue intensity: %0.4f \n background red intensity
      : %0.4f',...
60     bgblue.MeanIntensity,bgred.MeanIntensity)
61
62 %plot
63 figure
64 d(1)=subplot(1,3,1);imshow(Iblue);
65 d(2)=subplot(1,3,2); imshow(Ired);
66 d(3)=subplot(1,3,3); imshow(bwI);
67 title(d(1),'blue channel')
68 title(d(2),'red channel')
69 title(d(3),'binary combined')
70
71 % trace boundaries
72 [boundary,labels]=bwboundaries(bwI,'noholes');
73
74 figure, imshow(I)
75 hold on
```

```
for k = 1:length(boundary)
    b=boundary{k};
    plot(b(:,2),b(:,1),'w','LineWidth',0.5)
end

%measure properties using Ired and Iblue for intensity values
measurements=regionprops('table',labels,Ired,'MeanIntensity','
   Centroid',...
    'Perimeter','Area');

measurementsblue=regionprops('table',labels,Iblue,'MeanIntensity');

objects=max(max(labels));

measurements.labelnumber=[(1:objects)'];
measurements.Circularity = (4.*pi.*measurements.Area)./(measurements.
   Perimeter).^2;
measurements.bluechannel=measurementsblue.MeanIntensity;
%measurements.shape=zeros(objects,1);

% sort objects by circularity
str={};
for i=1:objects

str{i}=sprintf('\%i',measurements.labelnumber(i));
 end

text(measurements.Centroid(:,1)+10,measurements.Centroid(:,2),str,'
   Color','w','FontSize',10);
```

B.2 Solution SDA data analysis

This script uses the csv outputs from the Applied Biosystems qPCR instrument and is used for normalizing data, performing averages, subtractions, and plotting the data. This specific script was setup for the enzyme screen shown in figure 4-7 and hence the legend entries are specific for that. However, the general form of the script can be used for any qPCR-based SDA data.

```
1
2  %Assumes comp file and melt files
3  %includes ROX reference dye
4  %no averaging, plot individual replicates
5
6  raw_comp_data=readmatrix('NJ_SDA_MB_12220_comp.csv','Range','C2:IE81'
       );
7
8  [r,c]=size(raw_comp_data);
9
10 %create Rn matrix
11 Rn_data=zeros(r/2,c);
12 for i=1:2:r
13     Rn_data((i+1)/2,:)=raw_comp_data(i,:)./raw_comp_data(i+1,:);
14    \ %FAM/ROX
15 end
16
17 %create averages for the reps
18 Rn_avg=[mean(Rn_data(1:3,:));mean(Rn_data(4:6,:));mean(Rn_data
       (9:11,:));...
19     mean(Rn_data(12:14,:));mean(Rn_data(17:19,:));mean(Rn_data
           (20:22,:));...
20     mean(Rn_data(25:27,:));mean(Rn_data(28:30,:));mean(Rn_data
           (33:35,:));mean(Rn_data(36:38,:))];
```

```
21
22 %Split data (amp reaction vs. melt curve)
23 amp_data=Rn_data(:,1:60);
24 melt_data=Rn_data(:,61:end);
25
26 Rn_avg_amp=Rn_avg(:,1:60);
27
28 % graphs with just average values
29 time=[2:2:120];
30 figure()
31 P1=plot(time,Rn_avg_amp);
32 legend('Bst3.0(NEB3.1)-T','Bst3.0(NEB3.1)-NTC','Bst3.0(ITAB2)-T','
       Bst3.0(ITAB2)-NTC',...
33     'Bst2.0-T','Bst2.0-NTC','Klenow-T','Klenow-NTC','Bst LF-T','Bst
          LF-NTC');
34 ylabel('Rn');
35 xlabel('Time (min)');
36 title('Average Rn')
37
38 figure()
39 P1=plot(Rn_avg(:,61:end)');
40 legend('Bst3.0(NEB3.1)-T','Bst3.0(NEB3.1)-NTC','Bst3.0(ITAB2)-T','
       Bst3.0(ITAB2)-NTC',...
41     'Bst2.0-T','Bst2.0-NTC','Klenow-T','Klenow-NTC','Bst LF-T','Bst
          LF-NTC');
42 ylabel('Rn');
43 \%xlabel('Time (min)');
44 title('Average Rn')
45
46 figure()
47 P2=plot(time,Rn_avg_amp([1,3,5,7,9],:));
```

```
48 legend('Bst3.0(NEB3.1)-T','Bst3.0(ITAB2)-T','Bst2.0-T','Klenow-T','
      Bst LF-T');
49 ylabel('Rn');
50 xlabel('Time (min)');
51 title('Average Rn-Target')
52
53 figure()
54 P3=plot(time,Rn_avg_amp([2,4,6,8,10],:));
55 legend('Bst3.0(NEB3.1)-NTC','Bst3.0(ITAB2)-NTC','Bst2.0-NTC','Klenow-
      NTC','Bst LF-NTC');
56 ylabel('Rn');
57 xlabel('Time (min)');
58 title('Average Rn-NTC')
59
60 figure()
61 P4=plot(time,amp_data([7,15,23,31,39],:),'-');
62 legend('Bst3.0(NEB3.1)','Bst3.0(ITAB2)','Bst2.0','Klenow','Bst LF');
63 ylabel('Rn');
64 xlabel('Time (min)');
65 title('Rn-Probe+Target Control')
66
67 figure()
68 P5=plot(time,amp_data([8,16,24,32,40],:),'--');
69 legend('Bst3.0(NEB3.1)','Bst3.0(ITAB2)','Bst2.0','Klenow','Bst LF');
70 ylabel('Rn');
71 xlabel('Time (min)');
72 title('Rn-Probe only Control')
73
74 % repeat above set of graphs but with individual replicates graphed
75 time=[2:2:120];
76 figure()\%with target
```

```
77
78 M1=plot(time,amp_data(1:3,:),'Color','#0072BD');
79 hold on
80 M2=plot(time,amp_data(9:11,:),'Color','#D95319');
81 M3=plot(time,amp_data(17:19,:),'Color','#EDB120');
82 M4=plot(time,amp_data(25:27,:),'Color','#7E2F8E');
83 M5=plot(time,amp_data(33:35,:),'Color','#77AC30');
84 hold off
85 legend([M1(1),M2(1),M3(1),M4(1),M5(1)],'Bst3.0(NEB3.1)','Bst3.0(ITAB2
       )','Bst2.0','Klenow','Bst LF');
86 ylabel('Rn');
87 xlabel('Time (min)');
88 title('Indivdual Replicates Rn-Target')
89
90 figure()%NTC
91 M1=plot(time,amp_data(4:6,:),'Color','#0072BD');
92 hold on
93 M2=plot(time,amp_data(12:14,:),'Color','#D95319');
94 M3=plot(time,amp_data(20:22,:),'Color','#EDB120');
95 M4=plot(time,amp_data(28:30,:),'Color','#7E2F8E');
96 M5=plot(time,amp_data(36:38,:),'Color','#77AC30');
97 hold off
98 legend([M1(1),M2(1),M3(1),M4(1),M5(1)],'Bst3.0(NEB3.1)','Bst3.0(ITAB2
       )-T','Bst2.0','Klenow','Bst LF');
99 ylabel('Rn');
100 xlabel('Time (min)');
101 title('Indivdual Replicates Rn-NTC')
102
103 %%
104 %subtract controls
105 %1=Bst 3.0, NEB 3.1; 2 = Bst 3.0, ITAB2, 3=Bst 2.0, 4=Klenow, 5=Bst
```

```
   LF
106
107 T1=amp_data(1:3,:)-amp_data(7,:);
108 T2=amp_data(9:11,:)-amp_data(15,:);
109 T3=amp_data(17:19,:)-amp_data(23,:);
110 T4=amp_data(25:27,:)-amp_data(31,:);
111 T5=amp_data(33:35,:)-amp_data(39,:);
112
113 N1=amp_data(4:6,:)-amp_data(8,:);
114 N2=amp_data(12:14,:)-amp_data(16,:);
115 N3=amp_data(20:22,:)-amp_data(24,:);
116 N4=amp_data(28:30,:)-amp_data(32,:);
117 N5=amp_data(36:38,:)-amp_data(40,:);
118
119 figure()
120 M1=plot(time,T1,'Color','#0072BD');
121 hold on
122 M2=plot(time,T2,'Color','#D95319');
123 M3=plot(time,T3,'Color','#EDB120');
124 M4=plot(time,T4,'Color','#7E2F8E');
125 M5=plot(time,T5,'Color','#77AC30');
126 hold off
127 legend([M1(1),M2(1),M3(1),M4(1),M5(1)],'Bst3.0(NEB3.1)','Bst3.0(ITAB2
   )','Bst2.0','Klenow','Bst LF');
128 ylabel('Rn - Control Subtracted');
129 xlabel('Time (min)');
130 title('Indivdual Replicates Rn (Control Subtracted) - Target')
131 axis([0 120 -0.5 1])
132 figure()
133 M1=plot(time,N1,'Color','#0072BD');
134 hold on
```

```
M2=plot(time,N2,'Color','#D95319');
M3=plot(time,N3,'Color','#EDB120');
M4=plot(time,N4,'Color','#7E2F8E');
M5=plot(time,N5,'Color','#77AC30');
hold off
legend([M1(1),M2(1),M3(1),M4(1),M5(1)],'Bst3.0(NEB3.1)','Bst3.0(ITAB2
    )','Bst2.0','Klenow','Bst LF');
ylabel('Rn - Control Subtracted');
xlabel('Time (min)');
title('Indivdual Replicates Rn (Control Subtracted) - NTC')
axis([0 120 -0.5 1])

%% normalized (subtracted 1st value from each indivdual curve

figure()
M1=plot(time,T2-T2(:,1),'Color','#0072BD');
hold on
M2=plot(time,T3-T3(:,1),'Color','#D95319');
M3=plot(time,T5-T5(:,1),'Color','#EDB120');
M4=plot(time,T4-T4(:,1),'Color','#7E2F8E');
hold off
legend([M1(1),M2(1),M3(1),M4(1)],'Bst3.0','Bst2.0','Bst LF','Klenow',
    'FontSize',12);
ylabel('Normalized Fluorescence','FontSize',14);
xlabel('Time (min)','FontSize',14);
axis([0 120 0 1])

%% averaged and normalized (subtracted 1st value from each indivdual
    curve and then averaged
T=[mean(T1-T1(:,1));mean(T2-T2(:,1));mean(T3-T3(:,1));mean(T4-T4(:,1)
    );mean(T5-T5(:,1))];
```

```
N=[mean(N1-N1(:,1));mean(N2-N2(:,1));mean(N3-N3(:,1));mean(N4-N4(:,1)
    );mean(N5-N5(:,1))];

figure()
plot(time,T)
legend('Bst3.0(NEB3.1)','Bst3.0(ITAB2)','Bst2.0','Klenow','Bst LF');
ylabel('Delta Rn - Control Subtracted');
xlabel('Time (min)');
title('Average Rn (Control Subtracted and Normalized) - Target')
axis([0 120 -0.01 1])
figure()
plot(time,N)
hold off
legend('Bst3.0(NEB3.1)','Bst3.0(ITAB2)','Bst2.0','Klenow','Bst LF');
ylabel('Delta Rn - Control Subtracted');
xlabel('Time (min)');
title('Average Rn (Control Subtracted and Normalized) - NTC')
axis([0 120 -0.01 1])

%%
%melt curves
%only plotting averages for reps

temp_melt_data=readmatrix('NJ_SDA_MB_12220_diss.xlsx','Range','B3:
    FK42');
F_melt_data=readmatrix('NJ_SDA_MB_12220_diss.xlsx','Range','B44:FK83'
    );
deriv_melt_data=readmatrix('NJ_SDA_MB_12220_diss.xlsx','Range','B85:
    FK124');

%create averages for the reps
```

```
melt_avg=[mean(F_melt_data(1:3,:));mean(F_melt_data(4:6,:));mean(
    F_melt_data(9:11,:));...
     mean(F_melt_data(12:14,:));mean(F_melt_data(17:19,:));mean(
         F_melt_data(20:22,:));...
     mean(F_melt_data(25:27,:));mean(F_melt_data(28:30,:));mean(
         F_melt_data(33:35,:));mean(F_melt_data(36:38,:))];

%%
figure()
plot(temp_melt_data([1,9,17,25,33],:)',melt_avg([1,3,5,7,9],:)');
legend('Bst3.0(NEB3.1)','Bst3.0(ITAB2)','Bst2.0','Klenow','Bst LF','
    Location','Northwest');
ylabel('Relative Fluorescence (FAM/ROX)');
xlabel('Temperature');
title('Average Dissociation Curve-Target')

figure()
plot(temp_melt_data([4,12,20,28,36],:)',melt_avg([2,4,6,8,10],:)');
legend('Bst3.0(NEB3.1)','Bst3.0(ITAB2)','Bst2.0','Klenow','Bst LF','
    Location','Northwest');
ylabel('Relative Fluorescence (FAM/ROX)');
xlabel('Temperature');
title('Average Dissociation Curve-NTC')

figure()
plot(temp_melt_data([7,15,23,31,39],:)',F_melt_data
    ([7,15,23,31,39],:)');
legend('Bst3.0(NEB3.1)','Bst3.0(ITAB2)','Bst2.0','Klenow','Bst LF','
    Location','Northwest');
ylabel('Relative Fluorescence (FAM/ROX)');
xlabel('Temperature');
```

```
213 title('Dissociation Curve-Probe+Target Control')
214
215 figure()
216 plot(temp_melt_data([8,16,24,32,40],:)',F_melt_data
       ([8,16,24,32,40],:)');
217 legend('Bst3.0(NEB3.1)','Bst3.0(ITAB2)','Bst2.0','Klenow','Bst LF','
       Location','Northwest');
218 ylabel('Relative Fluorescence (FAM/ROX)');
219 xlabel('Temperature');
220 title('Dissociation Curve-Probe only Control')
221
222 %% 1st rep only
223 figure()
224 plot(temp_melt_data([1,9,17,25,33],:)',F_melt_data([1,9,17,25,33],:)
       ');
225 legend('Bst3.0(NEB3.1)','Bst3.0(ITAB2)','Bst2.0','Klenow','Bst LF','
       Location','Northwest');
226 ylabel('Relative Fluorescence (FAM/ROX)');
227 xlabel('Temperature');
228 title('Dissociation Curve-Target')
229
230 figure()
231 plot(temp_melt_data([4,12,20,28,36],:)',F_melt_data
       ([4,12,20,28,36],:)');
232 legend('Bst3.0(NEB3.1)','Bst3.0(ITAB2)','Bst2.0','Klenow','Bst LF','
       Location','Northwest');
233 ylabel('Relative Fluorescence (FAM/ROX)');
234 xlabel('Temperature');
235 title('Dissociation Curve-NTC')
236 %% DERIVATIVES
237 % first replicate only
```

```
%flip all the data (negative derivative)
negderiv_melt_data=-deriv_melt_data;

figure()
plot(temp_melt_data([1,9,17,25,33],:)',negderiv_melt_data
    ([1,9,17,25,33],:)');
legend('Bst3.0(NEB3.1)','Bst3.0(ITAB2)','Bst2.0','Klenow','Bst LF','
    Location','Northwest');
ylabel('dF/dT');
xlabel('Temperature');
title('Average Dissociation Curve-Target')
axis([35 90 -0.05 0.15])

figure()
plot(temp_melt_data([4,12,20,28,36],:)',negderiv_melt_data
    ([4,12,20,28,36],:)');
legend('Bst3.0(NEB3.1)','Bst3.0(ITAB2)','Bst2.0','Klenow','Bst LF','
    Location','Northwest');
ylabel('dF/dT');
xlabel('Temperature');
title('Average Dissociation Curve-NTC')
axis([35 90 -0.05 0.15])

figure()
plot(temp_melt_data([7,15,23,31,39],:)',negderiv_melt_data
    ([7,15,23,31,39],:)');
legend('Bst3.0(NEB3.1)','Bst3.0(ITAB2)','Bst2.0','Klenow','Bst LF','
    Location','Northwest');
ylabel('dF/dT');
xlabel('Temperature');
title('Dissociation Curve-Probe+Target Control')
```

```
axis([35 90 -0.05 0.15])

figure()
plot(temp_melt_data([8,16,24,32,40],:)',negderiv_melt_data
   ([8,16,24,32,40],:)');
legend('Bst3.0(NEB3.1)','Bst3.0(ITAB2)','Bst2.0','Klenow','Bst LF','
   Location','Northwest');
ylabel('dF/dT');
xlabel('Temperature');
title('Dissociation Curve-Probe only Control')
axis([35 90 -0.05 0.15])
%%
% plot Klenow set

figure()
P=plot(temp_melt_data([25,28,31,32],:)',negderiv_melt_data
   ([25,28,31,32],:)');
legend('Target','NTC','No amp control - Target','No amp control - NTC
   ','Location','Northwest');
P(1).Color='b';
P(2).Color='r';
P(3).Color='b';P(3).LineStyle='--';
P(4).Color='r';P(4).LineStyle='--';
ylabel('dF/dT');
xlabel('Temperature');
title('Dissociation Curve-Klenow (exo-) Polymerase')
axis([35 90 -0.02 0.14])

figure()
f=plot(temp_melt_data([25,28,31,32],:)',F_melt_data([25,28,31,32],:)
   ');
```

```
legend('Target','NTC','No amp control — Target','No amp control — NTC
    ','Location','Northwest');
f(1).Color='b';
f(2).Color='r';
f(3).Color='b';f(3).LineStyle='——';
f(4).Color='r';f(4).LineStyle='——';
ylabel('Fluorescence');
xlabel('Temperature');
title('Dissociation Curve—Klenow (exo—) Polymerase')
```

Bibliography

[1] Rebecca L. Siegel, Kimberly D. Miller, and Ahmedin Jemal. "Cancer statistics, 2018". In: *CA: A Cancer Journal for Clinicians* 68.1 (Jan. 2018), pp. 7–30. ISSN: 00079235. DOI: 10.3322/caac.21442. URL: http://doi.wiley.com/10.3322/caac.21442.

[2] Irene Vanni et al. "Exosomes: a new horizon in lung cancer". In: *Drug Discovery Today* 22.6 (June 2017), pp. 927–936. ISSN: 1359-6446. DOI: 10.1016/J.DRUDIS.2017.03.004. URL: https://www.sciencedirect.com/science/article/pii/S1359644617301150.

[3] Sabrina Müller et al. "Circulating MicroRNAs as Potential Biomarkers for Lung Cancer". In: *Tumor Liquid Biopsies. Recent results in cancer research.* Vol. 215. NLM (Medline), 2019, pp. 299–318. DOI: 10.1007/978-3-030-26439-0{_}16.

[4] Gareth J. Morrison and Amir Goldkorn. "Development and Application of Liquid Biopsies in Metastatic Prostate Cancer". In: *Current Oncology Reports* 20.4 (Apr. 2018), p. 35. ISSN: 1523-3790. DOI: 10.1007/s11912-018-0683-0. URL: http://link.springer.com/10.1007/s11912-018-0683-0.

[5] Raghu Kalluri and Valerie S. LeBleu. "The biology, function, and biomedical applications of exosomes". In: *Science* 367.6478 (Feb. 2020), eaau6977. ISSN: 10959203. DOI: 10.1126/science.aau6977. URL: https://www.sciencemag.org/lookup/doi/10.1126/science.aau6977.

[6] Ji Hye Jung, Xuebin Fu, and Phillip C. Yang. *Exosomes Generated from iPSC-Derivatives: New Direction for Stem Cell Therapy in Human Heart Diseases*. Jan. 2017. DOI: 10.1161/CIRCRESAHA.116.309307. URL: http://circres.ahajournals.org.

[7] Pin Li et al. "Progress in Exosome Isolation Techniques." In: *Theranostics* 7.3 (2017), pp. 789–804. ISSN: 1838-7640. DOI: 10.7150/thno.18133. URL: http://www.ncbi.nlm.nih.gov/pubmed/28255367%20http://www.pubmedcentral.nih.gov/articlerender.fcgi?artid=PMC5327650.

[8] Simone Anfossi et al. "Clinical utility of circulating non-coding RNAs — an update". In: *Nature Reviews Clinical Oncology* 15.9 (Sept. 2018), pp. 541–563. ISSN: 1759-4774. DOI: 10.1038/s41571-018-0035-x. URL: http://www.nature.com/articles/s41571-018-0035-x.

[9] Carine Z. J. Lim et al. "New Sensors for Extracellular Vesicles: Insights on Constituent and Associated Biomarkers". In: *ACS Sensors* 5.1 (Jan. 2020), pp. 4–12. ISSN: 2379-3694. DOI: 10.1021/acssensors.9b02165. URL: https://pubs.acs.org/doi/10.1021/acssensors.9b02165.

[10] Antonios Chronopoulos, Tyler J Lieberthal, and Armando E del Río Hernández. "Exosomes as a platform for 'liquid biopsy' in pancreatic cancer". In: *Convergent Science Physical Oncology* 3.1 (Feb. 2017), p. 013005. ISSN: 2057-1739. DOI: 10.1088/2057-1739/aa5beb. URL: http://stacks.iop.org/2057-1739/3/i=1/a=013005?key=crossref.abaf7dead9f7ca3bdde2abfdcd34eb49.

[11] Graça Raposo and Willem Stoorvogel. *Extracellular vesicles: Exosomes, microvesicles, and friends*. Feb. 2013. DOI: 10.1083/jcb.201211138.

[12] Dongbin Yang et al. "Progress, opportunity, and perspective on exosome isolation - Efforts for efficient exosome-based theranostics". In: *Theranostics* 10.8 (2020), pp. 3684–3707. ISSN: 18387640. DOI: 10.7150/thno.41580.

[13] Jun Lu et al. “MicroRNA expression profiles classify human cancers”. In: *Nature* 435.7043 (June 2005), pp. 834–838. ISSN: 00280836. DOI: 10.1038/nature03702. URL: https://www.nature.com/articles/nature03702.

[14] Patrick S Mitchell et al. “Circulating microRNAs as stable blood-based markers for cancer detection.” In: *Proceedings of the National Academy of Sciences of the United States of America* 105.30 (July 2008), pp. 10513–8. ISSN: 1091-6490. DOI: 10.1073/pnas.0804549105. URL: http://www.ncbi.nlm.nih.gov/pubmed/18663219%20http://www.pubmedcentral.nih.gov/articlerender.fcgi?artid=PMC2492472.

[15] Tugba Kilic et al. *microRNA biosensors: Opportunities and challenges among conventional and commercially available techniques*. Jan. 2018. DOI: 10.1016/j.bios.2017.08.007.

[16] Ioana Berindan-Neagoe et al. “MicroRNAome genome: A treasure for cancer diagnosis and therapy”. In: *CA: A Cancer Journal for Clinicians* 64.5 (Sept. 2014), pp. 311–336. ISSN: 1542-4863. DOI: 10.3322/caac.21244.

[17] Bianca C. Bernardo et al. *A MicroRNA Guide for Clinicians and Basic Scientists: Background and Experimental Techniques*. Mar. 2012. DOI: 10.1016/j.hlc.2011.11.002.

[18] Jason D. Arroyo et al. “Argonaute2 complexes carry a population of circulating microRNAs independent of vesicles in human plasma”. In: *Proceedings of the National Academy of Sciences* 108.12 (Mar. 2011), pp. 5003–5008. ISSN: 0027-8424. DOI: 10.1073/PNAS.1019055108. URL: https://www.pnas.org/content/108/12/5003%20https://www.pnas.org/content/108/12/5003.abstract.

[19] Gitte Brinch Andersen and Jörg Tost. “Circulating miRNAs as Biomarker in Cancer”. In: *Recent results in cancer research. Fortschritte der Krebsforschung. Progres dans les recherches sur le cancer* 215 (2020), pp. 277–298. ISSN: 00800015. DOI: 10.1007/978-3-030-26439-0{_}15.

[20] Jie Chen, Chengping Hu, and Pinhua Pan. "Extracellular vesicle microRNA transfer in lung diseases". In: *Frontiers in Physiology* 8.DEC (Dec. 2017), p. 1028. ISSN: 1664042X. DOI: 10.3389/fphys.2017.01028.

[21] Oscar D. Murillo et al. "exRNA Atlas Analysis Reveals Distinct Extracellular RNA Cargo Types and Their Carriers Present across Human Biofluids". In: *Cell* 177.2 (Apr. 2019), pp. 463–477. ISSN: 10974172. DOI: 10.1016/j.cell.2019.02.018.

[22] George A. Calin and Carlo M. Croce. "MicroRNA signatures in human cancers". In: *Nature Reviews Cancer* 6.11 (Nov. 2006), pp. 857–866. ISSN: 1474175X. DOI: 10.1038/nrc1997.

[23] Hong-Lin Cheng et al. "Detecting miRNA biomarkers from extracellular vesicles for cardiovascular disease with a microfluidic system". In: *Lab on a Chip* 18.19 (2018), pp. 2917–2925. ISSN: 1473-0197. DOI: 10.1039/C8LC00386F. URL: http://xlink.rsc.org/?DOI=C8LC00386F.

[24] Franco Grimolizzi et al. "Exosomal miR-126 as a circulating biomarker in non-small-cell lung cancer regulating cancer progression". In: *Scientific Reports* 7.1 (Dec. 2017), p. 15277. ISSN: 2045-2322. DOI: 10.1038/s41598-017-15475-6. URL: http://www.nature.com/articles/s41598-017-15475-6.

[25] Huilin Shao et al. "New Technologies for Analysis of Extracellular Vesicles". In: *Chemical Reviews* 118.4 (Feb. 2018), pp. 1917–1950. ISSN: 0009-2665. DOI: 10.1021/acs.chemrev.7b00534. URL: http://pubs.acs.org/doi/10.1021/acs.chemrev.7b00534.

[26] Zoraida Andreu et al. "Comparative analysis of EV isolation procedures for miRNAs detection in serum samples". In: *Journal of Extracellular Vesicles* 5.1 (Jan. 2016), p. 31655. ISSN: 2001-3078. DOI: 10.3402/jev.v5.31655. URL: https://www.tandfonline.com/doi/full/10.3402/jev.v5.31655.

[27] Davide Marenduzzo, Kieran Finan, and Peter R Cook. "The depletion attraction: an underappreciated force driving cellular organization." In: *The Journal of cell biology* 175.5 (Dec. 2006), pp. 681–6. ISSN: 0021-9525. DOI: 10.1083/jcb.200609066. URL: http://www.ncbi.nlm.nih.gov/pubmed/17145959%20http://www.pubmedcentral.nih.gov/articlerender.fcgi?artid=PMC2064666.

[28] Fei Liu et al. "The Exosome Total Isolation Chip". In: *ACS Nano* 11.11 (Nov. 2017), pp. 10712–10723. ISSN: 1936-0851. DOI: 10.1021/acsnano.7b04878. URL: http://pubs.acs.org/doi/10.1021/acsnano.7b04878.

[29] Mark A. Rider, Stephanie N. Hurwitz, and David G. Meckes. "ExtraPEG: A Polyethylene Glycol-Based Method for Enrichment of Extracellular Vesicles". In: *Scientific Reports* 6.1 (July 2016), p. 23978. ISSN: 2045-2322. DOI: 10.1038/srep23978. URL: http://www.nature.com/articles/srep23978.

[30] Yifei Wang et al. "Rapid Differentiation of Host and Parasitic Exosome Vesicles Using Microfluidic Photonic Crystal Biosensor". In: *ACS Sensors* 3.9 (Sept. 2018), pp. 1616–1621. DOI: 10.1021/ACSSENSORS.8B00360. URL: https://pubs.acs.org/doi/full/10.1021/acssensors.8b00360.

[31] Zheng Zhao et al. "A microfluidic ExoSearch chip for multiplexed exosome detection towards blood-based ovarian cancer diagnosis". In: *Lab on a Chip* 16.3 (Jan. 2016), pp. 489–496. ISSN: 1473-0197. DOI: 10.1039/C5LC01117E. URL: http://xlink.rsc.org/?DOI=C5LC01117E.

[32] Peng Zhang et al. "Ultrasensitive detection of circulating exosomes with a 3D-nanopatterned microfluidic chip". In: *Nature Biomedical Engineering* (Feb. 2019), p. 1. ISSN: 2157-846X. DOI: 10.1038/s41551-019-0356-9. URL: http://www.nature.com/articles/s41551-019-0356-9.

[33] M. Gaillard et al. *Biosensing extracellular vesicles: Contribution of biomolecules in affinity-based methods for detection and isolation.* Mar. 2020. DOI: 10.1039/c9an01949a.

[34] Hyungsoon Im et al. "Label-free detection and molecular profiling of exosomes with a nano-plasmonic sensor". In: *Nature Biotechnology* 32.5 (May 2014), pp. 490–495. ISSN: 1087-0156. DOI: 10.1038/nbt.2886. URL: http://www.nature.com/articles/nbt.2886.

[35] Yunchen Yang et al. "An Immuno-Biochip Selectively Captures Tumor-Derived Exosomes and Detects Exosomal RNAs for Cancer Diagnosis". In: *ACS Applied Materials & Interfaces* 10.50 (Dec. 2018), pp. 43375–43386. DOI: 10.1021/ACSAMI.8B13971. URL: https://pubs.acs.org/doi/full/10.1021/acsami.8b13971.

[36] Shailender Singh Kanwar et al. "Microfluidic device (ExoChip) for on-chip isolation, quantification and characterization of circulating exosomes". In: *Lab Chip* 14.11 (May 2014), pp. 1891–1900. ISSN: 1473-0197. DOI: 10.1039/C4LC00136B. URL: http://xlink.rsc.org/?DOI=C4LC00136B.

[37] Eduardo Reátegui et al. "Engineered nanointerfaces for microfluidic isolation and molecular profiling of tumor-specific extracellular vesicles". In: *Nature Communications* 9.1 (Dec. 2018), p. 175. ISSN: 2041-1723. DOI: 10.1038/s41467-017-02261-1. URL: http://www.nature.com/articles/s41467-017-02261-1.

[38] Peng Zhang, Mei He, and Yong Zeng. "Ultrasensitive microfluidic analysis of circulating exosomes using a nanostructured graphene oxide/polydopamine coating". In: *Lab on a Chip* 16.16 (Aug. 2016), pp. 3033–3042. ISSN: 1473-0197. DOI: 10.1039/C6LC00279J. URL: http://xlink.rsc.org/?DOI=C6LC00279J.

[39] Shuyan Zhu et al. "Highly sensitive detection of exosomes by 3D plasmonic photonic crystal biosensor". In: *Nanoscale* (2018). ISSN: 2040-3364. DOI: 10.1039/C8NR07051B. URL: http://xlink.rsc.org/?DOI=C8NR07051B.

[40] Dilu G. Mathew et al. "Electrochemical Detection of Tumor-Derived Extracellular Vesicles on Nanointerdigitated Electrodes". In: *Nano Letters* (Sept.

2019), acs.nanolett.9b02741. ISSN: 1530-6984. DOI: 10.1021/acs.nanolett.9b02741. URL: https://pubs.acs.org/doi/10.1021/acs.nanolett.9b02741.

[41] Morten P. Oksvold, Axl Neurauter, and Ketil W. Pedersen. "Magnetic Bead-Based Isolation of Exosomes". In: *Methods in Molecular Biology* 1218 (2015), pp. 465–481. DOI: 10.1007/978-1-4939-1538-5{_}27. URL: https://link.springer.com/protocol/10.1007/978-1-4939-1538-5_27.

[42] Mei He et al. "Integrated immunoisolation and protein analysis of circulating exosomes using microfluidic technology". In: *Lab on a Chip* 14.19 (July 2014), p. 3773. ISSN: 1473-0197. DOI: 10.1039/C4LC00662C. URL: http://xlink.rsc.org/?DOI=C4LC00662C.

[43] Richard M. Graybill and Ryan C. Bailey. *Emerging Biosensing Approaches for microRNA Analysis*. Jan. 2016. DOI: 10.1021/acs.analchem.5b04679. URL: https://pubs.acs.org/doi/10.1021/acs.analchem.5b04679.

[44] Philip Gillespie, Sylvain Ladame, and Danny O'Hare. "Molecular methods in electrochemical microRNA detection". In: *The Analyst* 144.1 (Dec. 2019), pp. 114–129. ISSN: 0003-2654. DOI: 10.1039/C8AN01572D. URL: http://xlink.rsc.org/?DOI=C8AN01572D.

[45] Stephen C. Chapin et al. "Rapid microRNA profiling on encoded gel microparticles". In: *Angewandte Chemie - International Edition* 50.10 (2011), pp. 2289–2293. ISSN: 14337851. DOI: 10.1002/anie.201006523.

[46] Colin C. Pritchard, Heather H. Cheng, and Muneesh Tewari. "MicroRNA profiling: Approaches and considerations". In: *Nature Reviews Genetics* 13.5 (May 2012), pp. 358–369. ISSN: 14710056. DOI: 10.1038/nrg3198.

[47] Andrew T. Sage et al. "Ultrasensitive electrochemical biomolecular detection using nanostructured microelectrodes". In: *Accounts of Chemical Research* 47 (2014), pp. 2417–2425. ISSN: 15204898. DOI: 10.1021/ar500130m.

[48] Ruijie Deng, Kaixiang Zhang, and Jinghong Li. "Isothermal Amplification for MicroRNA Detection: From the Test Tube to the Cell". In: *Accounts of Chemical Research* 50.4 (Apr. 2017), pp. 1059–1068. ISSN: 0001-4842. DOI: 10.1021/acs.accounts.7b00040. URL: http://pubs.acs.org/doi/10.1021/acs.accounts.7b00040.

[49] Limor Cohen et al. "Digital direct detection of microRNAs using single molecule arrays". In: *Nucleic acids research* 45.14 (Aug. 2017), e137. ISSN: 13624962. DOI: 10.1093/nar/gkx542.

[50] Ruixue Duan et al. "Lab in a Tube: Ultrasensitive Detection of MicroRNAs at the Single-Cell Level and in Breast Cancer Patients Using Quadratic Isothermal Amplification". In: *Journal of the American Chemical Society* 135.12 (Mar. 2013), pp. 4604–4607. ISSN: 0002-7863. DOI: 10.1021/ja311313b. URL: http://pubs.acs.org/doi/10.1021/ja311313b.

[51] Jie Miao et al. "A plasmonic colorimetric strategy for visual miRNA detection based on hybridization chain reaction". In: *Scientific Reports* 6.1 (Aug. 2016), pp. 1–7. ISSN: 20452322. DOI: 10.1038/srep32219.

[52] Qianqian Tian et al. "Carbon nanotube enhanced label-free detection of microRNAs based on hairpin probe triggered solid-phase rolling-circle amplification". In: *Nanoscale* 7.3 (Dec. 2014), pp. 987–993. ISSN: 2040-3372. DOI: 10.1039/C4NR05243A. URL: https://pubs.rsc.org/en/content/articlehtml/2015/nr/c4nr05243a%20https://pubs.rsc.org/en/content/articlelanding/2015/nr/c4nr05243a.

[53] Peng Miao et al. "Ultrasensitive Detection of MicroRNA through Rolling Circle Amplification on a DNA Tetrahedron Decorated Electrode". In: *Bioconjugate Chemistry* 26.3 (Mar. 2015), pp. 602–607. DOI: 10.1021/ACS.BIOCONJCHEM.5B00064. URL: https://pubs.acs.org/doi/full/10.1021/acs.bioconjchem.5b00064.

[54] Sang Yun Yeom et al. “Multiplexed Detection of Epigenetic Markers Using Quantum Dot (QD)-Encoded Hydrogel Microparticles”. In: *Analytical Chemistry* 88.8 (Apr. 2016), pp. 4259–4268. ISSN: 0003-2700. DOI: 10.1021/acs.analchem.5b04190. URL: https://pubs.acs.org/doi/10.1021/acs.analchem.5b04190.

[55] Lina Wu et al. “Fluorescence hydrogel array based on interfacial cation exchange amplification for highly sensitive microRNA detection”. In: *Analytica Chimica Acta* 1080 (Nov. 2019), pp. 206–214. ISSN: 18734324. DOI: 10.1016/j.aca.2019.07.024.

[56] Ningjing Jiang et al. “Detection of microRNA using a polydopamine mediated bimetallic SERS substrate and a re-circulated enzymatic amplification system”. In: *Microchimica Acta* 186.2 (Feb. 2019), p. 65. ISSN: 0026-3672. DOI: 10.1007/s00604-018-3174-y. URL: http://link.springer.com/10.1007/s00604-018-3174-y.

[57] Xuefei Gao et al. “An enzyme-amplified lateral flow strip biosensor for visual detection of MicroRNA-224”. In: *Talanta* 146 (Jan. 2016), pp. 648–654. ISSN: 00399140. DOI: 10.1016/j.talanta.2015.06.060.

[58] Jiahao Huang, Jueqi Wu, and Zhigang Li. *Biosensing using hairpin DNA probes*. Oct. 2015. DOI: 10.1515/revac-2015-0010.

[59] Sinuo Yu et al. “Application of DNA nanodevices for biosensing”. In: *The Analyst* (2020). ISSN: 0003-2654. DOI: 10.1039/d0an00159g.

[60] Sarah J. Smith, Carine R. Nemr, and Shana O. Kelley. “Chemistry-Driven Approaches for Ultrasensitive Nucleic Acid Detection”. In: *Journal of the American Chemical Society* 139.3 (Jan. 2017), pp. 1020–1028. ISSN: 0002-7863. DOI: 10.1021/jacs.6b10850. URL: http://pubs.acs.org/doi/10.1021/jacs.6b10850.

[61] Gaelle C. Le Goff et al. “Hydrogel microparticles for biosensing”. In: *European Polymer Journal* 72 (Nov. 2015), pp. 386–412. ISSN: 0014-3057. DOI: 10.1016/J.EURPOLYMJ.2015.02.022. URL: http://www.sciencedirect.com/science/article/pii/S001430571500097X.

[62] Sarah J. Shapiro, Dhananjaya Dendukuri, and Patrick S. Doyle. “Design of Hydrogel Particle Morphology for Rapid Bioassays”. In: *Analytical Chemistry* 90.22 (Oct. 2018), pp. 13572–13579. ISSN: 15206882. DOI: 10.1021/acs.analchem.8b03728. URL: http://pubs.acs.org/doi/10.1021/acs.analchem.8b03728.

[63] Nak Won Choi et al. “Multiplexed Detection of mRNA Using Porosity-Tuned Hydrogel Microparticles”. In: *Analytical Chemistry* 84.21 (Nov. 2012), pp. 9370–9378. ISSN: 0003-2700. DOI: 10.1021/ac302128u. URL: http://pubs.acs.org/doi/10.1021/ac302128u.

[64] Yoon Ho Roh et al. “Post-synthesis functionalized hydrogel microparticles for high performance microRNA detection”. In: *Analytica Chimica Acta* 1076 (Oct. 2019), pp. 110–117. ISSN: 0003-2670. DOI: 10.1016/J.ACA.2019.05.009. URL: https://www.sciencedirect.com/science/article/pii/S0003267019305537#undfig1.

[65] Hye Jin Kim et al. “Highly sensitive three-dimensional interdigitated microelectrode biosensors embedded with porosity tunable hydrogel for detecting proteins”. In: *Sensors and Actuators, B: Chemical* 302 (Jan. 2020), p. 127190. ISSN: 09254005. DOI: 10.1016/j.snb.2019.127190.

[66] Augusto M. Tentori et al. “Quantitative and multiplex microRNA assays from unprocessed cells in isolated nanoliter well arrays”. In: *Lab on a Chip* 18.16 (Aug. 2018), pp. 2410–2424. ISSN: 1473-0197. DOI: 10.1039/C8LC00498F. URL: http://xlink.rsc.org/?DOI=C8LC00498F.

[67] Maxwell B. Nagarajan et al. “Nonfouling, Encoded Hydrogel Microparticles for Multiplex MicroRNA Profiling Directly from Formalin-Fixed, Paraffin-

Embedded Tissue". In: *Analytical Chemistry* 90.17 (Sept. 2018), pp. 10279–10285. ISSN: 0003-2700. DOI: 10.1021/acs.analchem.8b02010. URL: http://pubs.acs.org/doi/10.1021/acs.analchem.8b02010.

[68] Stephen C. Chapin. "Encoded Hydrogel Microparticles for high-Throughput Molecular Diagnostics and Personalized Medicine". PhD thesis. PhD Thesis, Massachusetts Institute of Technology, 2012.

[69] Hyun Jee Lee et al. "Multiplexed immunoassay using post-synthesis functionalized hydrogel microparticles". In: *Lab on a Chip* 19 (2019), pp. 111–119. ISSN: 1473-0197. DOI: 10.1039/C8LC01160E. URL: http://xlink.rsc.org/?DOI=C8LC01160E.

[70] Hyewon Lee et al. "Sensitive and multiplexed on-chip microRNA profiling in oil-isolated hydrogel chambers". In: *Angewandte Chemie - International Edition* 54.8 (2015), pp. 2477–2481. ISSN: 15213773. DOI: 10.1002/anie.201409489.

[71] Gaelle C. Le Goff, Loïc J. Blum, and Christophe A. Marquette. "Shrinking Hydrogel-DNA Spots Generates 3D Microdots Arrays". In: *Macromolecular Bioscience* 13.2 (Feb. 2013), pp. 227–233. ISSN: 16165187. DOI: 10.1002/mabi.201200370. URL: http://doi.wiley.com/10.1002/mabi.201200370.

[72] Eric Y. Liu et al. "High-throughput double emulsion-based microfluidic production of hydrogel microspheres with tunable chemical functionalities toward biomolecular conjugation". In: *Lab on a Chip* 18.2 (Jan. 2018), pp. 323–334. ISSN: 1473-0197. DOI: 10.1039/C7LC01088E. URL: http://xlink.rsc.org/?DOI=C7LC01088E.

[73] Dhananjay Dendukuri et al. "Stop-flow lithography in a microfluidic device". In: *Lab on a Chip* 7.7 (June 2007), p. 818. ISSN: 1473-0197. DOI: 10.1039/b703457a. URL: http://xlink.rsc.org/?DOI=b703457a.

[74] Daniel C. Pregibon, Mehmet Toner, and Patrick S. Doyle. "Multifunctional encoded particles for high-throughput biomolecule analysis". In: *Science* 315.5817 (Mar. 2007), pp. 1393–1396. ISSN: 00368075. DOI: 10.1126/science.1134929. URL: http://www.ncbi.nlm.nih.gov/pubmed/10976071%20http://www.ncbi.nlm.nih.gov/pubmed/17347435.

[75] Dhananjay Dendukuri et al. "Modeling of Oxygen-Inhibited Free Radical Photopolymerization in a PDMS Microfluidic Device". In: *Macromolecules* 41.22 (Nov. 2008), pp. 8547–8556. ISSN: 0024-9297. DOI: 10.1021/ma801219w. URL: http://pubs.acs.org/doi/abs/10.1021/ma801219w.

[76] Stephen C. Chapin and Patrick S. Doyle. "Ultrasensitive Multiplexed MicroRNA Quantification on Encoded Gel Microparticles Using Rolling Circle Amplification". In: *Analytical Chemistry* 83.18 (Sept. 2011), pp. 7179–7185. ISSN: 0003-2700. DOI: 10.1021/ac201618k. URL: http://pubs.acs.org/doi/abs/10.1021/ac201618k.

[77] Jae Jung Kim, Lynna Chen, and Patrick S. Doyle. "Microparticle parking and isolation for highly sensitive microRNA detection". In: *Lab on a Chip* 17.18 (Sept. 2017), pp. 3120–3128. ISSN: 1473-0197. DOI: 10.1039/C7LC00653E. URL: http://xlink.rsc.org/?DOI=C7LC00653E.

[78] Rathi L. Srinivas, Stephen C. Chapin, and Patrick S. Doyle. "Aptamer-Functionalized Microgel Particles for Protein Detection". In: *Analytical Chemistry* 83.23 (Dec. 2011), pp. 9138–9145. ISSN: 0003-2700. DOI: 10.1021/ac202335u. URL: http://pubs.acs.org/doi/abs/10.1021/ac202335u.

[79] Maxwell B. Nagarajan et al. "Spatially resolved and multiplexed MicroRNA quantification from tissue using nanoliter well arrays". In: *Microsystems & Nanoengineering* 6.1 (Dec. 2020), p. 51. ISSN: 2055-7434. DOI: 10.1038/s41378-020-0169-8. URL: http://www.nature.com/articles/s41378-020-0169-8.

[80] Ki Wan Bong et al. “Compressed-air flow control system”. In: *Lab Chip* 11.4 (Jan. 2011), pp. 743–747. ISSN: 1473-0197. DOI: 10.1039/C0LC00303D. URL: http://xlink.rsc.org/?DOI=C0LC00303D.

[81] Nidhi Juthani and Patrick S. Doyle. “A platform for multiplexed colorimetric microRNA detection using shape-encoded hydrogel particles”. In: *Analyst* 145.15 (Aug. 2020), pp. 5134–5140. ISSN: 13645528. DOI: 10.1039/d0an00938e. URL: https://pubs.rsc.org/en/content/articlehtml/2020/an/d0an00938e%20https://pubs.rsc.org/en/content/articlelanding/2020/an/d0an00938e.

[82] Donghyuk Kim et al. “Enzyme-Free Nucleic Acid Amplification Assay Using a Cellphone-Based Well Plate Fluorescence Reader”. In: *Analytical Chemistry* 90.1 (Jan. 2018), pp. 690–695. ISSN: 0003-2700. DOI: 10.1021/acs.analchem.7b03848. URL: https://pubs.acs.org/doi/10.1021/acs.analchem.7b03848.

[83] Qinya Feng et al. “One bead three targets: An enzyme-free platform enabling simultaneous detection of multiplex MicroRNAs on a single microbead”. In: *Sensors and Actuators B: Chemical* 301 (Dec. 2019), p. 127119. ISSN: 0925-4005. DOI: 10.1016/J.SNB.2019.127119. URL: https://www.sciencedirect.com/science/article/pii/S0925400519313188#fig0005.

[84] Gaelle C. Le Goff et al. “Impact of immobilization support on colorimetric microarrays performances”. In: *Biosensors and Bioelectronics* 35.1 (May 2012), pp. 94–100. ISSN: 09565663. DOI: 10.1016/j.bios.2012.02.025.

[85] I. Hernández-Neuta et al. “Smartphone-based clinical diagnostics: towards democratization of evidence-based health care”. In: *Journal of Internal Medicine* 285.1 (Jan. 2019), pp. 19–39. ISSN: 09546820. DOI: 10.1111/joim.12820. URL: http://doi.wiley.com/10.1111/joim.12820.

[86] Lei Huang et al. “Multiplexed detection of biomarkers in lateral-flow immunoassays”. In: *The Analyst* 145.8 (Apr. 2020), pp. 2828–2840. ISSN: 0003-2654. DOI: 10.1039/c9an02485a.

[87] Shefali Lathwal and Hadley D. Sikes. “Assessment of colorimetric amplification methods in a paper-based immunoassay for diagnosis of malaria”. In: *Lab on a Chip* 16.8 (Apr. 2016), pp. 1374–1382. ISSN: 1473-0197. DOI: 10.1039/C6LC00058D. URL: http://xlink.rsc.org/?DOI=C6LC00058D.

[88] Emma H. Yee and Hadley D. Sikes. “Polymerization-Based Amplification for Target-Specific Colorimetric Detection of Amplified Mycobacterium tuberculosis DNA on Cellulose”. In: *ACS Sensors* 5.2 (Feb. 2020), pp. 308–312. ISSN: 23793694. DOI: 10.1021/acssensors.9b02424. URL: https://pubs.acs.org/doi/10.1021/acssensors.9b02424.

[89] Alexandr E. Urusov, Anatoly V. Zherdev, and Boris B. Dzantiev. *Towards lateral flow quantitative assays: Detection approaches*. Sept. 2019. DOI: 10.3390/bios9030089.

[90] Shuangqin Wei et al. “Exponential amplification reaction and triplex DNA mediated aggregation of gold nanoparticles for sensitive colorimetric detection of microRNA”. In: *Analytica Chimica Acta* 1095 (Jan. 2020), pp. 179–184. ISSN: 18734324. DOI: 10.1016/j.aca.2019.10.020.

[91] Jiquan Jiang et al. “A Novel Design Combining Isothermal Exponential Amplification and Gold-Nanoparticles Visualization for Rapid Detection of miRNAs”. In: *International Journal of Molecular Sciences* 19.11 (Oct. 2018), p. 3374. ISSN: 1422-0067. DOI: 10.3390/ijms19113374. URL: http://www.mdpi.com/1422-0067/19/11/3374.

[92] Juan Dong et al. “Colorimetric PCR-Based microRNA Detection Method Based on Small Organic Dye and Single Enzyme”. In: *Analytical Chemistry* 90.12 (June 2018), pp. 7107–7111. ISSN: 0003-2700. DOI: 10.1021/acs.

analchem.8b01111. URL: https://pubs.acs.org/doi/10.1021/acs.analchem.8b01111.

[93] Stefano Persano et al. "Label-Free Isothermal Amplification Assay for Specific and Highly Sensitive Colorimetric miRNA Detection". In: *ACS Omega* 1.3 (Sept. 2016), pp. 448–455. ISSN: 24701343. DOI: 10.1021/acsomega.6b00109.

[94] Wei Shen et al. "A real-time colorimetric assay for label-free detection of microRNAs down to sub-femtomolar levels". In: *Chemical Communications* 49.43 (May 2013), pp. 4959–4961. ISSN: 1364548X. DOI: 10.1039/c3cc41565a.

[95] Qian Wang et al. "Colorimetric detection of sequence-specific microRNA based on duplex-specific nuclease-assisted nanoparticle amplification". In: *Analyst* 140.18 (Sept. 2015), pp. 6306–6312. ISSN: 13645528. DOI: 10.1039/c5an01350j.

[96] Chunchen Liu et al. "Single-Exosome-Counting Immunoassays for Cancer Diagnostics". In: *Nano Letters* 18.7 (July 2018), pp. 4226–4232. ISSN: 1530-6984. DOI: 10.1021/acs.nanolett.8b01184. URL: http://pubs.acs.org/doi/10.1021/acs.nanolett.8b01184.

[97] Makiko N. Hatori, Samuel C. Kim, and Adam R. Abate. "Particle-Templated Emulsification for Microfluidics-Free Digital Biology". In: *Analytical Chemistry* 90.16 (Aug. 2018), pp. 9813–9820. ISSN: 0003-2700. DOI: 10.1021/acs.analchem.8b01759. URL: https://pubs.acs.org/doi/10.1021/acs.analchem.8b01759.

[98] Ghulam Destgeer et al. "Fabrication of 3D concentric amphiphilic microparticles to form uniform nanoliter reaction volumes for amplified affinity assays". In: *Lab on a Chip* 20.19 (Sept. 2020), pp. 3503–3514. ISSN: 1473-0189. DOI: 10.1039/D0LC00698J. URL: https://pubs.rsc.org/en/content/articlehtml/2020/lc/d0lc00698j%20https://pubs.rsc.org/en/content/articlelanding/2020/lc/d0lc00698j.

[99] Hyewon Lee et al. “Hydrogel-Based Colorimetric Assay for Multiplexed MicroRNA Detection in a Microfluidic Device”. In: *Analytical Chemistry* 92.8 (Apr. 2020), pp. 5750–5755. ISSN: 0003-2700. DOI: 10.1021/acs.analchem.9b05043.

[100] Jennifer A Schumacher et al. “Two-color fluorescent in situ hybridization using chromogenic substrates in zebrafish.” In: *BioTechniques* 57.5 (Nov. 2014), pp. 254–6. ISSN: 1940-9818. DOI: 10.2144/000114229. URL: http://www.ncbi.nlm.nih.gov/pubmed/25391914%20http://www.pubmedcentral.nih.gov/articlerender.fcgi?artid=PMC4336792.

[101] Sigma-Aldrich. *Colorimetric Alkaline Phosphatase and Peroxidase Substrate Detection Systems*. Tech. rep. 4. 2008, p. 6. URL: http://www.sigmaaldrich.com/technical-documents/articles/biofiles/colorimetric-alkaline.html.

[102] Richard C. Murdock et al. “Optimization of a Paper-Based ELISA for a Human Performance Biomarker”. In: *Analytical Chemistry* 85.23 (Dec. 2013), pp. 11634–11642. ISSN: 0003-2700. DOI: 10.1021/ac403040a. URL: https://pubs.acs.org/doi/10.1021/ac403040a.

[103] Eunae Kang et al. “Shape-Encoded Chitosan–Polyacrylamide Hybrid Hydrogel Microparticles with Controlled Macroporous Structures via Replica Molding for Programmable Biomacromolecular Conjugation”. In: *Langmuir* 32.21 (May 2016), pp. 5394–5402. ISSN: 0743-7463. DOI: 10.1021/acs.langmuir.5b04653. URL: https://pubs.acs.org/doi/10.1021/acs.langmuir.5b04653.

[104] Christina L. Lewis et al. “Fabrication of Uniform DNA-Conjugated Hydrogel Microparticles via Replica Molding for Facile Nucleic Acid Hybridization Assays”. In: *Analytical Chemistry* 82.13 (July 2010), pp. 5851–5858. ISSN: 0003-2700. DOI: 10.1021/ac101032r. URL: https://pubs.acs.org/doi/10.1021/ac101032r.

[105] Daniel C. Pregibon and Patrick S. Doyle. "Optimization of encoded hydrogel particles for nucleic acid quantification". In: *Analytical Chemistry* 81.12 (2009), pp. 4873–4881. ISSN: 00032700. DOI: 10.1021/ac9005292.

[106] Jae Jung Kim et al. "Porous microwells for geometry-selective, large-scale microparticle arrays". In: *Nature Materials* 16.1 (2017), pp. 139–146. ISSN: 14764660. DOI: 10.1038/nmat4747.

[107] Rathi Lakshmi Srinivas. "Hydrogel-Based MIcrofluidic Assays for Multiplexed Medical Diagnostics". PhD thesis. PhD Thesis, Massachusetts Institute of Technology, 2015.

[108] Mojdeh Mahdiannasser and Zahra Karami. "An innovative paradigm of methods in microRNAs detection: highlighting DNAzymes, the illuminators". In: *Biosensors and Bioelectronics* 107 (June 2018), pp. 123–144. ISSN: 18734235. DOI: 10.1016/j.bios.2018.02.020.

[109] Changxuan You et al. "Expression of miR-21 and miR-138 in colon cancer and its effect on cell proliferation and prognosis". In: *Oncology Letters* 17.2 (Feb. 2019), pp. 2271–2277. ISSN: 17921082. DOI: 10.3892/ol.2018.9864.

[110] Jie Yang et al. "Expression analysis of microRNA as prognostic biomarkers in colorectal cancer". In: *Oncotarget* 8.32 (Aug. 2017), pp. 52403–52412. ISSN: 1949-2553. DOI: 10.18632/oncotarget.14175. URL: 10.18632/oncotarget.14175.

[111] Hanyin Cheng et al. "Circulating plasma MiR-141 is a novel biomarker for metastatic colon cancer and predicts poor prognosis". In: *PLoS ONE* 6.3 (2011). ISSN: 19326203. DOI: 10.1371/journal.pone.0017745.

[112] Molecular Probes. *Certificate of Analysis*. Tech. rep. 2017.

[113] John R Chevillet et al. "Quantitative and stoichiometric analysis of the microRNA content of exosomes." In: *Proceedings of the National Academy of Sciences of the United States of America* 111.41 (Oct. 2014), pp. 14888–93.

ISSN: 1091-6490. DOI: 10.1073/pnas.1408301111. URL: http://www.ncbi.nlm.nih.gov/pubmed/25267620%20http://www.pubmedcentral.nih.gov/articlerender.fcgi?artid=PMC4205618.

[114] Daniel Taller et al. "On-chip surface acoustic wave lysis and ion-exchange nanomembrane detection of exosomal RNA for pancreatic cancer study and diagnosis". In: *Lab on a Chip* 15.7 (Mar. 2015), pp. 1656–1666. ISSN: 1473-0197. DOI: 10.1039/C5LC00036J. URL: http://xlink.rsc.org/?DOI=C5LC00036J.

[115] Hyewon Lee et al. "Encoded Hydrogel Microparticles for Sensitive and Multiplex microRNA Detection Directly from Raw Cell Lysates". In: *Analytical Chemistry* 88.6 (Mar. 2016), pp. 3075–3081. ISSN: 0003-2700. DOI: 10.1021/acs.analchem.5b03902. URL: http://pubs.acs.org/doi/10.1021/acs.analchem.5b03902.

[116] Junbeom Kim et al. "Hydrogel-based hybridization chain reaction (HCR) for detection of urinary exosomal miRNAs as a diagnostic tool of prostate cancer". In: *Biosensors and Bioelectronics* 192 (Nov. 2021), p. 113504. ISSN: 0956-5663. DOI: 10.1016/J.BIOS.2021.113504. URL: https://linkinghub.elsevier.com/retrieve/pii/S0956566321005418.

[117] Chueh-Yu Wu et al. "Monodisperse drops templated by 3D-structured microparticles". In: *Science Advances* 6.45 (Nov. 2020), eabb9023. ISSN: 2375-2548. DOI: 10.1126/SCIADV.ABB9023. URL: https://advances.sciencemag.org/content/6/45/eabb9023%20https://advances.sciencemag.org/content/6/45/eabb9023.abstract.

[118] Yilian Wang et al. "Counting of Enzymatically Amplified Affinity Reactions in Hydrogel Particle-Templated Drops". In: *bioRxiv* (Apr. 2021), p. 2021.04.21.440664. DOI: 10.1101/2021.04.21.440664. URL: https://www.biorxiv.org/content/10.1101/2021.04.21.440664v1%20https://www.biorxiv.org/content/10.1101/2021.04.21.440664v1.abstract.

[119] Violette B. Paragas et al. “The ELF-97 Alkaline Phosphatase Substrate Provides a Bright, Photostable, Fluorescent Signal Amplification Method for FISH”. In: *Journal of Histochemistry & Cytochemistry* 45.3 (Mar. 1997), pp. 345–357. ISSN: 0022-1554. DOI: 10.1177/002215549704500302. URL: http://journals.sagepub.com/doi/10.1177/002215549704500302.

[120] V. B. Paragas et al. “The ELFR-97 phosphatase substrate provides a sensitive, photostable method for labelling cytological targets”. In: *Journal of Microscopy* 206.2 (May 2002), pp. 106–119. ISSN: 0022-2720. DOI: 10.1046/j.1365-2818.2002.01017.x. URL: http://doi.wiley.com/10.1046/j.1365-2818.2002.01017.x.

[121] Cuiping Ma, Sen Liu, and Chao Shi. “Ultrasensitive detection of microRNAs based on hairpin fluorescence probe assisted isothermal amplification”. In: *Biosensors and Bioelectronics* 58 (Aug. 2014), pp. 57–60. ISSN: 18734235. DOI: 10.1016/j.bios.2014.02.034.

[122] Maria Chiara Giuffrida et al. “Isothermal circular-strand-displacement polymerization of DNA and microRNA in digital microfluidic devices”. In: *Analytical and Bioanalytical Chemistry* 407.6 (Feb. 2015), pp. 1533–1543. ISSN: 16182650. DOI: 10.1007/s00216-014-8405-4. URL: https://link.springer.com/article/10.1007/s00216-014-8405-4.

[123] Tian Tian et al. “Simultaneously sensitive detection of multiple miRNAs based on a strand displacement amplification”. In: *Chem. Commun.* 49.1 (Nov. 2013), pp. 75–77. ISSN: 1359-7345. DOI: 10.1039/C2CC36728A. URL: http://xlink.rsc.org/?DOI=C2CC36728A.

[124] Joseph Malcolm Schaeffer. “Stochastic Simulation of the Kinetics of Multiple Interacting Nucleic Acid Strands”. PhD thesis. California Institute of Technology, 2012.

[125] Joseph Malcolm Schaeffer, Chris Thachuk, and Erik Winfree. “Stochastic simulation of the kinetics of multiple interacting nucleic acid strands”. In:

Lecture Notes in Computer Science (including subseries Lecture Notes in Artificial Intelligence and Lecture Notes in Bioinformatics). Vol. 9211. Springer Verlag, 2015, pp. 194–211. ISBN: 9783319219981. DOI: 10.1007/978-3-319-21999-8{_}13.

[126] Hyundo Lee et al. "Creating Isolated Liquid Compartments Using Photopatterned Obstacles in Microfluidics". In: *Physical Review Applied* 7.4 (2017), pp. 1–13. ISSN: 23317019. DOI: 10.1103/PhysRevApplied.7.044013.

[127] Joseph N. Zadeh et al. "NUPACK: Analysis and design of nucleic acid systems". In: *Journal of Computational Chemistry* 32.1 (Jan. 2011), pp. 170–173. ISSN: 1096-987X. DOI: 10.1002/JCC.21596. URL: https://onlinelibrary.wiley.com/doi/full/10.1002/jcc.21596%20https://onlinelibrary.wiley.com/doi/abs/10.1002/jcc.21596%20https://onlinelibrary.wiley.com/doi/10.1002/jcc.21596.

[128] Jian Zhang et al. *Exosome and exosomal microRNA: Trafficking, sorting, and function*. Feb. 2015. DOI: 10.1016/j.gpb.2015.02.001.

[129] Arron Thind and Clive Wilson. "Exosomal miRNAs as cancer biomarkers and therapeutic targets". In: *Journal of Extracellular Vesicles* 5.1 (Jan. 2016), p. 31292. ISSN: 2001-3078. DOI: 10.3402/jev.v5.31292. URL: https://www.tandfonline.com/doi/full/10.3402/jev.v5.31292.

[130] Srimeenakshi Srinivasan et al. "Small RNA Sequencing across Diverse Biofluids Identifies Optimal Methods for exRNA Isolation". In: *Cell* 177.2 (Apr. 2019), pp. 446–462. ISSN: 10974172. DOI: 10.1016/j.cell.2019.03.024.

[131] Rachel E. Crossland et al. "Evaluation of optimal extracellular vesicle small RNA isolation and qRT-PCR normalisation for serum and urine". In: *Journal of Immunological Methods* 429 (Feb. 2016), pp. 39–49. ISSN: 0022-1759. DOI: 10.1016/J.JIM.2015.12.011. URL: https://www.sciencedirect.com/science/article/pii/S0022175915300776.

[132] Ji Hye Lee et al. "Simultaneous and multiplexed detection of exosome microRNAs using molecular beacons". In: *Biosensors and Bioelectronics* 86 (Dec. 2016), pp. 202–210. ISSN: 0956-5663. DOI: 10.1016/J.BIOS.2016.06.058. URL: https://www.sciencedirect.com/science/article/pii/S0956566316305929.

[133] Li Liu et al. "Synergy of Peptide-Nucleic Acid and Spherical Nucleic Acid Enabled Quantitative and Specific Detection of Tumor Exosomal MicroRNA". In: *Analytical Chemistry* 91.20 (Oct. 2019), pp. 13198–13205. ISSN: 15206882. DOI: 10.1021/acs.analchem.9b03622.

[134] Warren D. Gray, Adam J. Mitchell, and Charles D. Searles. "An accurate, precise method for general labeling of extracellular vesicles". In: *MethodsX* 2 (Jan. 2015), pp. 360–367. ISSN: 2215-0161. DOI: 10.1016/J.MEX.2015.08.002. URL: https://www.sciencedirect.com/science/article/pii/S2215016115000448#bib0105.

[135] Schopf E and Chen Y. "Attomole DNA detection assay via rolling circle amplification and single molecule detection". In: *Analytical biochemistry* 397.1 (Feb. 2010), pp. 115–117. ISSN: 1096-0309. DOI: 10.1016/J.AB.2009.09.023. URL: https://pubmed.ncbi.nlm.nih.gov/19761749/.

[136] Inas Helwa et al. "A Comparative Study of Serum Exosome Isolation Using Differential Ultracentrifugation and Three Commercial Reagents". In: *PLOS ONE* 12.1 (Jan. 2017). Ed. by Giovanni Camussi, e0170628. ISSN: 1932-6203. DOI: 10.1371/journal.pone.0170628. URL: http://dx.plos.org/10.1371/journal.pone.0170628.

[137] Alexander V Vlassov et al. *US008901284B2*. Feb. 2014.

[138] Daniel Bachurski et al. "Extracellular vesicle measurements with nanoparticle tracking analysis–An accuracy and repeatability comparison between NanoSight NS300 and ZetaView". In: *Journal of Extracellular Vesicles* 8.1 (Jan. 2019), e1596016. ISSN: 20013078. DOI: 10.1080/20013078.2019.

1596016. URL: https://www.tandfonline.com/doi/abs/10.1080/20013078.2019.1596016.

[139] Tanina Arab et al. "Characterization of extracellular vesicles and synthetic nanoparticles with four orthogonal single-particle analysis platforms". In: *Journal of Extracellular Vesicles* 10.6 (Apr. 2021), e12079. ISSN: 2001-3078. DOI: 10.1002/JEV2.12079. URL: https://onlinelibrary.wiley.com/doi/full/10.1002/jev2.12079%20https://onlinelibrary.wiley.com/doi/abs/10.1002/jev2.12079%20https://onlinelibrary.wiley.com/doi/10.1002/jev2.12079.

[140] Kevin S. Silmore et al. "High-Resolution Nanoparticle Sizing with Maximum A Posteriori Nanoparticle Tracking Analysis". In: *ACS Nano* 13.4 (Apr. 2019), pp. 3940–3952. DOI: 10.1021/ACSNANO.8B07215. URL: https://pubs.acs.org/doi/full/10.1021/acsnano.8b07215.

[141] Lew Brown, Jean-Luc Fraikin, and Franklin Monzon. *Where's my Peak?: Separating Truth from Fiction in Label-Free Measurements of EVs*. Tech. rep. Barcelona: Spectradyne LLC., 2018. URL: https://nanoparticleanalyzer.com/pdf/2018ISEVSpectradyneVendorPosterFinal.pdf.

[142] Jean-Luc Fraikin et al. "A high-throughput label-free nanoparticle analyser". In: *Nature Nanotechnology* 6.5 (May 2011), pp. 308–313. ISSN: 1748-3387. DOI: 10.1038/nnano.2011.24. URL: http://www.nature.com/articles/nnano.2011.24.

[143] Diána Kitka et al. "Detection and phenotyping of extracellular vesicles by size exclusion chromatography coupled with on-line fluorescence detection". In: *Scientific Reports* 9.1 (Dec. 2019), pp. 1–7. ISSN: 20452322. DOI: 10.1038/s41598-019-56375-1.

[144] Xabier Osteikoetxea et al. "Differential detergent sensitivity of extracellular vesicle subpopulations". In: *Organic & Biomolecular Chemistry* 13.38 (Sept.

2015), pp. 9775–9782. ISSN: 1477-0520. DOI: 10.1039/C5OB01451D. URL: http://xlink.rsc.org/?DOI=C5OB01451D.

[145] E. van der Pol et al. "Recent developments in the nomenclature, presence, isolation, detection and clinical impact of extracellular vesicles". In: *Journal of Thrombosis and Haemostasis* 14.1 (Jan. 2016), pp. 48–56. ISSN: 1538-7836. DOI: 10.1111/JTH.13190. URL: https://onlinelibrary.wiley.com/doi/full/10.1111/jth.13190%20https://onlinelibrary.wiley.com/doi/abs/10.1111/jth.13190%20https://onlinelibrary.wiley.com/doi/10.1111/jth.13190.

[146] Kasper Bendix Johnsen et al. "What is the blood concentration of extracellular vesicles? Implications for the use of extracellular vesicles as blood-borne biomarkers of cancer". In: *Biochimica et Biophysica Acta (BBA) - Reviews on Cancer* 1871.1 (Jan. 2019), pp. 109–116. ISSN: 0304-419X. DOI: 10.1016/J.BBCAN.2018.11.006. URL: https://www.sciencedirect.com/science/article/pii/S0304419X1830180X.

[147] Qunqun Guo et al. "Electrochemical Sensing of Exosomal MicroRNA Based on Hybridization Chain Reaction Signal Amplification with Reduced False-Positive Signals". In: *Analytical Chemistry* 92.7 (Mar. 2020), pp. 5302–5310. ISSN: 15206882. DOI: 10.1021/acs.analchem.9b05849. URL: https://pubs.acs.org/doi/10.1021/acs.analchem.9b05849.

[148] Gayatri K. Joshi et al. "Label-Free Nanoplasmonic-Based Short Noncoding RNA Sensing at Attomolar Concentrations Allows for Quantitative and Highly Specific Assay of MicroRNA-10b in Biological Fluids and Circulating Exosomes". In: *ACS Nano* 9.11 (Nov. 2015), pp. 11075–11089. DOI: 10.1021/ACSNANO.5B04527. URL: https://pubs.acs.org/doi/full/10.1021/acsnano.5b04527.

[149] Yuanfeng Pang et al. "Dual-SERS biosensor for one-step detection of microRNAs in exosome and residual plasma of blood samples for diagnosing pancre-

atic cancer". In: *Biosensors and Bioelectronics* 130 (Apr. 2019), pp. 204–213. ISSN: 0956-5663. DOI: 10.1016/J.BIOS.2019.01.039.

[150] Lynna Chen et al. "Flexible Octopus-Shaped Hydrogel Particles for Specific Cell Capture". In: *Small* 12.15 (2016), pp. 2001–2008. ISSN: 16136829. DOI: 10.1002/smll.201600163.

[151] Minggan Li et al. "Fabrication of Highly Porous Nonspherical Particles Using Stop-Flow Lithography and the Study of Their Optical Properties". In: *Langmuir* 33.1 (Jan. 2017), pp. 184–190. ISSN: 0743-7463. DOI: 10.1021/acs.langmuir.6b03358. URL: http://pubs.acs.org/doi/10.1021/acs.langmuir.6b03358.

[152] Hyun June Moon et al. "Elimination of Unreacted Acrylate Double Bonds in the Polymer Networks of Microparticles Synthesized via Flow Lithography". In: *Langmuir* (Feb. 2020). ISSN: 0743-7463. DOI: 10.1021/acs.langmuir.9b02737.

[153] Devatha P. Nair et al. *The Thiol-Michael addition click reaction: A powerful and widely used tool in materials chemistry*. Jan. 2014. DOI: 10.1021/cm402180t. URL: https://pubs.acs.org/sharingguidelines.

[154] Chelsea N. Salinas and Kristi S. Anseth. "Mixed Mode Thiol - Acrylate Photopolymerizations for the Synthesis of PEG - Peptide Hydrogels". In: *Macromolecules* 41.16 (Aug. 2008), pp. 6019–6026. ISSN: 00249297. DOI: 10.1021/ma800621h. URL: https://pubs.acs.org/sharingguidelines.

[155] Gaelle C. Le Goff et al. "High-Throughput Contact Flow Lithography". In: *Advanced Science* 2.10 (Oct. 2015), p. 1500149. ISSN: 2198-3844. DOI: 10.1002/ADVS.201500149. URL: https://onlinelibrary.wiley.com/doi/full/10.1002/advs.201500149%20https://onlinelibrary.wiley.com/doi/abs/10.1002/advs.201500149%20https://onlinelibrary.wiley.com/doi/10.1002/advs.201500149.

[156] David C. Appleyard, Stephen C. Chapin, and Patrick S. Doyle. "Multiplexed Protein Quantification with Barcoded Hydrogel Microparticles". In: *Analytical Chemistry* 83.1 (Jan. 2011), pp. 193–199. ISSN: 0003-2700. DOI: 10.1021/ac1022343. URL: http://pubs.acs.org/doi/abs/10.1021/ac1022343.

[157] Andrew G Lee et al. "Development of macroporous poly(ethylene glycol) hydrogel arrays within microfluidic channels." In: *Biomacromolecules* 11.12 (Dec. 2010), pp. 3316–24. ISSN: 1526-4602. DOI: 10.1021/bm100792y. URL: http://www.ncbi.nlm.nih.gov/pubmed/21028794%20http://www.pubmedcentral.nih.gov/articlerender.fcgi?artid=PMC3006031.

[158] Dohyun Kim and Amy E. Herr. "Protein immobilization techniques for microfluidic assays". In: *Biomicrofluidics* 7.4 (July 2013), p. 041501. ISSN: 19321058. DOI: 10.1063/1.4816934.

[159] Eric Y. Liu, Sukwon Jung, and Hyunmin Yi. "Improved Protein Conjugation with Uniform, Macroporous Poly(acrylamide- co -acrylic acid) Hydrogel Microspheres via EDC/NHS Chemistry". In: *Langmuir* 32.42 (Oct. 2016), pp. 11043–11054. ISSN: 0743-7463. DOI: 10.1021/acs.langmuir.6b02591. URL: http://pubs.acs.org/doi/10.1021/acs.langmuir.6b02591.

[160] Kyung-A Hyun et al. "Epithelial-to-mesenchymal transition leads to loss of EpCAM and different physical properties in circulating tumor cells from metastatic breast cancer". In: *Oncotarget* 7.17 (Apr. 2016), p. 24677. DOI: 10.18632/ONCOTARGET.8250. URL: /pmc/articles/PMC5029733/%20/pmc/articles/PMC5029733/?report=abstract%20https://www.ncbi.nlm.nih.gov/pmc/articles/PMC5029733/.

[161] Anne-Kathleen Rupp et al. "Loss of EpCAM expression in breast cancer derived serum exosomes: Role of proteolytic cleavage". In: *Gynecologic Oncology* 122.2 (Aug. 2011), pp. 437–446. ISSN: 0090-8258. DOI: 10.1016/J.YGYNO.2011.04.035. URL: http://www.gynecologiconcology-online.net/article/S0090825811003362/fulltext%20http://www.gynecologiconcology-

online.net/article/S0090825811003362/abstract%20https://www.gynecologiconcology-online.net/article/S0090-8258(11)00336-2/abstract.

[162] Coy Austin Fitts et al. "Exploiting Exosomes in Cancer Liquid Biopsies and Drug Delivery". In: *Advanced Healthcare Materials* (Jan. 2019), p. 1801268. ISSN: 21922640. DOI: 10.1002/adhm.201801268. URL: http://doi.wiley.com/10.1002/adhm.201801268.

[163] Samir El Andaloussi et al. *Extracellular vesicles: Biology and emerging therapeutic opportunities*. May 2013. DOI: 10.1038/nrd3978.

[164] Sangiliyandi Gurunathan et al. "Review of the Isolation, Characterization, Biological Function, and Multifarious Therapeutic Approaches of Exosomes". In: *Cells* 8.4 (Apr. 2019). ISSN: 2073-4409. DOI: 10.3390/CELLS8040307. URL: https://pubmed.ncbi.nlm.nih.gov/30987213/.

[165] Sweta Rani et al. "Mesenchymal Stem Cell-derived Extracellular Vesicles: Toward Cell-free Therapeutic Applications". In: *Molecular therapy : the journal of the American Society of Gene Therapy* 23.5 (May 2015), pp. 812–823. ISSN: 1525-0024. DOI: 10.1038/MT.2015.44. URL: https://pubmed.ncbi.nlm.nih.gov/25868399/.

[166] Guillaume Van Niel, Gisela D'Angelo, and Graça Raposo. "Shedding light on the cell biology of extracellular vesicles". In: *Nature reviews. Molecular cell biology* 19.4 (Apr. 2018), pp. 213–228. ISSN: 1471-0080. DOI: 10.1038/NRM.2017.125. URL: https://pubmed.ncbi.nlm.nih.gov/29339798/.

[167] Meng Kou et al. "Mesenchymal stem cell-derived extracellular vesicles for immunomodulation and regeneration: a next generation therapeutic tool?" In: *Cell Death & Disease 2022 13:7* 13.7 (July 2022), pp. 1–16. ISSN: 2041-4889. DOI: 10.1038/s41419-022-05034-x. URL: https://www.nature.com/articles/s41419-022-05034-x.

[168] Alicia Llorente et al. “Molecular lipidomics of exosomes released by PC-3 prostate cancer cells”. In: *Biochimica et biophysica acta* 1831.7 (July 2013), pp. 1302–1309. ISSN: 0006-3002. DOI: 10.1016/J.BBALIP.2013.04.011. URL: https://pubmed.ncbi.nlm.nih.gov/24046871/.

[169] Ayuko Hoshino et al. “Tumour exosome integrins determine organotropic metastasis”. In: *Nature 2015 527:7578* 527.7578 (Oct. 2015), pp. 329–335. ISSN: 1476-4687. DOI: 10.1038/nature15756. URL: https://www.nature.com/articles/nature15756.

[170] Agnes T. Reiner et al. “Concise Review: Developing Best-Practice Models for the Therapeutic Use of Extracellular Vesicles”. In: *Stem Cells Translational Medicine* 6.8 (Aug. 2017), pp. 1730–1739. ISSN: 2157-6564. DOI: 10.1002/SCTM.17-0055. URL: https://academic.oup.com/stcltm/article/6/8/1730/6448755.

[171] Laura Patras et al. “Trojan horse treatment based on PEG-coated extracellular vesicles to deliver doxorubicin to melanoma in vitro and in vivo”. In: *Cancer Biology and Therapy* 23.1 (2022), pp. 1–16. ISSN: 15558576. DOI: 10.1080/15384047.2021.2003656/SUPPL{_}FILE/KCBT{_}A{_}2003656{_}SM5125.ZIP. URL: https://www.tandfonline.com/doi/abs/10.1080/15384047.2021.2003656.

[172] BCC Publishing. *Exosome Diagnostics and Therapeutics: Global Markets*. Tech. rep. 2021.

[173] Sabrina Roy et al. “Navigating the Landscape of Tumor Extracellular Vesicle Heterogeneity”. In: *International Journal of Molecular Sciences* 20.6 (Mar. 2019). ISSN: 14220067. DOI: 10.3390/IJMS20061349. URL: /pmc/articles/PMC6471355/%20/pmc/articles/PMC6471355/?report=abstract%20https://www.ncbi.nlm.nih.gov/pmc/articles/PMC6471355/.

[174] David J. Teece. “Business Models, Business Strategy and Innovation”. In: *Long Range Planning* 43.2-3 (Apr. 2010), pp. 172–194. ISSN: 0024-6301. DOI: 10.1016/J.LRP.2009.07.003.

[175] *Bio-Techne To Acquire Exosome Diagnostics, Inc. | Bio-Techne Exosome*. URL: https://www.exosomedx.com/news-events/bio-techne-acquire-exosome-diagnostics-inc.

[176] Dana Al Sulaiman et al. “High-Resolution Patterning of Hydrogel Sensing Motifs within Fibrous Substrates for Sensitive and Multiplexed Detection of Biomarkers”. In: *ACS Sensors* 6.1 (Jan. 2020), pp. 203–211. DOI: 10.1021/ACSSENSORS.0C02121. URL: https://pubs.acs.org/doi/full/10.1021/acssensors.0c02121.